Prototyping and testing analog electronics and dishes for HIRAX and CHORD

Elizabeth Pieters, Department of Physics

McGill University, Montreal

November, 2021

A thesis submitted to McGill University in partial fulfillment of the requirements of the degree of

Master of Physics

Abstract

Multiple radio telescope arrays, each consisting of hundreds of individual dishes, are slated for construction over the next few years, such as the Hydrogen Intensity and Real-time Analysis eXperiment (HIRAX) and the Canadian Hydrogen Observatory and Radio-transient Detector (CHORD). These arrays will map neutral hydrogen emission, providing insight into the expansion of the universe and the nature of dark energy. Also investigated by these arrays are fast radio bursts (FRBs), which are unexplained bursts of radio waves lasting on the order of a millisecond. Prototyping and testing with smaller arrays of dishes is required before construction of the larger arrays begin. CHORD and HIRAX use test setups at the Dominion Radio Astrophysical Observatory (DRAO) in Kaledon, BC. The Deep Dish Development Array (D3A) at DRAO consists of two three meter diameter dishes. Three six-meter diameter dishes are currently under construction as well. This thesis discusses elements of the design, construction, and characterization of different components of D3A. Characterization of the 2019 passive analog electronics chain at D3A is described, along with the construction and testing of both the 2021 HIRAX active feed and analog electronics chain currently in place at D3A, and the D3A analog electronics for the CHORD feed. A newly constructed tool known as a reflectometer used to measure composite dish uniformity is presented.

Résumé

Au cours des prochaines années, la construction de plusieurs réseaux de radiotélescopes, comme HIRAX (Hydrogen Intesity and Real-time Analysis eXperiment) et CHORD (Canadian Hydrogen Observatory and Radio-transient Detector), chacun composé de centaines d'antennes, est planifiée. Ces radiotélescopes produiront des images interférométriques de l'émission d'hydrogène neutre, qui permettront de mieux comprendre l'expansion de l'univers ainsi que la nature de l'énergie sombre. Ces radiotélescopes permettront également à l'étude des sursauts radio rapides (FRB), des sursauts inexpliqués d'ondes radio d'une durée de l'ordre d'une milliseconde. Il est nécessaire de réaliser des prototypes et des tests avec des réseaux d'antennes plus petits avant de commencer la construction des réseaux plus grands. CHORD et HIRAX utilisent des installations d'essai à l'Observatoire fédéral de radioastrophysique (OFR) à Kaledon, en Colombie-Britannique. Le D3A (Deep Dish Development Array) à l'OFR est composé de deux antennes paraboliques de trois mètres en diamètre. Trois paraboles de six mètres en diamètre sont également en construction. Cette thèse discute des éléments du design, de la construction et de la caractérisation des différentes composantes du D3A. La caractérisation de la chaîne électronique analogique passive de 2019 à D3A est décrite, ainsi que la construction et les tests de l'alimentation active et de la chaîne électronique analogique de HIRAX 2021 actuellement en place à D3A, et de l'électronique analogique de D3A pour l'alimentation de CHORD. Un nouvel outil, le réflectomètre, qui est utilisé pour mesurer l'uniformité d'une antenne parabolique est aussi présenté.

Acknowledgements

A big thank you to all the members of the CHORD and HIRAX collaborations, whose vision and expertise drives the prototyping forward, and to the staff at DRAO for the countless hours spent working on D3A. Another big thank you to my supervisors, Cynthia Chiang and Matt Dobbs, for helping me explore the incredible world of radio telescopes and supporting me throughout my degree. Further thank yous to Dallas Wulf, who has been showing me the ropes since day one, and to Kit Gerodias, for making schoolwork and fieldwork that much more fun. Thank you to all my labmates and the excellent technical lab staff at McGill for the help and camaraderie. To my family and friends, another thank you; I would not have made it here without you. And last but not least, a giant thank you and all my love to my husband John Forsyth for joining me on this adventure.

Table of Contents

List of Figures

List of Tables

Chapter 1

Introduction

1.1 Cosmology and astronomy at radio frequencies

1.1.1 Hydrogen intensity mapping

Neutral hydrogen emits radiation at a wavelength of 21 cm (1420 MHz) because of interactions between the proton and electron's magnetic moments, known as hyperfine splitting [1]. This signal can be used to map hydrogen throughout the universe, which is important because hydrogen comprises nearly 75% of the gas in the by mass. The large proportion of hydrogen present allows it to be used as a tracer for the distribution of matter in the universe. Examining the 21 cm signal at different redshifts provides hydrogen maps that trace the evolution of large scale structure of universal matter through time, and will provide constraints for cosmological models that seek to uncover the nature of dark energy.

Dark energy

One of the great mysteries of modern cosmology is understanding dark energy. The recent (on cosmological timescales) acceleration in the expansion of the universe is attributed to the presence of energy that has not been directly observed, and is therefore

referred to as 'dark'. The equation of state used to describe the behaviour of dark energy, as well as other cosmological components such as radiation and matter, is the linear equation [2, Eq. 4.55]

$$\mathrm{P} = w\varepsilon, \tag{1.1}$$

where P is the pressure, w is the unitless equation of state parameter, and ε is the energy density [2], which is often written in terms of the unitless density parameter Ω. Radiation and matter have $w = 1/3$ and $w \sim 0$ respectively. To be considered dark energy, a substance should have $w < -1/3$ because that range of values will result in positive acceleration in the expansion of the universe [2].

Pinpointing parameters such as w and Ω is critical for generating models of our universe and its evolution. Future experiments plan to constrain parameters pertaining to dark energy, including the dark energy density parameter Ω_{DE} to less than 1% [3]. One method of determining these cosmological parameters is by looking at baryon acoustic oscillations.

Baryon acoustic oscillations

At a redshift of $z \sim 1090$ [2] the universe was hot and dense, forming a plasma that trapped photons. This photon-baryon fluid was capable of supporting acoustic pressure waves generated by areas of over and underdensity within the plasma. As the universe expanded it cooled, and at the epoch of recombination the elements in the plasma recombined and no longer supported the acoustic waves. These waves were essentially 'frozen out', no longer propagating but leaving a measurable effect on both the photons and baryons. In the case of baryons, the oscillations left an imprint on the baryon matter distribution of the early universe, known as Baryon Acoustic Oscillations (BAOs). Given the length of time the universe existed as a plasma, the characteristic scale the BAOs reached before freezing out can be calculated at a comoving scale of about 160 Mpc [2]. As the universe continued to expand, so did the matter distributions left by the acoustic waves,

providing an opportunity to use BAOs as a standard ruler to measure the expansion of the universe.

Hydrogen intensity mapping at a given redshift provides information about large scale structure across the sky, effectively measuring the density distribution of the universe. The two-point correlation function of this distribution exhibits a peak at the length scale corresponding to baryon acoustic oscillations that have been measured in the Sloan Digital Sky Survey data [4] at optical frequencies and which can also be detected in radio frequencies when cross-correlated with optical data [5]. Various properties such as the angular size, location, and amplitude of the BAO peak can be used to constrain different cosmological parameters, including the equation of state parameter of dark energy and various density parameters [2]. Note that the same information can be extracted from the matter power spectrum, which is the Fourier transform of the correlation function [2].

An intensity mapping instrument built to detect BAOs would aim for increased sensitivity at the angular scales that correspond to the size of the BAOs at the cost of other attributes such as resolution; the tradeoffs made to achieve this higher sensitivity are discussed further in Section 1.2.2. Current and upcoming instruments built to perform large scale hydrogen intensity mapping include the Canadian Hydrogen Intensity Mapping Experiment (CHIME), the Hydrogen Intensity and Real-time Analysis eXperiment (HIRAX) and the Canadian Hydrogen Observatory and Radio-transient Detector (CHORD). CHIME and HIRAX radio telescope arrays cover a frequency range of 400-800 MHz in order to capture the redshifted neutral hydrogen emission from redshifts $0.8 \lesssim z \lesssim 2.5$ [3]. CHORD will cover 300-1500 MHz. CHIME, HIRAX, and CHORD all have large fields of view and increased sensitivities at relevant angular scales. Further radio telescopes include the Tianlai Project that is developing both the Tianlai Cylindrical Pathfinder Array [6] and the Tianlai Dish Pathfinder array [7], which plan to provide observations from 500–1500 MHz and 400-1430 MHz respectively. MeerKAT, which is itself a precursor to the larger upcoming Square Kilometer Array, is planning a survey known as the MeerKAT Large Area Synoptic Survey (MeerKLASS) covering 900–1670 MHz which

emphasizes survey speed over resolution [8]. All experiments plan to perform significant hydrogen intensity mapping in order to shed light on dark energy.

1.1.2 Radio transients

Radio transients are astrophysical phenomena that emit short duration or rapidly varying radio frequency signals. Some radio transients have a known cause, such as pulsars. Pulsars are rapidly rotating neutron stars with a strong magnetic field that emits radiation at radio frequencies. The emission can be detected only when the magnetic pole of the pulsar is visible, causing a 'pulsing' signal corresponding to the rotation of the neutron star [9]. Another recently discovered form of radio transients are irregular radio frequency bursts that last anywhere from tens of nanoseconds to a few milliseconds. These are known as fast radio bursts, or FRBs.

Fast radio bursts

First discovered in 2007, FRBs are a growing topic of interest in the astrophysical community as their cause has yet to be determined. Some FRBs are repeating or even periodic, with the majority thus far not observed to repeat. All FRBs originate from outside of our galaxy with the exception of a single non-repeater localized to a magnetar within the Milky Way. Whether all FRBs are magnetars, and what the physics behind repeaters are, is an area of open research [10].

A significant problem in studying FRBs was that, until recently, there were not enough detections to form a comprehensive and statistically powerful study. The primary reason is that the field of view of radio telescopes sensitive enough to detect FRBs is not large enough to observe more than a small fraction of the sky at once. However, the recent publication of the first CHIME/FRB catalogue [11] has quadrupled [10] the number of detected FRBs with a 536 documented fast radio bursts. CHIME was able to make these discoveries due to its very large 200 square degree [12] field of view. CHORD and HIRAX are positioned to discover yet more FRBs. HIRAX will be located in the southern hemi-

sphere and with 256 dishes, a quarter of the final planned number, will have a sensitivity and collecting area similar to CHIME's [13]. CHORD will have a much higher sensitivity than CHIME as well as detecting detecting FRBs on a wider frequency band, and both CHORD and CHIME have plans to operate outrigger stations to provide FRB localization [14]. The influx of FRB detections from each instrument will provide key datasets for understanding FRBs.

1.2 Principles of radio interferometry

Radio interferometry uses arrays of spaced out elements that act together as a single instrument capable of detecting very quiet signals. In a traditional single dish telescope, light is reflected from each part of the dish onto the feed. A dish made of fractured pieces would still perform much the same function, with some loss of signal between the pieces. Interferometry takes that one step further, separating the pieces of the dish into different elements and providing each one with its own feed to collect the signals. Rather than the single dish where signals are combined automatically at the feed after reflecting off of the dish, the signals from each element in the interferometer are combined later in a component known as the correlator, which performs a correlation as discussed in Section 1.2.1. These elements, although separated, are part of the single large interferometer and work together to produce the overall picture, much like observing the sky through a cracked mirror.

Radio interferometers have a number of tradeoffs when compared to single dish telescopes. The placement of the elements in the interferometer can shape what angular scales the interferometer sees, and can focus on scales of interest at the cost of others (see Section 1.2.2). Repeated dishes can be more cost effective for providing a large collecting area than a single large dish, but incur a significant computational cost, up to N^2 for correlating each pair of signals from N elements in a traditional interferometer [15]. Understanding the components of a radio interferometer and the differences between the

two types of telescope provides the groundwork for selecting the best design for a given science goal.

1.2.1 Correlation

Unlike in a single dish where incoming signals bounce off every part of the dish and are combined at the feed, the separated elements of an interferometer each receive individual signals that must be combined after they have been converted by the antenna into a voltage. The correlator combines pairs of received signals by multiplying the voltages together to form a cross-correlation. The response of the correlator $r(\tau)$ to two voltage signals $V_1(t)$ and $V_2(t)$ can be expressed (as in Ref. [16, Eq. 3.19]) by

$$r(\tau) = \lim_{T \to +\infty} \frac{1}{2T} \int_{-T}^{T} V_1(t) V_2^*(t-\tau) dt, \tag{1.2}$$

where $V_2^*(t)$ is the complex conjugate of $V_2(t)$. The variance of the noise in the correlator output is inversely proportional to the integration time, which means that longer integration times allow for more sensitive measurements. In the case of single dishes, there is no need for the correlation function, but the signal is still integrated with root mean squared (rms) fluctuations decreasing as the square root of the integration time, as described by the radiometer equation [17]. In this way radio telescopes can observe minuscule signals from distant reaches of space that would otherwise be lost in noise.

1.2.2 Baselines

The distance between two elements in an interferometric array is referred to as a baseline, and the correlator outputs from pairs of elements are called visibilities. Mathematically the sky intensities have approximately a 2D Fourier transform relationship with the visibilities produced by each pair of elements [16], and the longer baselines measure higher spatial frequency of intensities on the sky. Therefore the range of baselines within an array determines the sizes of objects that an array can pick out in the sky. If there are long

baselines, the array can resolve smaller objects, and with shorter baselines the array can determine large scale average intensities. Within a single dish telescope, the baselines can be thought of as the distance from any one piece of the dish to another. The ease of placing two small dishes a kilometre apart compared to building a kilometre wide dish illustrates the advantage of using interferometers for high resolution images. However obtaining a single high resolution baseline to take measurements at a given angular scale comes at the cost of the continuous baselines and therefore continuous angular scales available in a single dish.

The relationship between the baseline lengths and the resolution observed in the sky drives different layouts of interferometric arrays. Imaging arrays, which create detailed images of the sky, require information on all different length scales in order to properly 'see' the sky, and thus require as many different baselines as possible to capture different spatial frequencies. The need for many different baselines drives an irregular, even pseudo-random layout of the elements. Other arrays focus on particular length scales and create regular, grid-like arrays with as many identical baselines as possible in order to generate statistical information on the scales important for a particular science goal. Having identical baselines provides heightened sensitivity at certain scales but sacrifices the wide range of baselines required for images.

1.2.3 Redundancy

Arrays that use repeated baselines to generate statistical information as discussed in Section 1.2.2 often rely on the baselines being redundant, which means that the repeated baselines are providing identical signals. To achieve this, the array must be redundant: each element of the array, including spacing, dishes, feeds, and electronic components, must be identical. Practical considerations such as manufacturing tolerances and element placement limit how similar elements in the array can be, but striving for redundancy in an array reduces systematic errors in noise and heightens sensitivity. Having a redundant array provides other significant benefits such as simplified calibration methods [3]. Data

from identical baselines can be averaged before being saved, resulting in a significant reduction in data storage. Averaging the data comes with a risk however, because if the baselines are not redundant, the data will be permanently corrupted by the systematics of the array. This risk further drives the need for prototyping and testing to ensure that the final array will achieve the necessary degree of redundancy.

1.2.4 Noise Temperature

In radio astronomy it is often convenient to express noise power as a temperature by using the concept of Johnson or Nyquist noise. Here the temperature refers to the physical temperature of a resistor necessary to generate the equivalent noise power, a relationship described by

$$P_{\mathrm{N}} = k_{\mathrm{B}} T \Delta f, \tag{1.3}$$

where P_{N} is the noise power, k_{B} is Boltzmann's constant, T is the noise temperature in Kelvin and Δf is the frequency bandwidth (see Ref. [18]).

The noise temperature is additive, allowing each component of the signal to be analyzed independently and then summed to regain the total signal temperature. When including all sources of noise the total combined temperature can exceed 50 K (such as in early tests of the D3A prototype discussed in Section 1.4.4); the desired component of the signal, the sky signal, is only a fraction of this value. The excess noise temperature enters the signal both at the antenna, where spillover to the warm ground, radio frequency interference (RFI), and signals from unwanted sources are picked up, and in the receiver throughout the electronic components and cables used to transport, amplify or filter the signal.

We break down the total combined temperature T_{tot} into four main components (excluding sources such as RFI and the sun). These components, shown in Fig. 1.1, are

- T_{sky}: the temperature from the desired sky signal
- T_{A}: the noise temperature added from the antenna

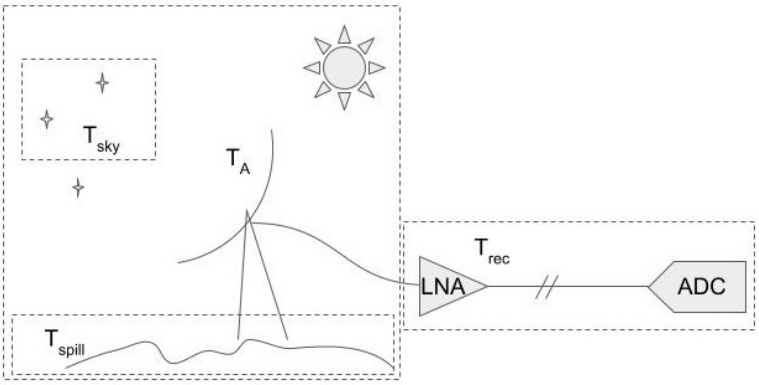

Figure 1.1: Sources of noise temperature in the radio telescope system, including temperature contributed by the sky signal $T_{\rm sky}$, the antenna, $T_{\rm A}$, spillover to the ground, $T_{\rm spill}$, and the receiver electronics $T_{\rm rec}$.

- $T_{\rm spill}$: the noise temperature added from ground spill
- $T_{\rm rec}$: the receiver noise temperature added in the electronic components,

where

$$T_{\rm tot} = T_{\rm sky} + T_A + T_{\rm spill} + T_{\rm rec}. \tag{1.4}$$

The combined noise temperature from the antenna, ground spill, and electronics can be referred to as the system temperature ($T_{\rm sys}$), and minimizing $T_{\rm sys}$ is a constant focus for improving radio telescopes.

Referred Noise Temperature

Noise temperature within the electronics chain is added to the signal by each individual component. Rather than provide detailed specifications of the noise performance of each component, it is more convenient to provide one frequency dependent value describing all the noise temperature contributions referred to a single position in the chain. This 'referred noise temperature' must also take into account the amplification, attenuation, and filtering that occurs in different stages along the chain, which alters the impact of introducing noise in a given stage. For example, if the signal is amplified by a factor of

one hundred, adding noise before the amplification is equivalent to adding one hundred times the noise afterwards.

In this thesis the noise temperature is referred to the input of the first low-noise amplifier (LNA) in the electronics chain, located after the feed. To refer the noise temperature to the input of the LNA, the noise temperature added in each component is divided by the preceding gain in the electronics chain. This process is illustrated in Fig.1.2, highlighting the importance of placing a low-noise amplifier first in the signal chain to reduce the effect of any subsequently added noise. In a well-designed system, the noise of the first stage amplifier dominates the electronics noise and should be as low as technology and cost allows. For radio telescope arrays a first stage amplifier noise of around 25 K is becoming common and affordable.

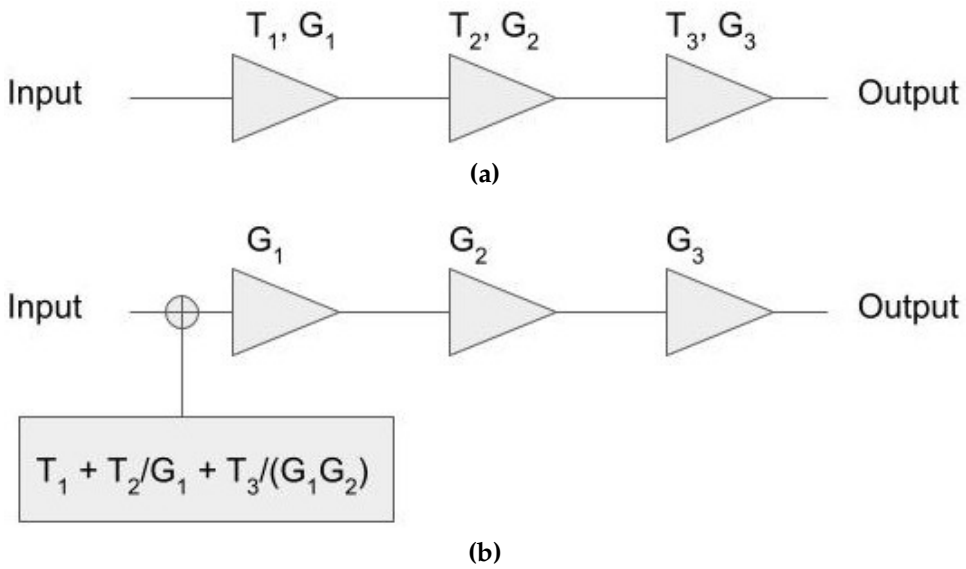

Figure 1.2: Example a) showing noise temperature added to an electronics chain in each component and b) the equivalent noise temperature referred to the input of the chain. T_i is the input referred noise and G_i is the gain of each component.

Noise Figure

For non-astronomy applications, it is more common to measure the noise figure in decibels (dB) instead of the noise temperature. As such, the noise performance of electronics

components is often listed on the datasheet as the noise figure [19], which can then be translated to a noise temperature. The noise figure represents the effective input (or output) noise temperature compared to a reference temperature of 290 K. The noise figure (NF) can be converted to noise temperature (T) using

$$T(K) = T_{\mathrm{REF}}(K)\left(10^{\frac{NF(dB)}{10}} - 1\right) \tag{1.5}$$

where the T_{REF} is the reference temperature of 290 K. [19, 20].

Noise from Attenuators

The effective input-referred noise temperature T_{e} generated in an attenuator is expressed as

$$T_{\mathrm{e}} = (L-1)T, \tag{1.6}$$

where L is the (linear) loss factor and equal to the inverse of the gain, and T is the physical temperature of the system [21, Eq. 10.15]. This equation holds for loss in transmission lines and coaxial cable [21–23]. During our later analysis of the electronics chains this equation is used to calculate the contribution of coax cables to the noise temperature.

1.3 Radio telescope components

1.3.1 Antennas

Feeds

The feed is the component of the antenna that translates incoming electromagnetic radiation into an analog voltage signal. Different feeds will pick up different polarizations of light, whether circular or linear polarizations. The feeds used in radio astronomy arrays are often designed to pick up two linear polarizations that are offset by 90 degrees, referred to as x and y polarization. Each feed will therefore generate two signals describing

the x and y polarization of the incident light. The electromagnetic performance of a feed is often verified using simulation software, such as CST [24].

Dishes

The dish is the component of the antenna that focuses incoming radiation onto the feed, which increases the amount of signal incident upon the feed while simultaneously reducing the field of view to a smaller region of the sky. The reflective dish should be large relative to a wavelength [18], which in the radio can be close to a metre (400 MHz corresponds to a 75 cm wavelength). Individual dishes should therefore have a minimum size of a couple metres in diameter. Having longer wavelengths ($\sim$10's of cm) additionally means that the observed photons are less sensitive to cm or mm deviations of the reflective surface. This insensitivity often leads to more relaxed requirements for the precision of the reflective surface than at higher frequencies; this is not the case in HIRAX and CHORD, where redundancy between dishes is important for calibration and data analysis. These arrays have requirements on the reflective surfaces of the dishes that are far more stringent than those typically used in radio astronomy, driving the need for new dish manufacturing techniques as discussed in Section 1.4.4.

The overall collecting area of the array is another important consideration. As discussed in Section 1.2, the larger the overall collecting area of the array, the less observing time is required to produce data products with an acceptable amount of noise. These two considerations, the minimum size of dishes and the overall collecting size of the array, can result in different designs, such as the large structures seen in CHIME (Fig. 1.3), or the smaller but more numerous dishes planned for HIRAX (Fig. 1.4) and CHORD.

1.3.2 Electronics

Analog electronics

The analog electronics modify the signal produced by the feed into a form that can be readily converted into a digital signal. When the signal is transported from the individual elements to a central digitizing and processing location in analog form, for instance over a coaxial cable, the electronics are typically split into a front-end and back-end stage. The front-end electronics consist of extremely low noise amplification which happens in components mounted on or immediately after the feed, before the coaxial cable. As discussed in Section 1.2.4 the noise from this first amplification step will be the dominant noise component from the noise added in throughout the analog electronics chain, so it is important that the noise added here is as minimal as possible. The back-end stage of the electronics typically occurs in a shielded screen room located away from the dish and connected to the front-end stage by coaxial cable. The back-end stage of the analog chain then filters the signal to the desired frequency range and provides any further amplification necessary before the input to the data acquisition system where the analog-to-digital conversion occurs.

Data acquisition system

The data acquisition system performs a number of different operations, including converting the incoming analog voltage into a digital signal and performing the correlation discussed in Section 1.2.1. The system requires a number of different components, a large amount of computing power, and its discussion is outside the scope of this thesis. For further information on CHIME's data acquisition and processing, see Refs. [25, 26].

Figure 1.3: CHIME telescope located at DRAO near Penticton, BC. The telescope consists of four 20x100 m segments that each have 256 feeds. Photo from CHIME website [12].

1.4 Radio interferometric arrays

1.4.1 Canadian Hydrogen Intensity Mapping Experiment

CHIME is located near Penticton, BC at the Dominion Radio Astrophysical Observatory as seen in Fig. 1.3. A drift-scan telescope, CHIME scans the sky as it passes directly overhead and cannot be tilted to change its observation angle. CHIME has four 20x100 m fixed reflective segments placed side by side that each have 256 feeds spaced lengthwise that detect 400-800 MHz frequencies. The resulting field of view is larger than 200 square degrees [27]. This massive field of view has been instrumental in detecting fast radio bursts, with a recently published catalogue of 536 fast radio bursts (see Ref. [11]). Outriggers, which are smaller versions of the main telescope but located thousands of kilometers away, are planned to provide very long baselines and therefore higher localization of detected FRBs on the sky [28], as CHIME continues to monitor for FRBs and other radio transients along with performing hydrogen mapping of redshifts $0.8 \lesssim z \lesssim 2.5$.

1.4.2 Hydrogen Intensity Real-time Analysis eXperiment

HIRAX will be located in the Karoo desert in South Africa, mapping areas of the sky in the southern hemisphere unavailable to CHIME and CHORD. The frequency range will be identical to CHIME at 400-800 MHz. Rather than the few large structures seen in the CHIME design, HIRAX will be composed of 1024 (256 currently funded) identical six meter parabolic dishes each with a single dual-polarization feed as imagined in Fig. 1.4, providing a field of view between 15 and 56 square degrees [3]. Like CHIME, HIRAX is a drift-scan telescope; rather than moving to observe different areas of the sky HIRAX waits for the sky to move through its field of view due to the rotation of the earth. Unlike CHIME, HIRAX is not completely fixed but the dishes will be able to tilt -30 to +30 degrees in the north-south direction, though this is a manual and labour-intensive process to shift all 1024 dishes.

One of the motivating factors in switching to repeated dishes is to improve redundancy in the measurements, so to have each feed observing the sky in an identical manner. Within a cylinder, feeds towards the ends of the cylinder will have a significantly different environment than those in the center, whereas with dishes each feed has its own dish that ideally provides an identical environment to every other feed. Having this redundancy improves the sensitivity of the measurement and reduces the high demands on data storage and analysis [3]. Achieving a high level of redundancy imposes strict requirements on the variation of the reflective surface of the dishes, which must be uniform on the order of 1 mm [13].

1.4.3 Canadian Hydrogen Observatory and Radio-transient Detector

CHORD will be located next to CHIME at DRAO near Penticton, BC, and will be composed of 512 six meter parabolic dishes in a drift-scan array, which like HIRAX can be manually tilted north-south. To complement the core array and provide very long baselines, outriggers will be constructed. CHORD's bandwidth extends beyond those of

Figure 1.4: Rendering of future HIRAX array to be installed at the South Africa Radio Astronomy Observatory site in the Karoo. The array will consist of 1024 six meter parabolic dishes each with a single dual-polarization feed. Image credit Prof. C. Chiang.

CHIME and HIRAX and will include 300-1500 MHz. Similar to HIRAX, one of the main requirements of CHORD is that the measurements are redundant; each of the 512 dishes should be as identical as possible. The acceptable variance in the reflective surface of the dish is even stricter than HIRAX at 0.5 mm. This requirement has spurred new methods of fabricating dishes for radio astronomy, and several prototype dishes have been built at DRAO. Together the prototype dishes are referred to as the Deep Dish Development Array (D3A).

1.4.4 Deep Dish Development Array (D3A)

D3A acts as a prototype and test bed for HIRAX and CHORD technologies, including feeds, electronics, and the method of dish fabrication. As D3A is located at DRAO, it can provide further insight into the radio frequency environment that CHORD will encounter. D3A currently consists of two three meter dishes with three six meter dishes under construction. The layout of the existing three meter dishes and block house where

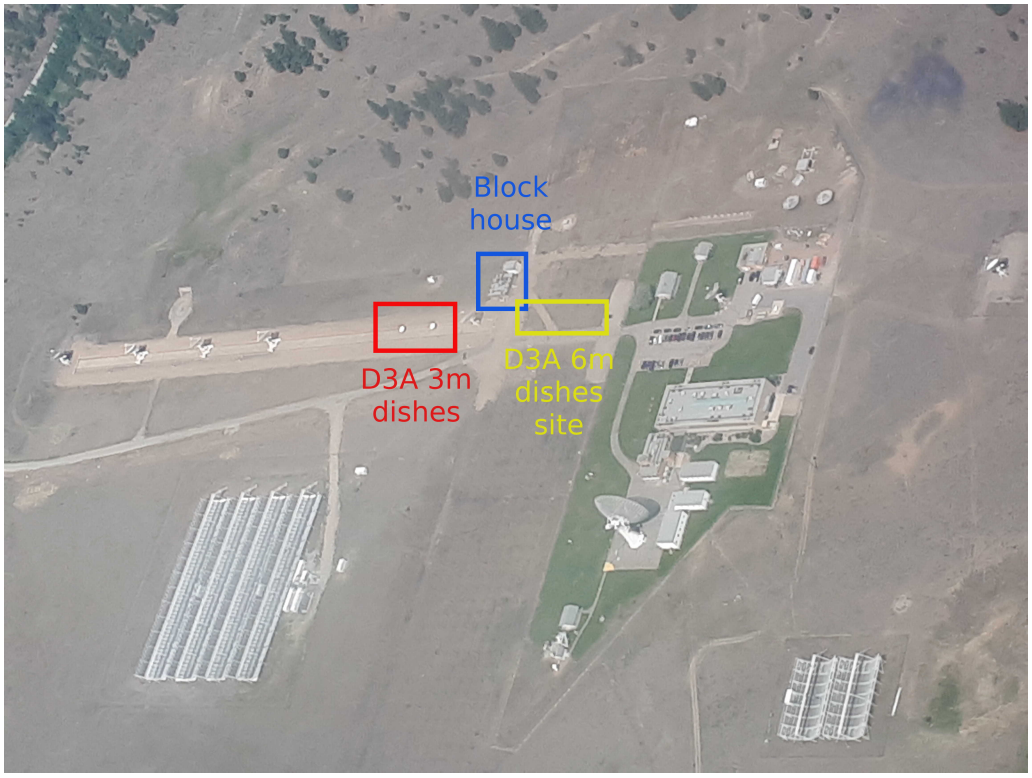

Figure 1.5: Aerial view of DRAO with the D3A three meter dishes (red), blockhouse (blue), and future site of the D3A 6 m dishes (yellow) outlined. Photo credit: D. Wulf.

the analog electronics are operated are shown in Fig. 1.5, with a single three meter dish displayed in Fig. 1.6.

Dish construction

D3A is a test bed for parabolic dish construction that will allow for the sub-mm precision required by CHORD. The process involves molding a composite material to the desired shape that has a metal mesh embedded within it. The composite material is invisible at radio wavelengths and the metal mesh acts as the reflective surface of the dish. Only a single layer of composite material lies between the inner surface of the dish and the metal mesh, so the mesh should in theory accurately follow the precise surface of the dish, which is measured with a laser tracker to ensure conformity. The mold and resulting

Figure 1.6: D3A three meter dish. Photo credit: K. Gerodias.

(a) **(b)**

Figure 1.7: D3A six meter a) mold and b) first dish sitting on mount inside workshop. Photo credit for a) K. Gerodias.

dish are shown in Fig. 1.7. The mesh lying just under the surface of the dish is shown in Fig. 1.8, which shows a section of the dish with a large number of seams.

1.5 Summary

This thesis discusses different aspects of the prototyping work underway at D3A. The first aspect, discussed in Chapter 2, is the prototype analog electronics chains, which

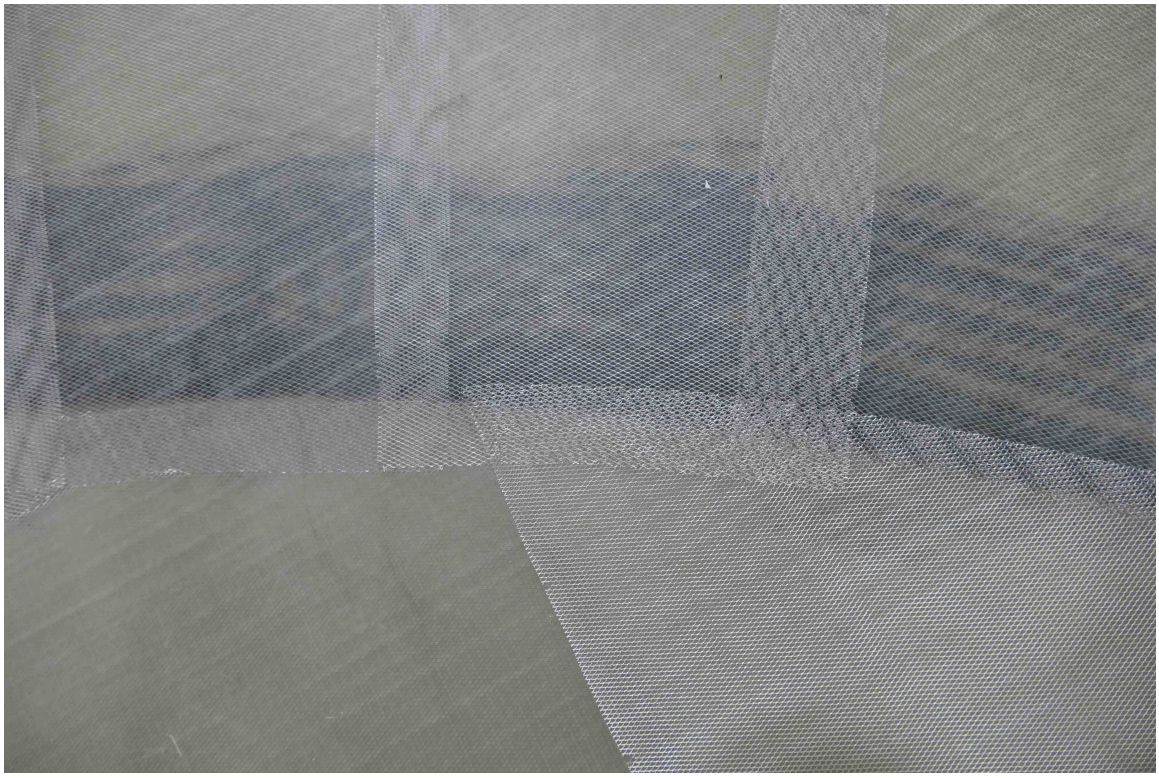

Figure 1.8: Mesh embedded inside surface of first D3A six meter dish.

includes work done by the author in characterizing the pre-existing analog electronics chain at D3A used with the passive 'CHIME-like' feed. Likewise, construction and testing of the electronics chain (designed by D. Wulf) for the ultra-wideband feed is described. The second aspect of prototyping focuses on determining the uniformity of the new D3A six meter dishes by constructing and characterizing a tool called the reflectometer. The McGill reflectometer discussed in Chapter 3 is initially constructed with the help of S. Tartakovsky and E. Eagan, and with the guidance of I. Theron who developed a similar tool for use with the KAT-7 array. Characterization of the reflectometer represents solely the author's effort, and some data sets in the six meter dish were taken with the assistance of K. Gerodias.

Chapter 2

Analog electronics at D3A

2.1 Noise temperature analysis on D3A passive feed setup

The noise temperature of a receiver system is a critical factor in the telescope's ability to make sensitive observations within a given amount of observing time. As discussed in Section 1.2.4, the noise temperature is commonly used in astronomy to describe the level of noise added in with the signal. In this section we will discuss the portion of this noise introduced within the receiver system at D3A, for example in the coaxial cable transporting the signal from the dish to where it is analyzed in the screen room located in the block house, or in electronics components such as amplifiers.

This analysis is performed using D3A data from October 2019 through January 2020 when passive clover leaf 'CHIME-like' feeds were installed and tested in the two three meter dishes, with the analog electronics chain displayed in Fig 2.1. Throughout October 19 2019 to November 5 2019 the west dish had the feed removed and replaced with a 50 Ω terminator at the input of the LNA (the P33ULN in Fig. 2.1), effectively replacing the $\sim$5-10 K frequency variable sky signal from the feed with a spectrally flat 300 K signal attributable to Johnson noise in the resistor. The two datasets with the feed and with the terminator are referred to as 'sky data' and 'terminated data' respectively.

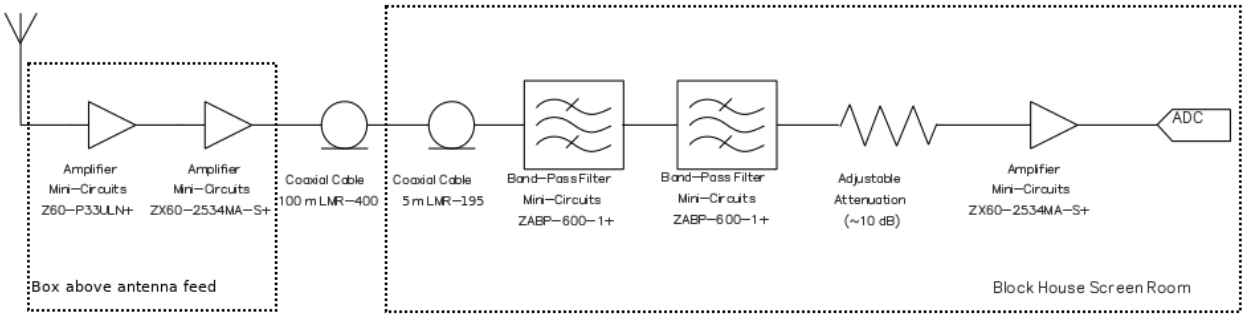

Figure 2.1: D3A passive feed electronics setup 2019, updated from original from D. Wulf, private communication, July 2020.

The terminated data have a known input that can be exploited to help characterize the subsequent electronics chain. This characterization was particularly important when access to the D3A setup was limited and removing and testing the chains was not an option. To compare the terminated signal to the expected performance of the electronics chain, datasheet values for gain and noise figure are compiled for each component, then combined to simulate the whole chain. The results of this analysis are discussed in Section 2.1.1, and the comparison to the results of the terminated data analysis are shown in Section 2.1.2.

2.1.1 Datasheet performance

The datasheet information for the gain and noise figure (when available) of each component in the D3A electronics setup (Fig. 2.1) is compiled and used to calculate the theoretical gain of the chain, shown in Fig. 2.2. The typical performance values from the datasheets are used and are unlikely to differ from the component's actual gain by more than 1 dB. To determine which components are affecting the shape of the overall gain, the gain of each component is normalized to unity at 600 MHz to highlight its shape, as shown in Fig. 2.3.

Likewise, the total noise temperature referred to the input of the electronics chain (just after the feed) is calculated by converting the noise figure of each component (when available) to a noise temperature, and propagating it backwards through the gain of previous

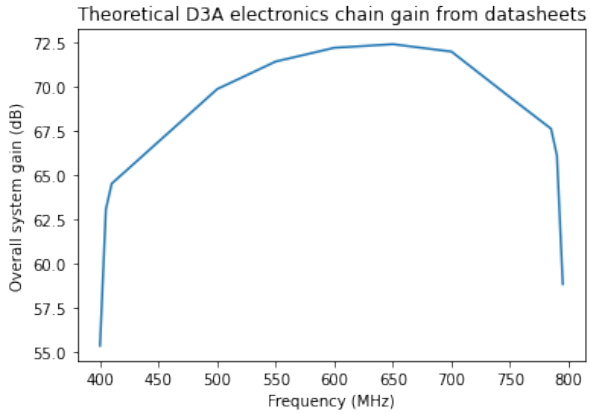

Figure 2.2: Total theoretical gain for D3A passive feed electronics chain from datasheets.

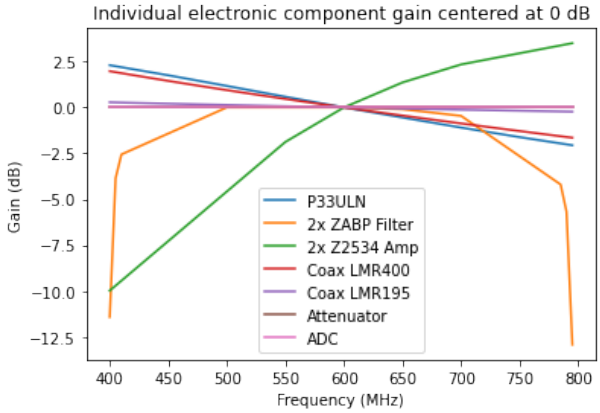

Figure 2.3: Gain shape of components in D3A passive feed electronics chain from datasheets, normalized to unity gain at 600 MHz, to display the effect of each component on the overall gain shape.

components to reach the input. The ZABP-600 bandpass filter datasheet did not have a noise figure and the two units included were assumed to contribute a negligible amount of noise, a fair approximation as the amplification from the two amplifiers preceeding the filters means that any added noise will be very small compared to the signal. Noise from attenuators and coax cables is accounted for as discussed in Section 1.2.4. The overall noise temperature of the electronics chain referred to the input is shown in Fig. 2.4, overplotted with the noise temperature of the first LNA, the Minicircuits ZX60-P33ULN+. Figure 2.4 demonstrates that the overall noise is dominated by the noise of the first am-

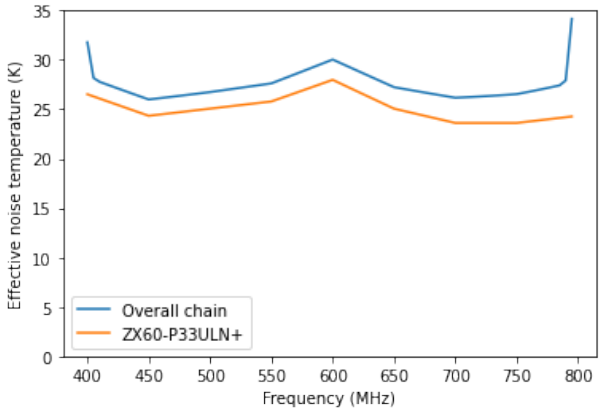

Figure 2.4: Noise temperature of the overall D3A passive electronics chain referred to the input (blue) compared to noise temperature of the ZX60-P33ULN (orange). The bandpass filters cause the referred noise temperature to rise sharply at the edges of the band. The increased separation between the overall chain and the ZX60-P33ULN at higher frequencies stems from the noise temperature of the second LNA (located before the bandpass filter) being referred to the input through the sharp negative gain slope of the ZX60-P33ULN. The noise temperature of the ZX60-P33ULN, which is the first LNA in the electronics chain, dominates the overall noise temperature.

plifier, since the signal is boosted in the amplifier and subsequent noise is proportionally smaller.

Impedance Mismatch

The previous datasheet analysis for the gain and noise temperature assumes that the impedance of the components is matched. Serious mismatch can create a frequency-dependent change in either the gain or the noise temperature. Given that the Minicircuits components and coaxial cables comprising the chain all have a nominal impedance of 50 Ω, the largest source of impedance mismatch is likely between the antenna and the input to the electronics chain.

The gain at impedances other than the nominal 50 Ω for the ZX60-P33ULN+ is unavailable on the datasheets, so an estimate is made using the formula for the 2-port trans-

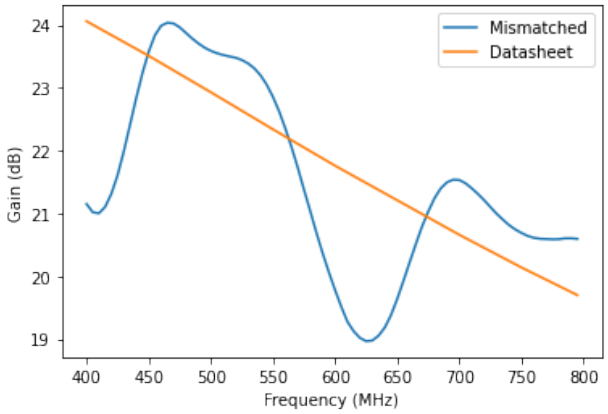

Figure 2.5: Gain for ZX60-P33ULN+ from datasheet (orange) and with mismatch estimate to feed (blue). The mismatch between the amplifier and feed causes changes in the gain of the amplifier.

ducer power gain (G_t) [29], which relies on the reflection coefficients Γ_S and Γ_L and the S-parameters (see Appendix A for a discussion of S-parameters), and is calculated by

$$G_\mathrm{t} = \frac{(1-|\Gamma_\mathrm{S}|^2)|S_{21}|^2(1-|\Gamma_\mathrm{L}|^2)}{|(1-S_{11}\Gamma_\mathrm{S})(1-S_{22}\Gamma_\mathrm{L})-S_{12}S_{21}\Gamma_\mathrm{S}\Gamma_\mathrm{L}|^2}. \tag{2.1}$$

Γ_S and Γ_L are calculated using the source and load impedances (Z_S and Z_L respectively), where each reflection coefficient is calculated using

$$\Gamma_\mathrm{X} = \frac{Z_\mathrm{X}-Z_0}{Z_\mathrm{X}+Z_0}. \tag{2.2}$$

Using this formula with S-parameters from the datasheet and CST simulated input impedances for the feed and dish provided by the feed designer, V. MacKay (personal communication), the theoretical gain of the ZX60-P33ULN+ is calculated and is shown in Fig. 2.5. Note that this result should be treated as a rough estimate because of both the method and the uncertainties in the inputs.

The calculation for the noise temperature given a mismatched impedance relies upon a noise parameter dataset with only seven data points which extended between 800 MHz and 3 GHz, and therefore is extrapolated to the desired range of 400 - 800 MHz. The

extrapolation is done using a few different methods, including a constant extrapolation using the lowest frequency data point, the extrapolation provided by Scipy Interpolate's `interp1d` function [30] (which is used to interpolate other datasheet information), and a second degree polynomial fit using Numpy's `polyfit` function [31]. The formula for calculating the impedance-dependent noise factor as described in Ref. [32] is

$$F = F_{\mathrm{min}} + 4R_{\mathrm{n}}/Z_0 * \frac{(|\Gamma_{\mathrm{s}} - \Gamma_{\mathrm{opt}}|^2)}{((1 - |\Gamma_{\mathrm{s}}|^2) * |1 + \Gamma_{\mathrm{opt}}|^2)}, \tag{2.3}$$

where F_{min} is the minimum noise factor, Γ_{opt} is the optimum reflection coefficient, R_{n} is the equivalent noise resistance, Z_0 is the characteristic impedance (here 50 Ω), and Γ_{s} is the source reflection coefficient, where the feed and dish S_{11} parameter is used.

Because of the extrapolation of the noise parameters and uncertainties in simulated feed and dish S_{11} parameter, this calculation should be treated with caution. The result is shown in Fig. 2.6, displaying an increase in noise temperature in the center and lower edge of the band for the passive feed prototype, consistent through all noise parameter data extrapolation methods. Note that this estimate of the noise temperature is specific to this prototype and not indicative of the expected performance of the CHORD or HIRAX arrays, which have different feeds and electronics designed in tandem to optimize the noise performance, a process that takes into account impedance matching.

2.1.2 Terminated data performance

To compare the datasheet electronics chain specifications to the performance in the field, it is necessary to decouple the performance of the antenna and dish. This decoupling is accomplished by using D3A data from November 2, 2019, when the west dish feed was replaced by a 50 Ω terminator, providing a stable signal of about 300K across the entire band. The theoretical gain and noise temperature is compiled from the manufacturers datasheets (discussed in Section 2.1.1) and a 300 K signal is added to the beginning of the theoretical chain to provide a direct comparison to this dataset.

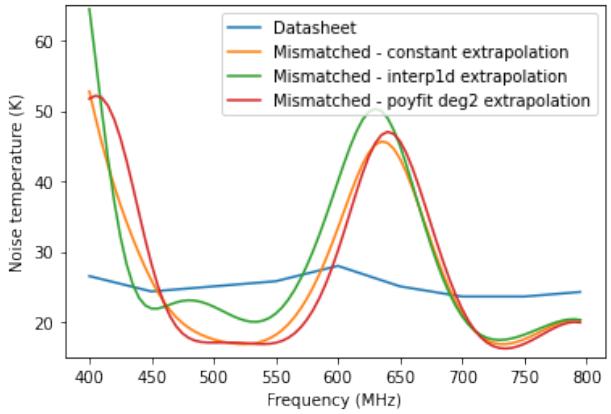

Figure 2.6: Noise temperature for ZX60-P33ULN+ from datasheet (blue) with estimate for mismatch to feed using three different extrapolation methods for the noise parameter data: a constant extrapolation using the lowest frequency data point (blue), the linear extrapolation performed by Scipy Interpolate's `interp1d` function (green), and a second degree polynomial fit using Numpy's `polyfit` function (red). By estimating the effect of impedance mismatch on the noise and gain we expect a strong noise enhancement in the center and lower edge of the band.

Gain shape comparison

Figure 2.7 displays the normalized autocorrelation of the terminated data compared to the theoretical gain. The normalization is done by dividing the data by its maximum value, which effectively removes the average gain to provide a comparison strictly of the gain shape. The gain shape appears to be consistent between the measured terminated data and the typical performance of the electronic components given on the datasheets.

Magnitude comparison

After confirming that the gain shape is in good agreement with the theoretical expectation derived from the datasheets, the next step is to determine whether the magnitude of the two signals are comparable. The raw acquisition data that measure the voltage level of the signal at the input of the analog-digital converter (ADC) are used to provide power, which can be compared to the theoretical power expected based on the 300 K input signal

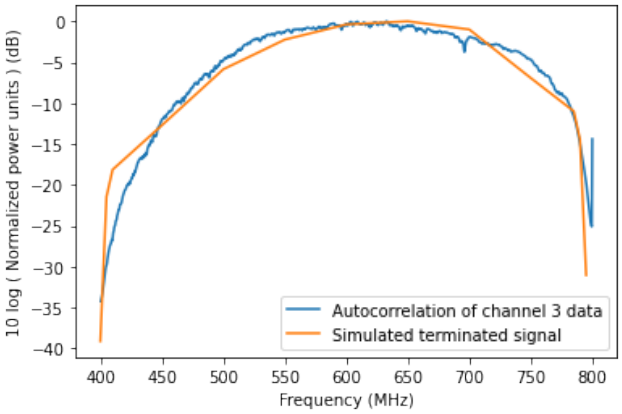

Figure 2.7: Comparison of shapes between the autocorrelation of D3A data using a 50 Ω terminator as input (blue) and a 300K signal with the theoretical datasheet gain applied (orange). D3A dataset is 20191102T000018Z_D3A west dish x polarization (channel 3) data. The gain shape of the measured data agrees with the theoretical expectation.

and theoretical gain. The raw acquisition data are in least significant bits (LSB), where $LSB = 0.5V/2^8$. Since the input resistance of the ADC of 100 Ω, this voltage can be converted to power using $P = V_{\mathrm{RMS}}^2/100\Omega$.

The theoretical power expected from the datasheets is compared to the measured power from the raw acquisition data, and is found to be 2.4 times greater than the x polarization power and only 0.43 times the y polarization power. The large difference between the x polarization and y polarization power is noted for this setup; the y polarization contains more unwanted noise seen not only in terminated measurements but also on sky measurements of Cassiopeia A transits performed both by myself and D. Wulf, resulting in a larger power. The x polarization power level represents the power level in the desired system as the on sky measurements do not show the additional noise, and has 3 dB less power than expected from the datasheets. To diagnose this discrepancy, gain measurements were conducted on individual amplifiers when the electronics chain was eventually dismantled. The amplifiers performed as indicated by their datasheets and the cause or causes of the discrepancies remain unknown.

Delay spectrum

The delay spectrum is examined to detect possible reflections throughout the receiver system that would create a delayed copy of the signal. Specifically the autocorrelation of the west dish x polarization (channel 3) is Fourier transformed; the results displayed here did not have a window applied to the data prior to the transform but including the application of a Hamming window provides very similar (albeit slightly less noisy) results. The frequency domain information is thus transformed into the delay spectrum, and a search is performed for peaks that indicate a reflected and therefore time delayed signal. One location in the signal chain where large time delays might occur is in the two coax cables running from the dish to the screen room; the 100 m LMR-400 coax cable runs from the dish to the screen room and the 5 m LMR-195 is connected to the ADC in the screen room. The calculations for the two time delays are shown below.

LMR-400 Coax Cable: 100 m of LMR-400 coax cable runs between the dish and the screen room, and the velocity of propagation quoted on the datasheet (Ref. [33]) is 0.84 times the speed of light. Therefore a signal reflecting from the connector and travelling through the cable two additional times has a time delay of

$$\tau_{400} = \frac{200\mathrm{m}}{0.84 * 3 * 10^8 \mathrm{m/s}} = 0.794\mu\mathrm{s}. \tag{2.4}$$

LMR-195 Coax Cable: 5 m of LMR-195 coax cable runs inside the screen room, and the signal inside the cable travels at 0.76 the speed of light [34]. A signal reflecting from the connector and travelling through the cable two additional times has a time delay of

$$\tau_{195} = \frac{10\mathrm{m}}{0.76 * 3 * 10^8 \mathrm{m/s}} = 0.0439\mu\mathrm{s}. \tag{2.5}$$

If light is bounced back through both cables, the resulting total time delay is

$$\tau_{\mathrm{tot}} = 0.794 + 0.0439 = 0.838\mu s. \tag{2.6}$$

Fig. 2.8 shows the delay spectrum plots are the absolute value of the Fourier transform of the autocorrelation of the x polarization with the magnitude normalized to the peak value. Also displayed are the expected time delays corresponding to a signal bouncing an extra time back and forth through the coax cables. Two peaks rise distinctly from the delay spectrum in Fig. 2.8 quite close to the 100 m cable time delay and the 100+5 m cable time delay, both at about 1/1000 of the overall signal strength. The 5 m cable time delay lies much closer to zero in the delay spectrum, where the spectrum is very noisy, and any peak caused by this time delay is indistinguishable from the noise. Because of the proximity of the two visible peaks to the theoretical time delays and their prominence in the delay spectrum, it is quite probable that they are caused by reflections at the connections between the 100 m and 5 m coax. The appearance of these reflections is not a serious concern as 1/1000 of the signal is comparable to the approximately -55 dB crosstalk between inputs on the same ADC chip [35] and is therefore an acceptably small magnitude.

The difference between the theoretical and measured time delays is likely due to inaccuracy on the datasheet value of the speed of propagation in the cables. Different copies of the datasheet for the LMR-195 have a 4% disagreement for the velocity of propagation, quoting it at 0.76 and 0.80 of the speed of light (see Refs. [34] and [36] respectively). In light of this disagreement the 3% difference between the peaks and theoretical time delays in Fig. 2.8b) quite plausible. It may be worth noting for the sake of the previous section that the attenuation information used in that section is identical between the two LMR-195 datasheets. As the delay spectrum is noticeably noisier around the peak at zero, which denotes the unreflected signal that arrives without any delay, it is hard to pick out any major reflections from that region of the spectrum.

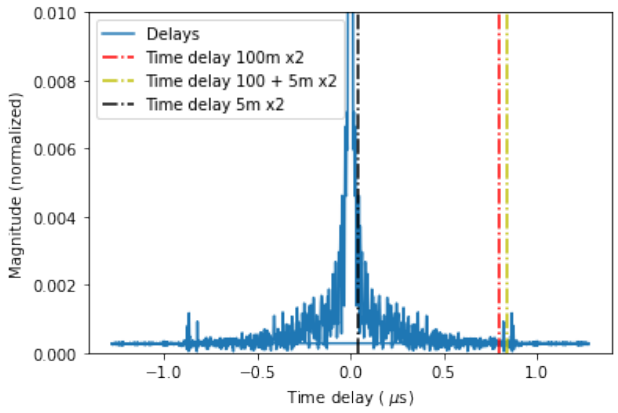

(a)

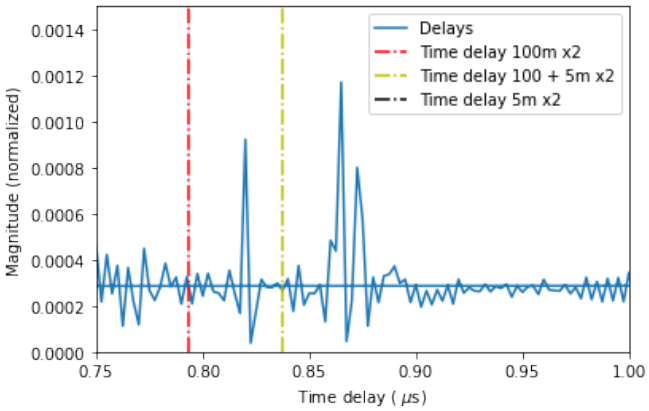

(b)

Figure 2.8: Delay spectrum of D3A west dish x polarization (channel 3) autocorrelation from 20191102T000018Z data set (blue) with a) a wider view of the delay spectrum and b) a close up of the relevant section. Plotted are the the time delay of the 100 m LMR-400 coax (red vertical line), the time delay of both the 100 m LMR-400 and 5 m LMR-195 coax (yellow vertical line), and the time delay of the 5 m LMR-195 coax (black vertical line). The appearance of two distinct peaks close to the calculated time delay for reflections in the 100 m LMR-400 and combined 100 m LMR-400 and 5 m LMR-195 are highly suggestive of reflections occurring at the cable connectors on the order of 1/1000 of the overall signal strength, small enough to be acceptable.

2.2 Ultra-wideband feed prototype analog electronics

2.2.1 Design

The CHORD frequency bandwidth of 300-1500 MHz is significantly wider than HIRAX or CHIME, necessitating the design of an ultra-wideband (UWB) feed and changes to the electronics. The three 6 m dishes require six electronics chains as each dish has both x and y polarization. To facilitate rapid testing of the UWB feed a prototype analog electronics chain is constructed to be compatible with the current data acquisition system that can handle a 400 MHz bandwidth. The 1200 MHz bandwidth is therefore split into three 400 MHz bands in the screen-room electronics that are each input into the data acquisition system. Because of the limited choices when working with off-the-shelf electronic components for prototyping, the three bands do not extend down to 300 MHz, and instead are 400-800, 800-1200, and 1200-1600 MHz. Two different versions of the analog electronics (referred to as V1 and V2) designed by D. Wulf are constructed. Three of the electronics chains (boards 1-3) are V1 and the other three (boards 4-6) are V2. The electronics schematics are shown in Fig. 2.9. The difference between V1 and V2 lies in the filters used for the two upper frequency bands, and will be discussed further in the Section 2.2.3.

2.2.2 Construction

The chains are soldered together and then mounted onto plastic boards, which slot into the rack shelf pictured in Fig. 2.10. The rack shelf has a power distribution system that requires two different voltages and a ground to be hooked into the terminal blocks shown in Fig. 2.11a). The power runs from the terminal block to 6 snap molex connectors shown in Fig. 2.11b), which clips into the corresponding connector on the electronics boards. Each board has an on-off switch to control power on the board. The rack shelf fits into a rack in the screen room at DRAO shown in Fig. 2.12 and is powered by the voltage supply on the desk.

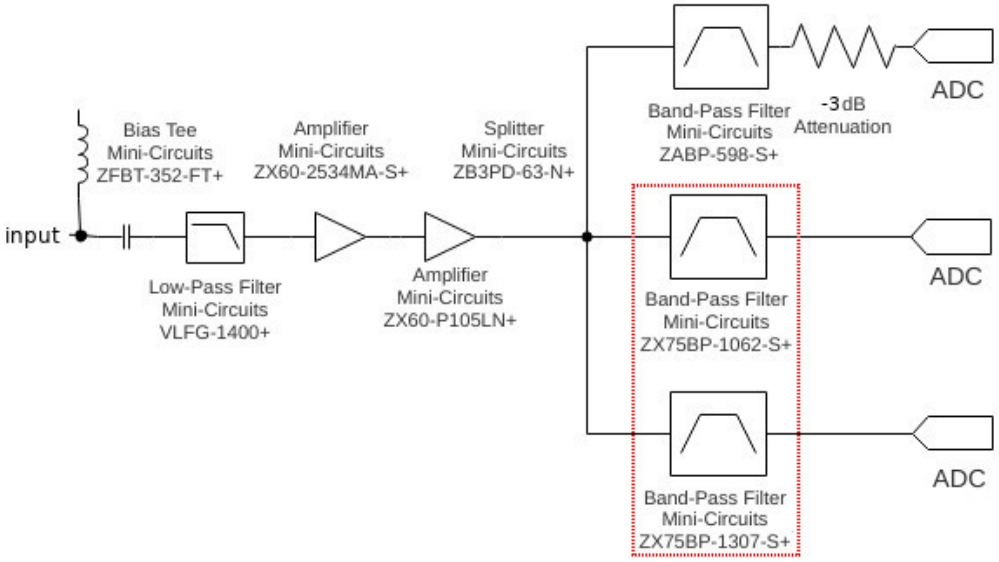

(a) V1

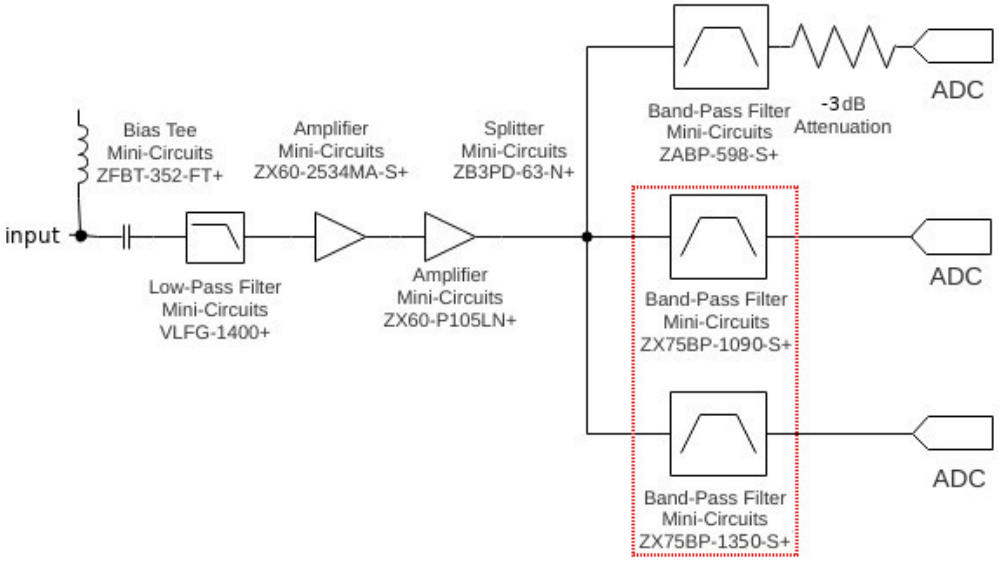

(b) V2

Figure 2.9: UWB feed analog electronics schematic a) V1 with wider bandpass filters (ZX75BP-1062-S+ and ZX75BP-1307-S+) outlined in red and b) V2 with narrower bandpass filters (ZX75BP-1090-S+ and ZX75BP-1350-S+) outlined in red.

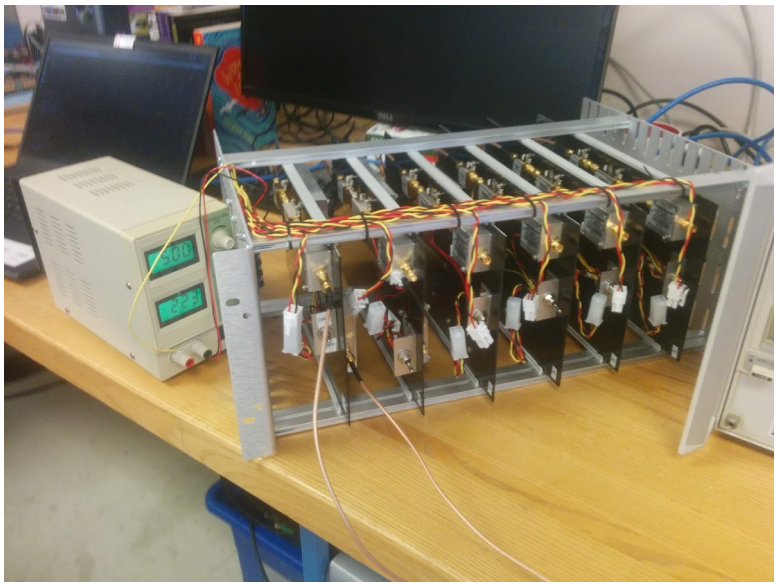

Figure 2.10: Rack shelf with the six analog electronics boards for testing the UWB feed on the three D3A 6 m dishes, powered by the voltage supply to the left.

(a) **(b)**

Figure 2.11: Power distribution for the UWB analog electronics, showing a) molex terminal blocks on rack shelf that distributes the incoming power to each board and b) UWB power connectors linking each board to the power distribution on the rack shelf.

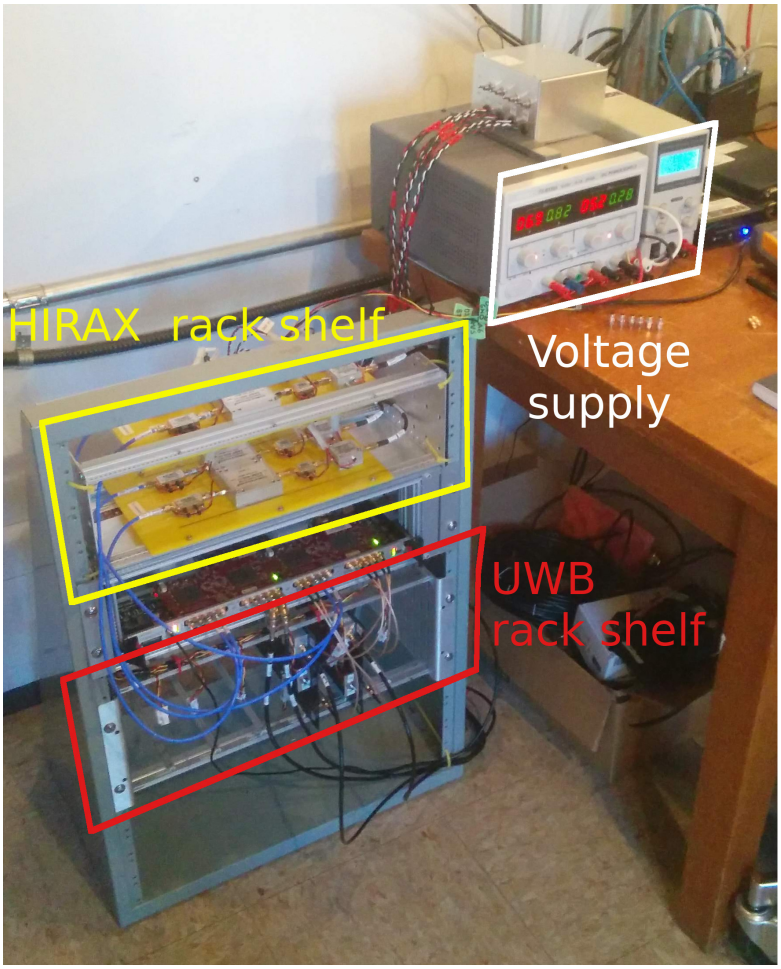

Figure 2.12: Rack in blockhouse at DRAO with shelves for the UWB feed and HIRAX feed screen room analog electronics. Only two of the six electronics boards are present on the UWB rack shelf. The voltage supply that powers the electronics chains is shown on the desk.

2.2.3 Testing

The gain is measured in the McGill Cosmology Laboratory using the Hewlett-Packard 87534E VNA and saved with a python script using code functionality from the McGill Cosmology LabPy repository maintained by J.F. Cliche. Both the theoretical gain from the datasheets and the measured gain for each board is plotted in Fig. 2.13. The displayed measurements are performed with a -50 dBm power input; further tests using -40 dBm and -60 dBm inputs confirmed the components are operating in a linear regime at these in-

put levels. In Fig. 2.13a) we see that the first version of the electronics chain (V1) amplifies the full bandwidth of each band but has significant overlap between 800-1200 and 1200-1600 MHz bands that needs to be separated in post-processing. The second version (V2) shown in Fig. 2.13b) has no overlap between the bands but lacks the full frequency range that provides information on what CHORD will detect, including possible RFI bands.

2.3 D3A analog electronics summary

The analog electronics chains in place at D3A are made of discrete components and assembled to provide a relatively fast and reliable solution to the prototyping needs. The main function of the analog electronics is to enable the testing of other more permanent components such as the feed and the dish. As we saw in Section 2.1 the electronics chain can be difficult to characterize remotely after installation at DRAO. Because we were unable to troubleshoot individual components in person, we relied on a simpler test configuration in which the electronics were disconnected from the feed and could thus be tested in isolation. We determined that the gain shape of the electronics aligned well with the expected values, and the magnitude was 3 dB lower than expected. The delay spectrum was investigated to find reflections in the system, and reflections in the cables were discovered but considered negligible.

In Section 2.2.3 we discussed the construction and testing of a new analog electronics chain created to work with the ultra-wideband feed. Two versions of this chain were created to help inform the future direction of the analog electronics for CHORD. Further, the UWB electronics chain was tested thoroughly and compared to the data sheet performance to confirm that it was behaving as expected prior to installation at D3A. This confirmation allows us to move forward with testing and characterizing the prototype ultra-wideband feed and six meter dish on the sky, a crucial step for the future performance of CHORD.

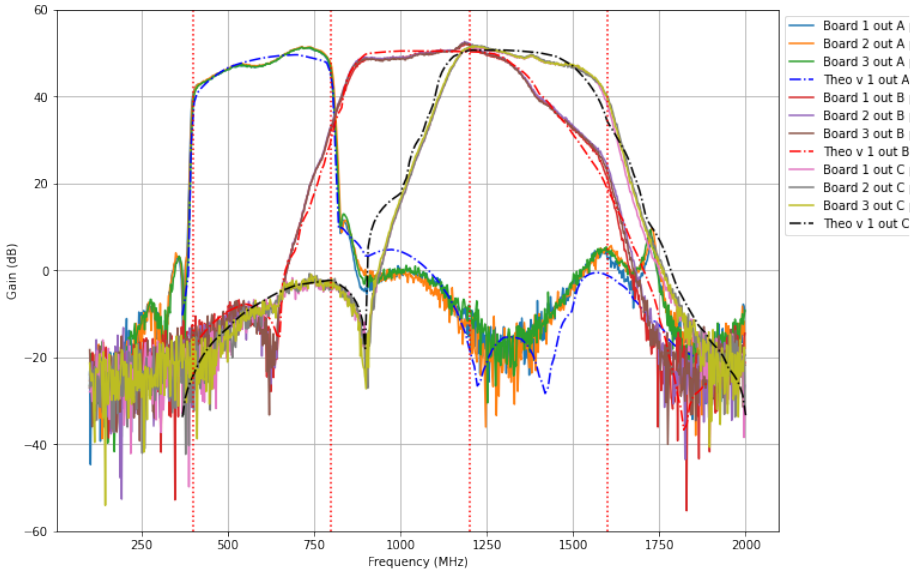

(a) V1

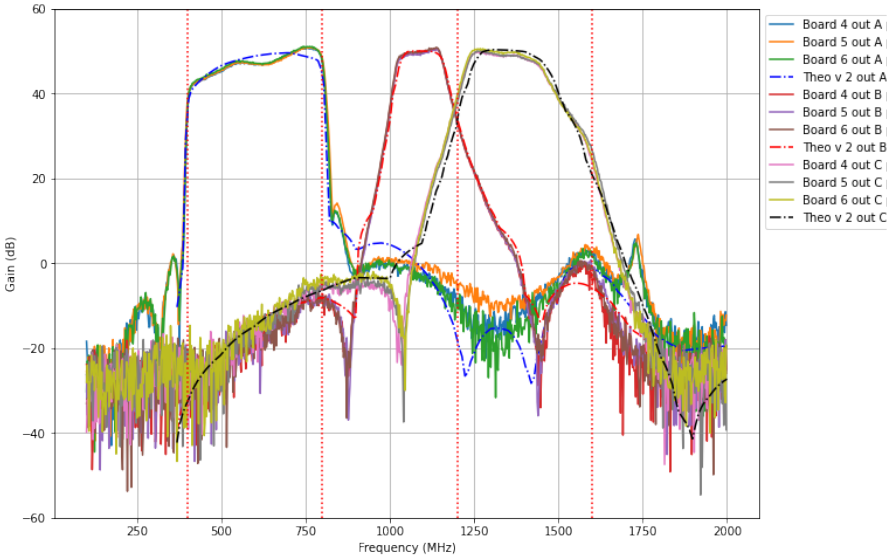

(b) V2

Figure 2.13: UWB feed analog electronics gain a) V1 (boards 1-3) with wider bandpass filters and b) V2 (boards 4-6) with narrower bandpass filters. Each board has three outputs corresponding to the three frequency bands, with out A, B, and C corresponding to the 400-800, 800-1200, and 1200-1600 MHz bands respectively. VNA measurements (solid lines) are shown compared to the theoretical gain from the datasheets (labelled 'Theo', dash-dot lines), with a fairly good match between the two. The edges of the three bands (vertical red dotted lines) are shown at 400, 800, 1200, and 1600 MHz. V1 shows overlap between the two upper bands (800-1200 and 1200-1600 MHz) whereas V2 does not have full frequency coverage.

Chapter 3

Reflectometer

Because redundant arrays such as HIRAX and CHORD require a high level of repeatability between telescopes, it is important that the dishes have a reflective surface that is continuous at the wavelengths of interest and closely matches (on the order of 0.5 mm rms) the shape of the other dishes in the array. The design of the prototype D3A dishes outlined in Section 1.4.4 involves a reflective metal mesh buried in a composite material that provides structural support and is transparent at radio frequencies. Techniques such as photogrammetry and laser tracking can provide precise information on the shape of the composite material composing the surface of the dish. However, the physical front surface of the dish does not coincide exactly with the conductive surface provided by the metal mesh, which is embedded within the composite material. Characterizing the electromagnetic uniformity of the dish therefore requires a different measurement technique to probe the conductive surface through the layers of composite. To measure uniformity, we will use a device known as a reflectometer that uses an open resonant cavity to determine the depth of the conductive mesh [37]. The other primary application of reflectometers is determining the surface resistivity of a material [38], [39].

3.1 Principles of reflectometers

The reflectometer shown in Fig. 3.1 is based on a cylindrical resonant cavity that can sustain resonant modes at frequencies dependent on the geometry of the cavity. However, the reflectometer lacks one of the end plates of the cylindrical cavity (see Fig. 3.1a), b)) and instead is placed against a reflective surface (Fig. 3.1c), d)) that effectively acts as the missing end plate, enclosing the cavity. The resonant frequencies in the completed cavity depends on its length, which varies with the distance between the reflective test surface and the open end of the reflectometer. This offset can be calculated by monitoring the resonant frequencies. For example, the reflective mesh in our dish is buried within the composite material. Placing the reflectometer against a portion of the dish (shown in Fig. 3.2) and determining the offset provides us with the depth of that section of mesh within the dish.

To determine the exact relationship between the distance to the reflective surface and the change in the resonant frequencies, we need to understand the basics of the resonant modes occurring in cylindrical cavities. Adding the loop antenna seen in Fig. 3.1a) to measure the resonant frequencies will change the behaviour of the resonances away from that of an empty cylindrical cavity, and must be understood to calculate the distance. Both the empty cylindrical cavity and the effects of adding an antenna are discussed in the following sections.

3.1.1 Resonant modes in a cylindrical cavity

The resonant modes in a cylindrical cavity include both transverse electric (TE) and transverse magnetic (TM) resonant modes. Fig. 3.3 shows the coordinates of such a cylindrical cavity with z running lengthwise down the cylinder, r in the radial direction, and ϕ along azimuth. In transverse electric modes the z-component of the electric field is zero, leaving the only transverse components. Likewise, TM modes require the z-component of the magnetic field to be zero. The TE and TM modes excited in the cavity are indexed by

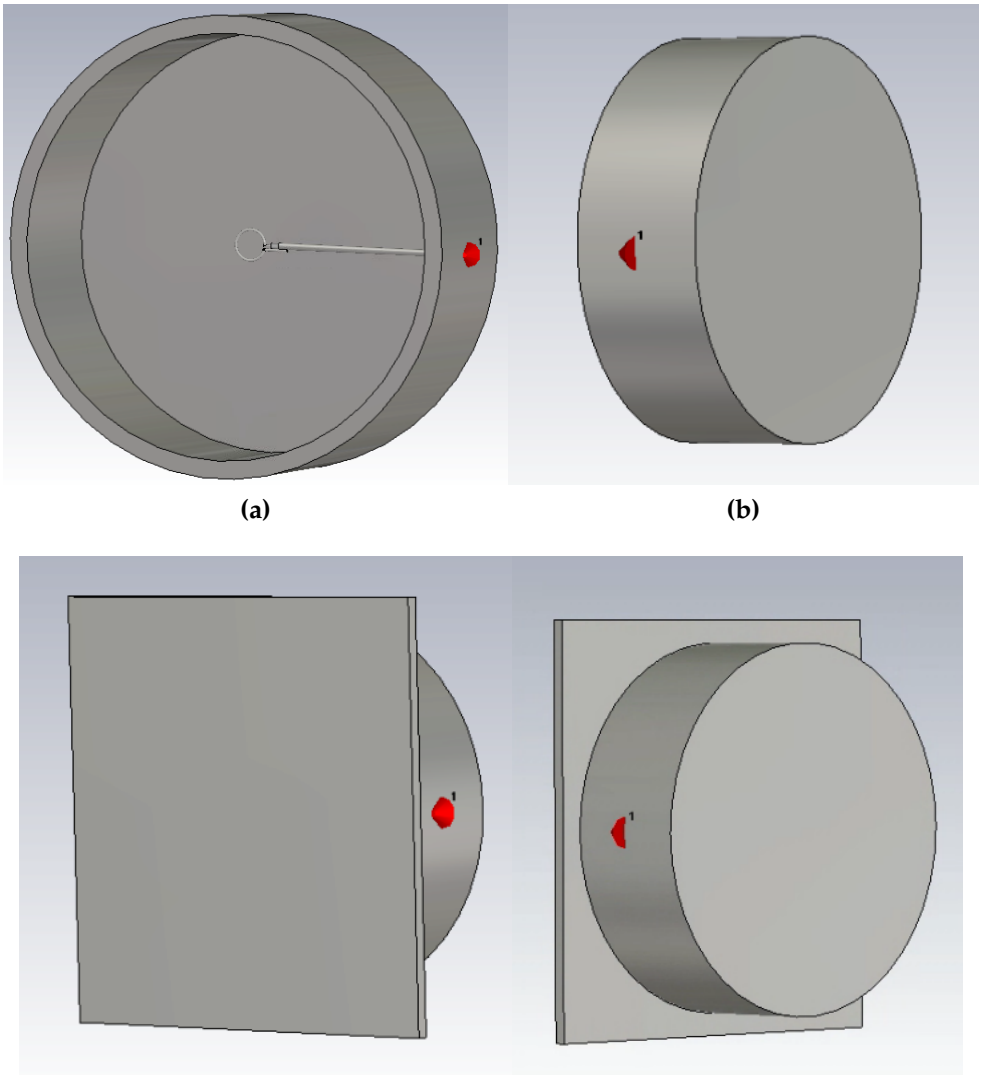

Figure 3.1: Reflectometer model in CST, an electromagnetic simulation software [24], shown with and without a square test plate to demonstrate the use of the reflectometer on a reflective surface. a) Reflectometer front view displaying the lack of one end plate and the loop antenna used to monitor the resonant frequencies in the cylindrical cavity. b) Reflectometer back view. c) Reflectometer front view with the open end of the cavity shown pressed against a square test plate. d) Reflectometer back view with the square test plate.

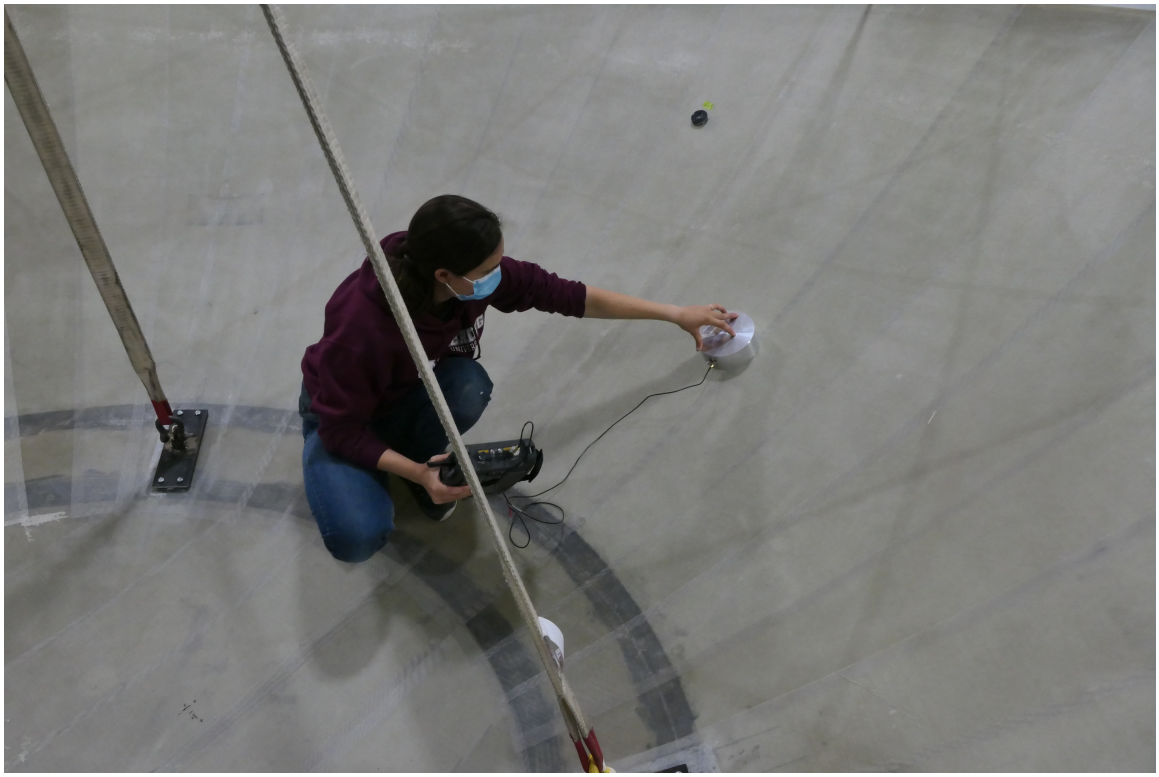

Figure 3.2: Reflectometer pressed by the author's left hand against the inside of the first six meter D3A dish at DRAO, attached to a Fieldfox portable VNA via a cable for reading data. Photo credit: K. Gerodias.

n, m, and l, where n is the azimuthal variation along ϕ, m is the radial variation along r, and l is the variation along the length of the cylinder in the z direction. Figure 3.4 illustrates the effects of the different variations. Having no variations along a given direction would mean a constant field strength in that direction, and adding an variation means the strength increases and decreases, creating a local maximum. For example, in Fig. 3.4c) we have m=3, denoting three radial variations, and we see clearly three lighter rings denoting three local maxima along the radial direction.

The resonant frequencies as derived in [21, Eq. 6.53a] for the TE modes f_{nml}^{TE} are

$$f_{nml}^{\mathrm{TE}} = \frac{c}{2\pi\sqrt{\mu_{\mathrm{r}}\epsilon_{\mathrm{r}}}}\sqrt{\left(\frac{p_{nm}^{`}}{a}\right)^2 + \left(\frac{l\pi}{d}\right)^2} \tag{3.1}$$

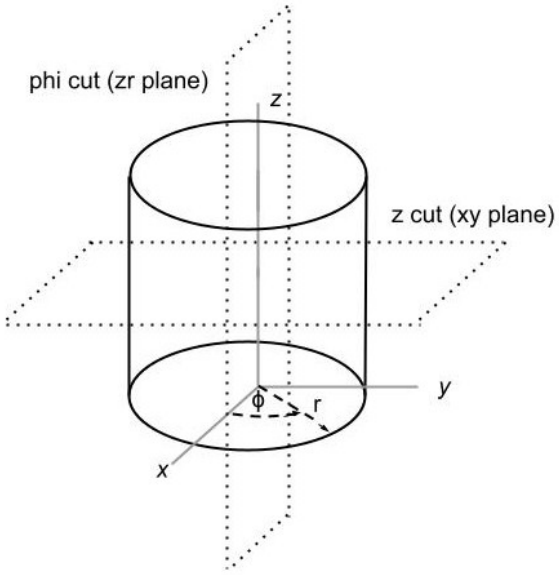

Figure 3.3: Cylindrical coordinates showing z, x, and y along with the radial r and azimuthal ϕ directions. Different planes for viewing 2D slices of the cylinder are shown.

where c is the speed of light, μ_{r} and ϵ_{r} are the relative magnetic permeability and permittivity of the material filling the cavity, a and d are the radius and depth of the cavity, and $p_{nm}^{'}$ is the mth root of the derivative of the nth Bessel function.

Similarly, the resonant frequencies of the TM modes ([21, Eq. 6.53b]) are:

$$f_{nml}^{\mathrm{TM}} = \frac{c}{2\pi\sqrt{\mu_{\mathrm{r}}\epsilon_{\mathrm{r}}}}\sqrt{\left(\frac{p_{nm}}{a}\right)^2 + \left(\frac{l\pi}{d}\right)^2} \tag{3.2}$$

where p_{nm} is the mth root of the nth Bessel function. Note that for TE modes $l \geq 1$, whereas for TM modes $l \geq 0$. Both n and m for both modes must be ≥ 0.

These equations make it possible to derive the depth d of a resonant cavity given the radius and the frequency of a known TE or TM resonant mode. For TE modes, we find that

$$d = \frac{\pi}{\sqrt{\left(\frac{f_{nml}^{\mathrm{TE}}}{\frac{c}{2\pi}}\right)^2 - \left(\frac{p_{nm}^{'}}{a}\right)^2}}. \tag{3.3}$$

where f_{nml}^{TE} is the frequency of the mode and a is the radius of the cavity. The reflectometer takes advantage of this relationship between cavity geometry and resonant mode fre-

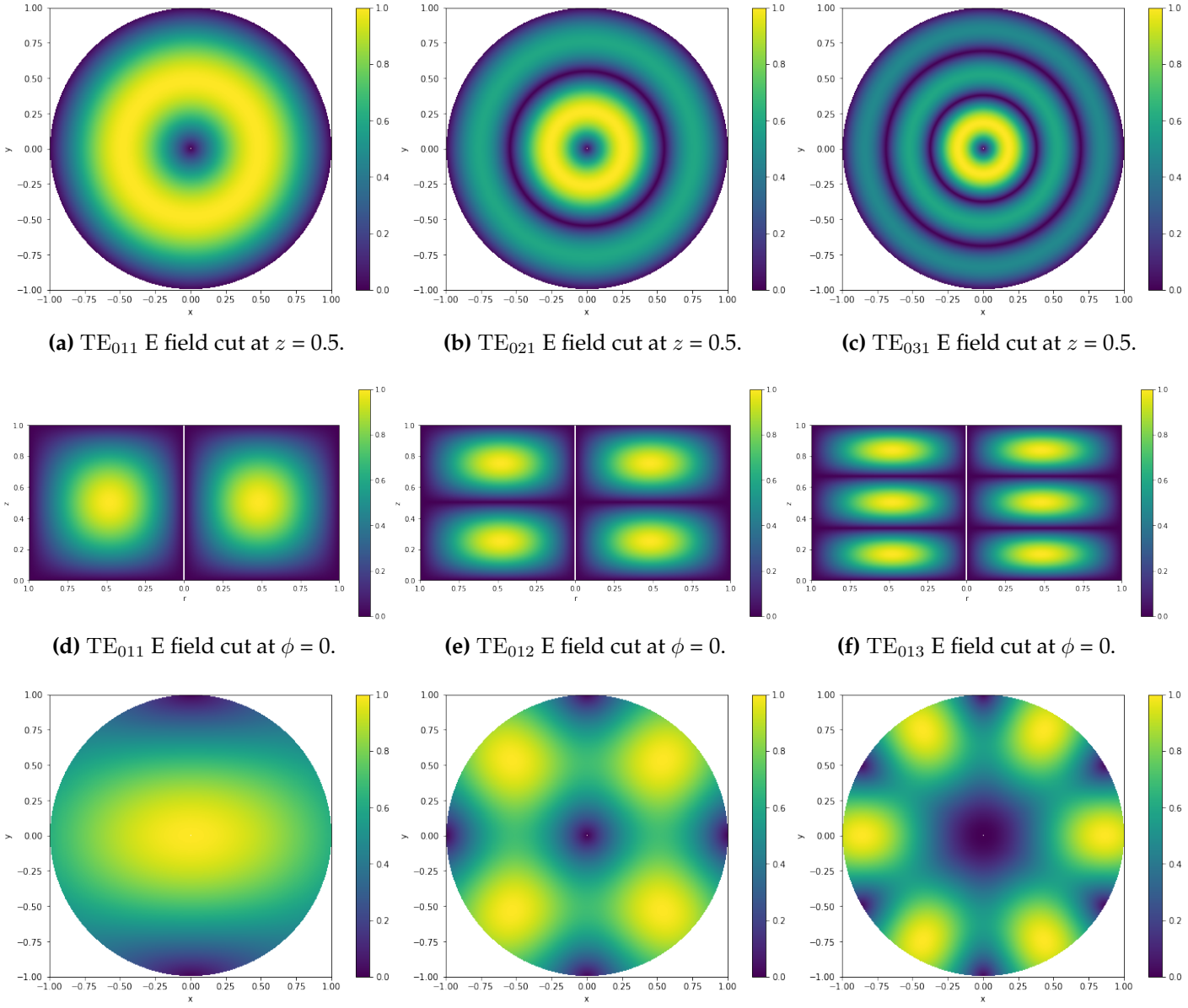

(a) TE_{011} E field cut at $z = 0.5$. **(b)** TE_{021} E field cut at $z = 0.5$. **(c)** TE_{031} E field cut at $z = 0.5$.

(d) TE_{011} E field cut at $\phi = 0$. **(e)** TE_{012} E field cut at $\phi = 0$. **(f)** TE_{013} E field cut at $\phi = 0$.

(g) TE_{111} E field cut at $z = 0.5$. **(h)** TE_{211} E field cut at $z = 0.5$. **(i)** TE_{311} E field cut at $z = 0.5$.

Figure 3.4: TE modes of a cylindrical resonant cavity to illustrate variations. a), b), and c) increase radial variations m from 1 to 3; d), e) and f) increase longitudinal variations l from 1 to 3, and g), h) and i) increase azimuthal variations n from 1 to 3. Each added variation adds a maximum along the given direction.

quency. By creating a cylindrical resonant cavity missing a single end plate and placing the open end against a surface as shown in Figs. 3.1 and 3.2, it is possible to measure the distance to the first electrically reflective layer in the surface (that acts as the second end plate) by monitoring the frequency of a specific resonant mode.

The ideal resonant mode does not require surface current between the cylinder walls and the end plate, as the surface under test may not necessarily be in good electrical contact with the walls. The TE_{011} mode shown in Fig. 3.5 is therefore a good candidate as the fields and surface current die to zero at the junction between the cylinder walls and the end plates. This mode has a simple structure consisting of only a single variation (increase and decrease in field strength) in the ϕ, and z directions, and has a lower frequency compared to most other modes because the resonant frequency tends to increase with the number of variations.

One drawback is that the TE_{011} mode is colocated in frequency with the TM_{111} mode shown in Fig. 3.6, which has maximum surface current between the walls and endplates. To be able to use the TE_{011} mode to determine depth, the cavity must be modified slightly to separate the two modes so that the resonance does not depend on contact between the walls and endplates. One recommendation includes attaching a crosswire across the diameter of the cavity stretching from one curved wall to another (shown in Fig. 3.7) to short out the TM_{111} mode [37]. However in Section 3.3 it is shown that having an antenna within the cavity already perturbs the modes enough to separate the frequencies of the TE_{011} and TM_{111} mode, rendering any further alterations unnecessary.

3.1.2 Measuring the resonances

At the resonant frequencies of the TE and TM modes, the resonant cavity stores a large amount of energy. First an antenna is placed in the cavity, the design of which is discussed later in Section 3.2. The antenna is excited and the reflected power, or S_{11} parameter (see Appendix A), is measured across a broad frequency range where the desired resonances occur. The resonances appear as sharp dips in the S_{11} accompanied by a phase change

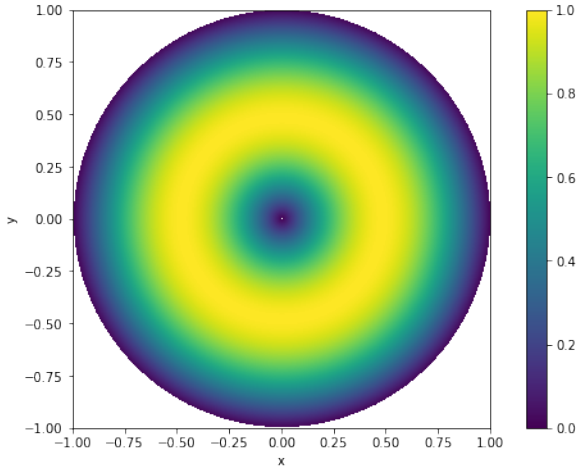

(a) E field cut at $z = 0.5$.

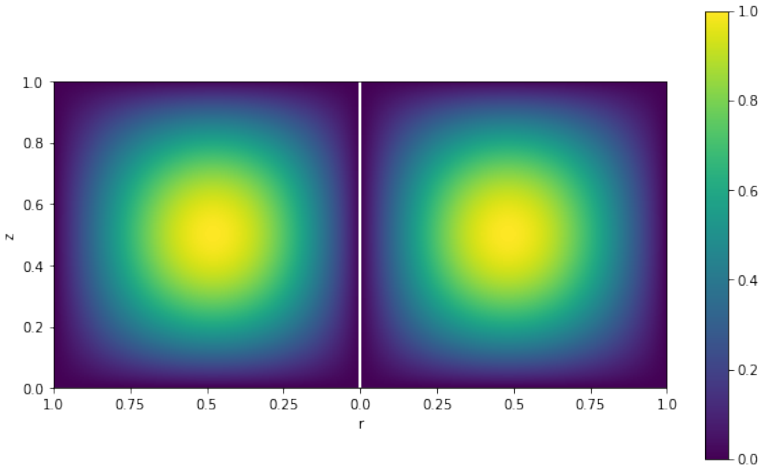

(b) E field cut at $\phi = 0$.

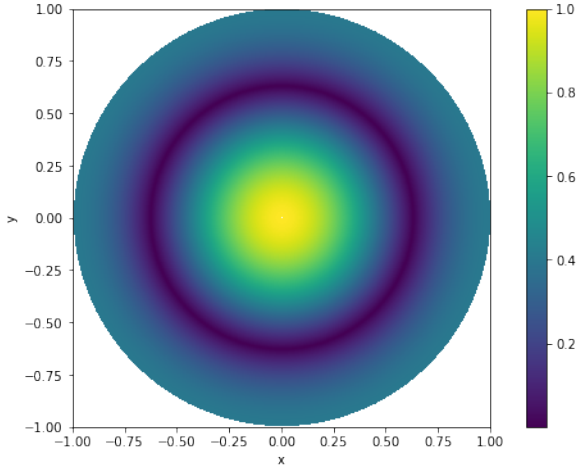

(c) H field cut at $z = 0.5$.

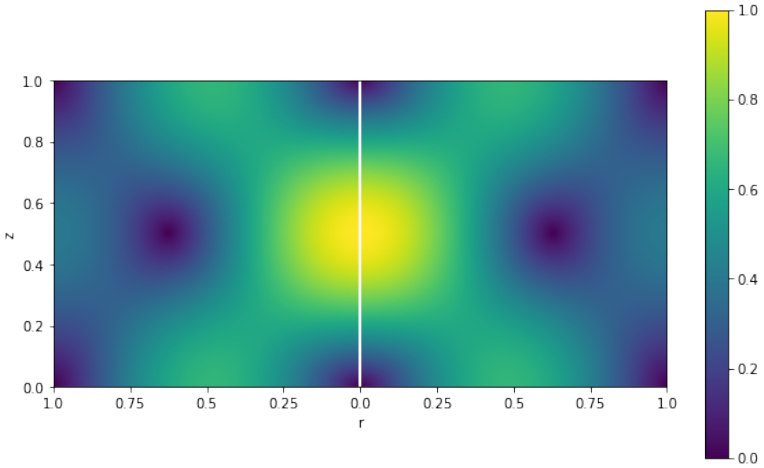

(d) H field cut at $\phi = 0$.

Figure 3.5: Calculated TE_{011} electric and magnetic field magnitude. Fields are normalized to the maximum magnitude in the given cut, and are calculated from Eq. 6.54 in [21]. a) E field cut at $z = 0.5$. b) E field cut at $\phi = 0$. c) H field cut at $z = 0.5$. d) H field cut at $\phi = 0$. As expected from the TE_{011} mode no variations appear along ϕ, and a single variation occurs along r and z. Because fields go to zero at the corner junctions between the cylindrical walls and circular end plates, the surface current goes to zero in those locations. As such this mode does not rely on electrical contact between the walls and end plates.

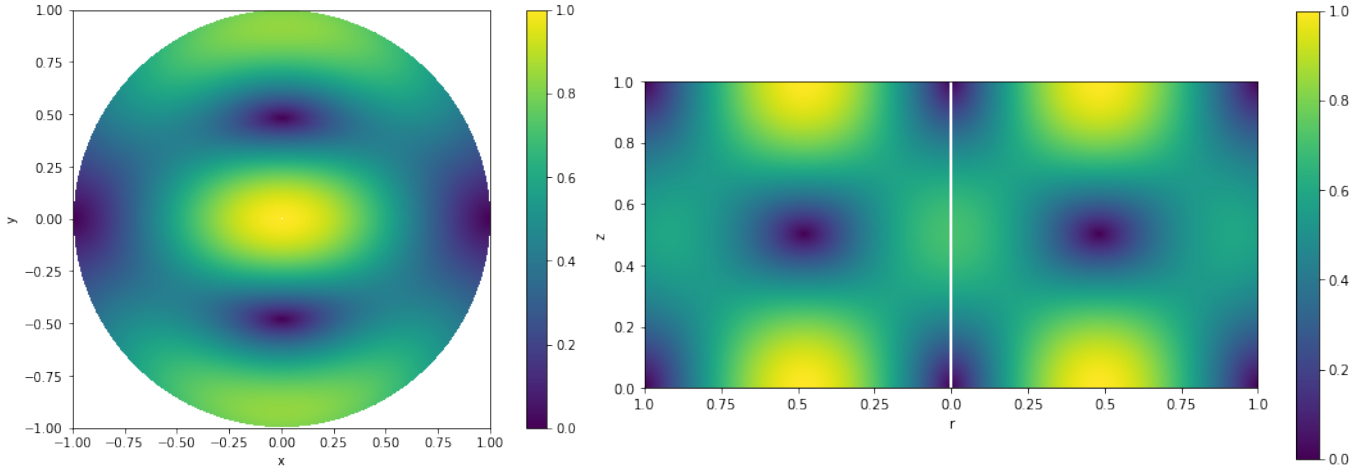

(a) E field cut at $z = 0.5$.

(b) E field cut at $\phi = 0$.

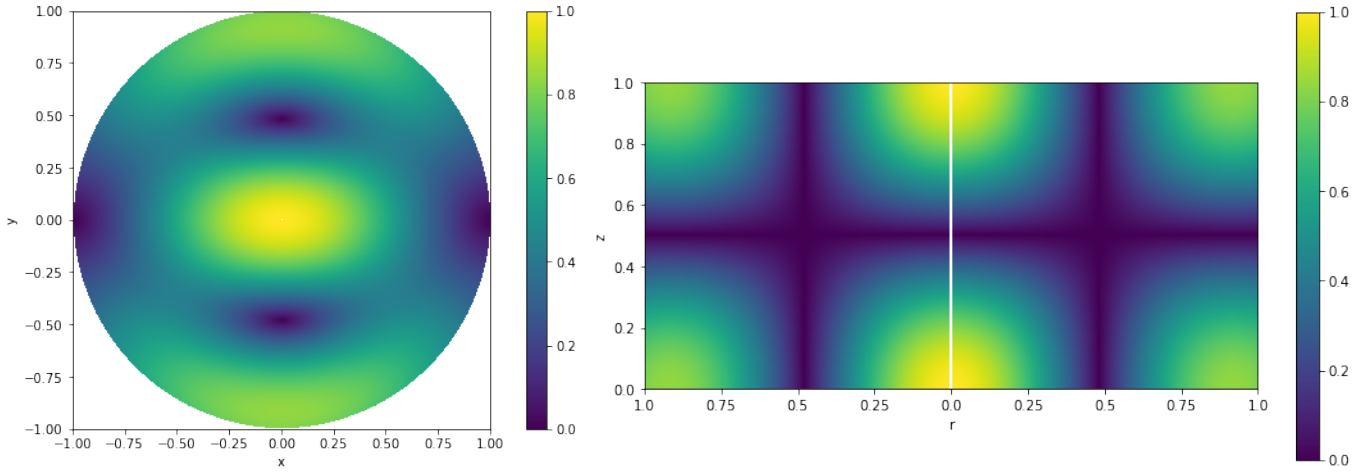

(c) H field cut at $z = 0$.

(d) H field cut at $\phi = 0$.

Figure 3.6: Calculated TM_{111} electric and magnetic field magnitude. Fields are normalized to the maximum magnitude in the given cut, and are derived from [21], [40] and [41]. a) E field cut at $z = 0.5$. b) E field cut at $\phi = 0$. c) H field cut at $z = 0$. d) H field cut at $\phi = 0$. As expected from the TM_{111} mode a single variation occurs along ϕ, r and z. Because fields persist in the corner junctions between the cylindrical walls and circular end plates, the surface current is nonzero in those locations. As such this mode relies on electrical contact between the walls and end plates and depends sensitively on intermittent contact.

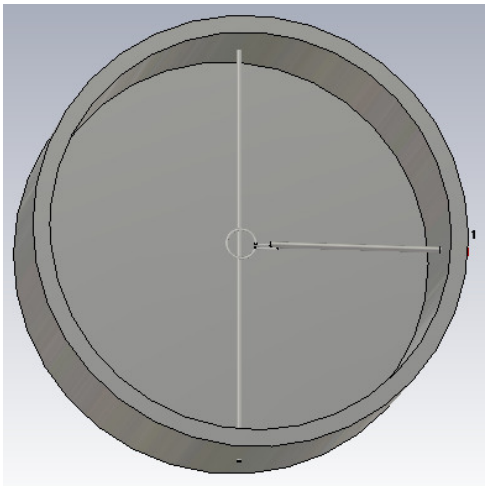

Figure 3.7: Crosswire in CST model running across the diameter of reflectometer underneath and perpendicular to the antenna.

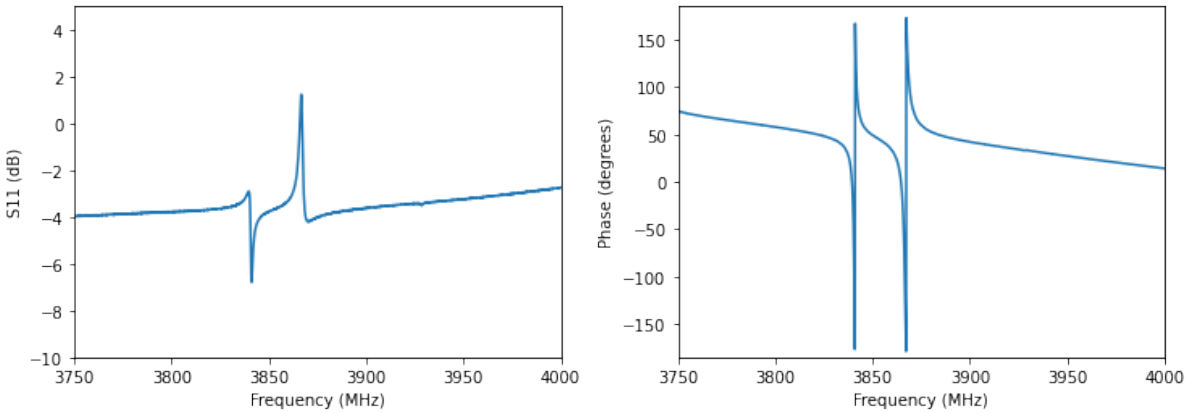

Figure 3.8: Resonances appearing in reflectometer S_{11} a) magnitude and b) phase.

that sweeps through 360 degrees, as shown in Figure 3.8. The center of dip provides the resonant frequency of the corresponding mode and can be tracked to provide information on the depth to a reflective surface.

Changes in the resistivity, rather than producing an offset in the resonant frequencies, are expected to affect the quality factor (Q factor) of the resonances [39]. The Q factor is a parameter that provides information on the energy storage versus dissipation of a resonance. The higher the Q factor, the better the resonance is at storing energy; the lower the

Q factor, the less time (or fewer oscillations) it will take for the resonance to lose its energy. The Q factor can be measured from the width of the dips in the S_{11} parameter, requiring a fitting function for the dips. An absolute measurement of the resistivity of a reflective surface requires knowledge about the resistivity of the reflectometer's inner cavity walls. Using the reflectometer to provide information on resistivity is not explored in this initial study; instead the focus is on depth measurements as the priority is to determine the variance of the mesh depth within the dish.

The S_{11} measurement is done using a tool such as a vector network analyzer (VNA) and sweeping the S_{11} parameter across frequency. To perform the measurement on the large dishes in the field it is convenient to have a portable analyzer. We use the portable Fieldfox N9914A [42] for the majority of the measurements, including those of the first D3A six meter dish and calibration measurements of flat metal plates in the lab. Further flat surface measurements in the lab are carried out using the E5080B ENA Vector Network Analyzer [43].

3.2 Reflectometer design

3.2.1 Reflectometer geometry

Different cylinder geometries produce reflectometers with different resonant frequencies. Although the reflectometer is used on six meter dishes that are constructed for cosmology with wavelengths 0.2 to 1 m (300 to 1500 MHz), the change in the mesh depth must be determined on a sub-mm scale. It is neither desirable nor practical to build a reflectometer with resonant frequencies near the observed frequencies; one reflectometer design with the TE_{011} mode at 470 MHz has a half meter length and diameter.

The McGill reflectometer is based on a design that was developed for characterizing the KAT-7, which uses the TE_{011} mode at 3.7 GHz [37]. The McGill reflectometer is created with similar geometry, as outlined in Table 3.1, with a shorter length than radius to increase sensitivity to changes in depth. Note that the resonant frequencies depend

Geometry	Size (mm)
Inner radius	75
Outer radius	81
Inner length	50
Outer length	56

Table 3.1: McGill reflectometer geometry.

only on the inner length and radius that define the cavity, not the outer dimensions. The McGill reflectometer design provides a TE_{011} mode for an empty cavity at 3.863 GHz and is a compact handheld device.

3.2.2 Reflectometer antenna

The McGill reflectometer antenna is modelled after the loop antenna used in the KAT-7 reflectometer. The antenna consists of a small wire loop near the center of the cavity both radially and vertically. In the case of the McGill reflectometer, shown in Fig. 3.9, a piece of copper wire (1.2 mm thickness) is bent into a circular shape (around a through punch selected for its diameter) and soldered onto a stiff coaxial cable ending in an SMA connector. The SMA connects on the inner wall of the reflectometer to a bulkhead SMA that extends through the reflectometer wall to provide an SMA connection on the outer wall. An external coax cable is attached to the SMA bulkhead on the outer wall and carries the signal to the analyzer.

The radius of the KAT-7 reflectometer antenna is 3 mm. Electromagnetic simulations using CST [24] are run for the McGill reflectometer to find the optimum antenna radii. Figure 3.10 shows the S_{11} parameter against frequency with varying loop radii (numbers are in cm) when the reflectometer is flush against a perfectly conductive test plate. Note that the two dips close to the nominal 3.863 GHz are the TE_{011} and TM_{111} modes, which in an empty cavity are colocated; we will discuss mode identification in Section 3.3. The ideal antenna should provide a significant sharp resonant spike that makes it easier to

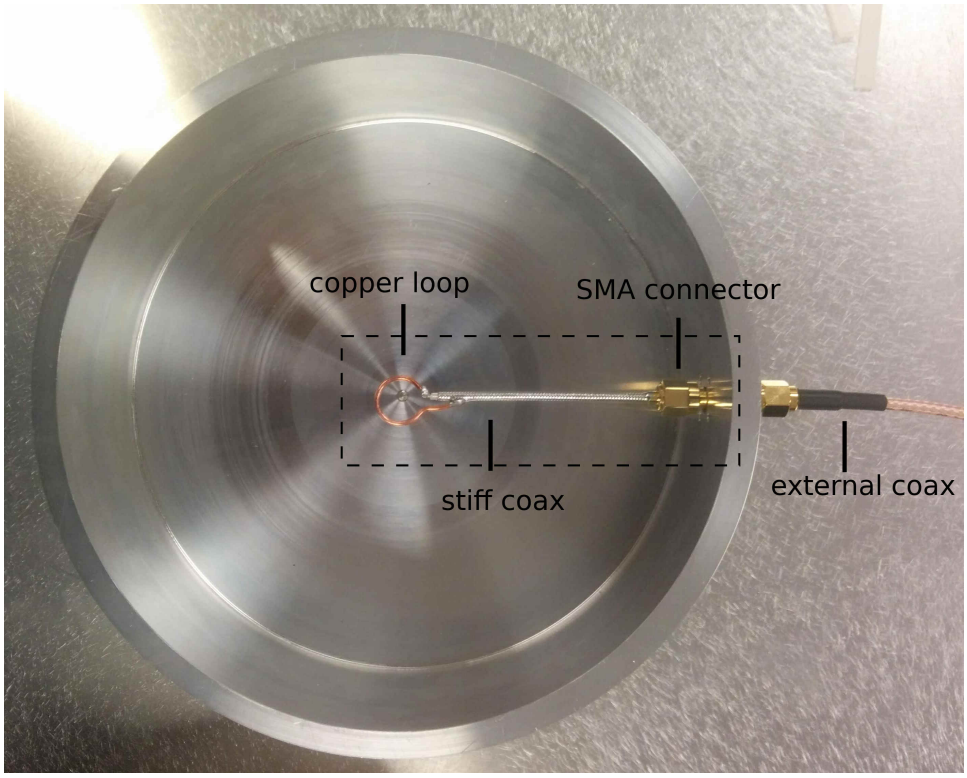

Figure 3.9: The reflectometer antenna outlined in the dashed black line is built from a copper loop soldered to a stiff coax cable terminating in an SMA connector, and is attached to the inner reflectometer wall.

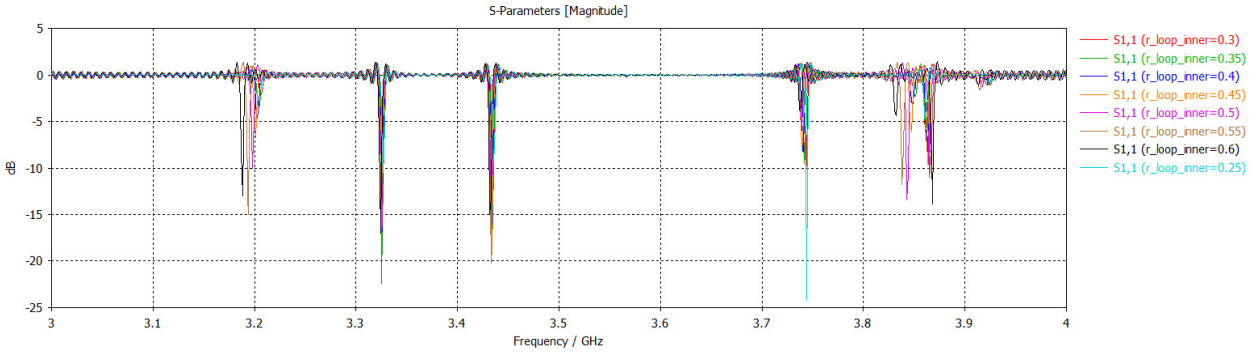

Figure 3.10: CST simulated S_{11} parameters of the reflectometer flush against a metal test plate with different antenna radii (listed in cm).

locate the precise frequency of the resonance. Examining the shapes of the two dips close to 3.863 GHz, a diameter of approximately 5 mm is chosen.

Experimental data varying the antenna size are collected to explore the effects of different sizes of antennas. Three different antennas are constructed using copper wire with a 1.2 mm diameter, with internal radii of approximately 2.3, 5, and 12 mm, and are tested on a flat painted metal surface (a dryer) as shown in Fig. 3.11. From the data shown in Fig. 3.11 we can see that 2.3 and 5 mm radius antennas agree fairly well, though the pair of S_{11} dips close to 3820 GHz in Fig. 3.11b) are slightly closer together with the 2.3 mm radius antenna than with the 5 mm radius antenna. As we want to isolate only the TE_{011} mode, the 5 mm radius is preferred as the resonances are farther apart. The 12 mm radius antenna is noticeably different from the other two, with resonances farther apart. This trend of separating and diminishing peaks with increased loop radius shows slightly in the 6 mm radius simulation run from Fig. 3.10. One possible explanation is that the wire length of the loop antenna is approaching the wavelengths we are observing; 3.863 GHz corresponds to a wavelength of 78 mm, and 2 π r for the circumference of the 12 mm antenna gives 63 mm. The large antenna is therefore no longer acting as an 'electrically small' antenna but rather as a large loop antenna with different electrical characteristics [18]. The following simulations and measurements presented in this thesis use the 5 mm antenna as the standard, following the precedent set by the KAT-7 reflectometer using an electrically small antenna.

As can be seen in both simulation and measurements, the size of the antenna affects the S_{11} parameter not only in S_{11} spike size but also location. This shift could be problematic as we want the peak location to give us information about the depth to the closest reflective surface. Two possible ways to deal with the complicated electromagnetic situation caused by the addition of an antenna are to simulate the effects or to measure the reflectometer performance on a precisely known surface to be able to calibrate out shifts in the frequency not caused by a change in depth to the reflective surface under test. Simulations are discussed in Section 3.3 and calibration in Section 3.6.1.

Figure 3.11: a) Reflectometer testing of different antenna sizes using the Fieldfox network analyzer, shown along with b) the 12 mm antenna, c) the 5 mm antenna, and d) the 2.3 mm antenna.

3.2.3 Reflectometer construction

Initial machining of the reflectometer's cylindrical aluminum cavity was carried out by S. Tartakovsky and E. Eagan using the McGill Physics machine shop. The schematics for the cavity are displayed in Appendix B courtesy of S. Tartakovsky. The aluminum cavity was further modified to include an SMA bulkhead, and the 5 mm antenna was constructed (as discussed in Section 3.2.2) and installed by the author. The 2.3 mm and 12 mm antennas are constructed later to explore the effects of changing the antenna radius and confirm the CST simulations that are run prior to construction as discussed previously in Section 3.2.2. The 5 mm antenna and physical cavity geometry are replicated in an electromagnetic simulator to determine expected behaviour, as discussed in the next section.

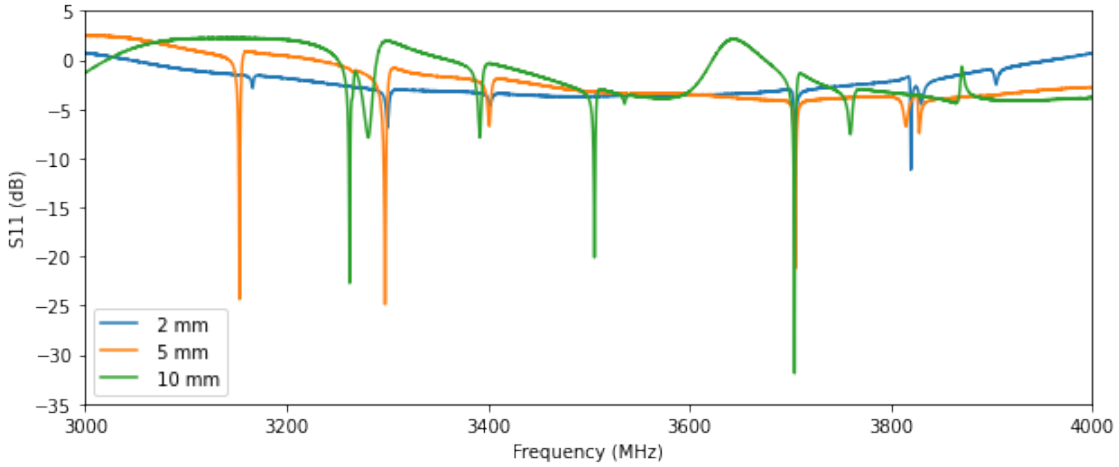

(a) Full tested frequency range.

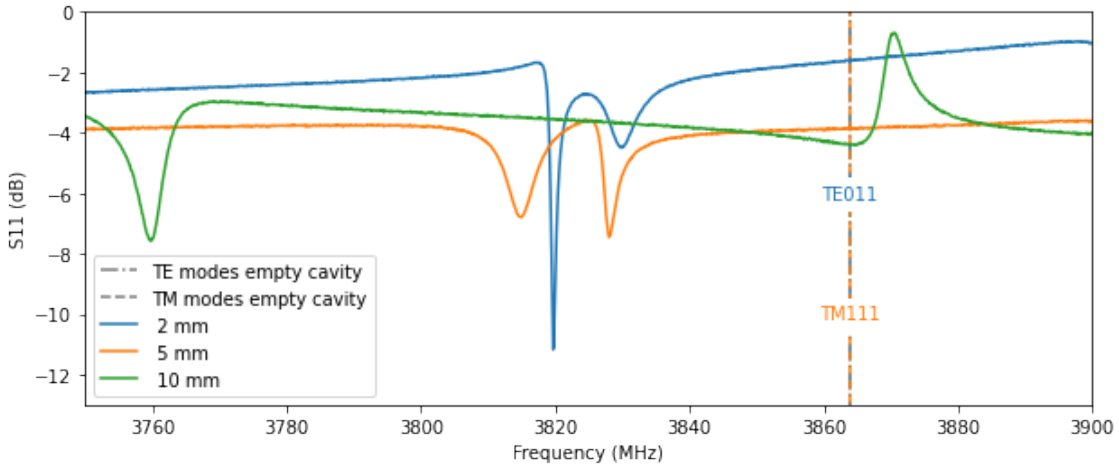

(b) Zoomed close to 3.863 GHz TE_{011} mode.

Figure 3.12: Reflectometer test results with a) full test frequency range, and b) zoomed in both frequency and magnitude, comparing antennas with 2.3 mm (blue), 5 mm (orange) and 12 mm (green) radius. The test is performed on painted metal surface causing an offset to the reflective surface and therefore lower than theoretical resonant frequencies.

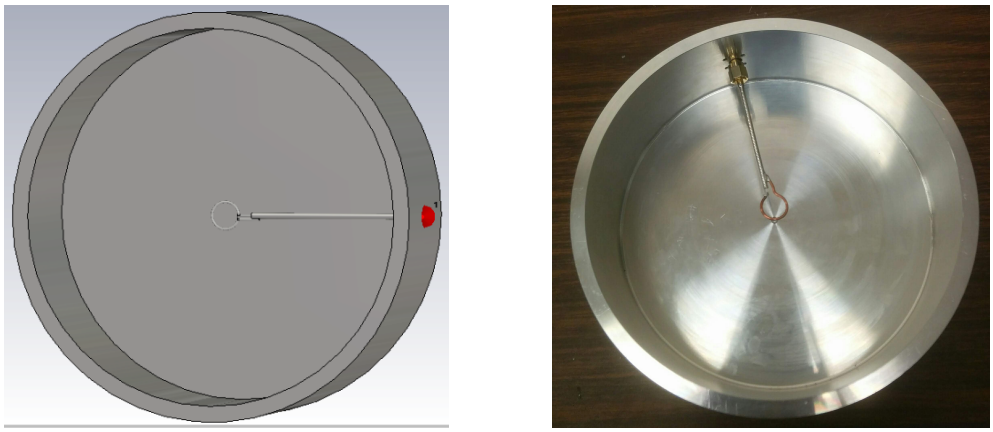

(a) (b)

Figure 3.13: a) CST model of reflectometer. b) Physical reflectometer built in lab. The dimensions of the reflectometer are listed in Table 3.1.

3.3 CST simulations

The addition of the antenna in the reflectometer shifts the positions of the resonant modes away from the calculated frequencies expected in an empty cavity. To compute the resonance shifts caused by the antenna, the system is modelled using CST. Two different reflectometer configurations are run: 1) the cylinder with the antenna as shown in Fig. 3.13a), and 2) the cylinder with the antenna and a crosswire for TM_{111} mode suppression [37] as previously shown in Fig. 3.7. The crosswire has a 1 mm radius and is located 5 mm below the antenna running from wall to wall perpendicular to the direction of the antenna coax. These two configurations are then compared to the theoretical mode frequencies in an empty cylindrical cavity calculated using Eqs. 3.1 and 3.2.

The results of the comparison are shown in Fig. 3.14. As expected a significant difference is found between simulated resonances with an antenna (seen in the sharp dips in S_{11} magnitude) and the calculated empty cavity resonant frequencies (vertical lines). Notably two resonant dips appear close to the calculated frequency for the 3.863 GHz empty cavity TE_{011} mode both with and without the crosswire. Because the crosswire does not immediately simplify our mode suppression or identification problems, it is not used in

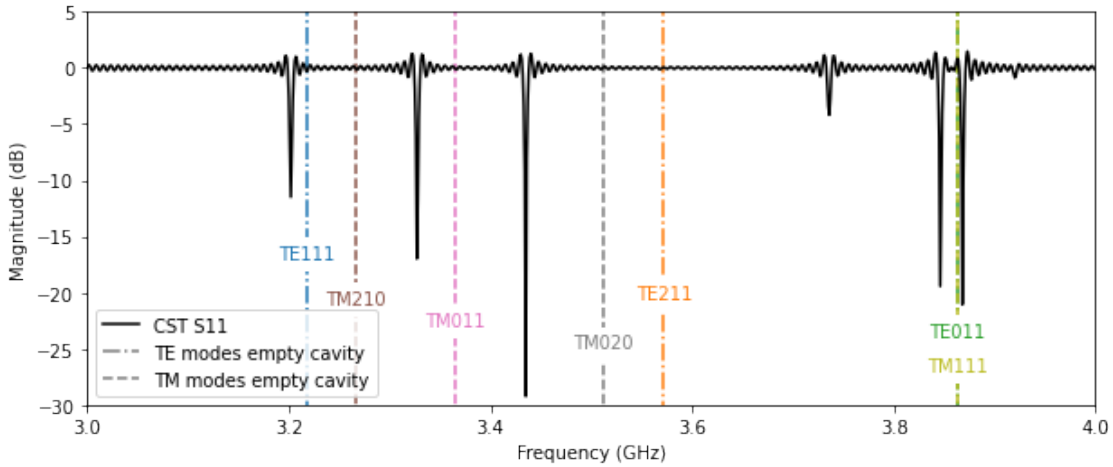

(a) Without crosswire.

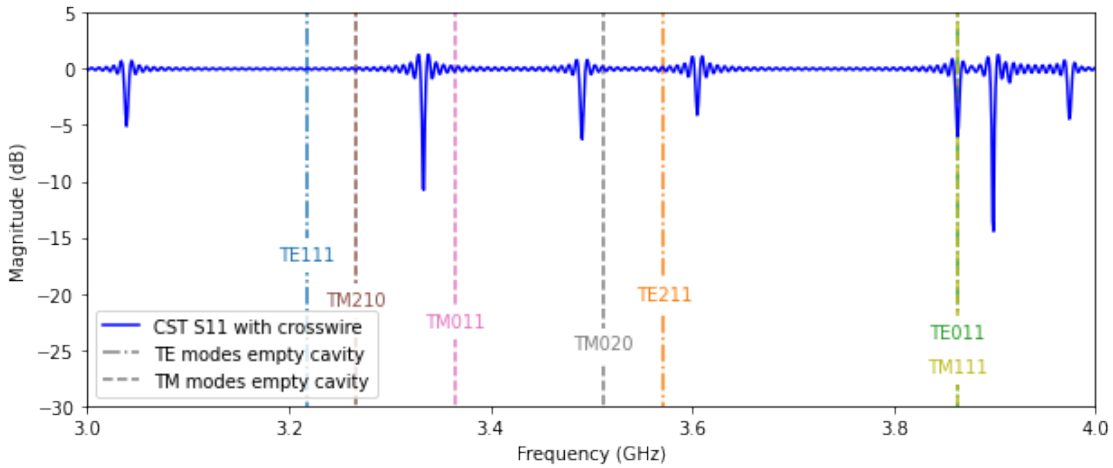

(b) With crosswire.

Figure 3.14: CST simulated reflectometer S_{11} a) without a crosswire and b) with a crosswire compared to the calculated location of labelled resonant modes with an empty cylindrical cavity. The antenna inside the cavity perturbs the resonant modes and shifts them away from the expected frequencies. Notably the TE_{011} and TM_{111} modes, which are colocated in an empty cavity, are separated in the simulation.

the physical system (Fig. 3.13b)) and the analysis is continued with the simpler model without the crosswire.

3.3.1 Resonance mode identification

Further investigation is required to determine which, if either, of the two dips in the S_{11} near the TE_{011} mode in Fig. 3.14a) corresponds to the TE_{011} mode, for which CST monitors are used. CST monitors allow the user to request specific information prior to running the simulation that is not typically saved during a simulation run, which is often detailed frequency-specific information. The monitors used for our purposes provide the electric field, magnetic field, and surface current at pre-selected frequencies. The results of monitors at the 3.865 GHz and 3.843 GHz dips are shown in Figs. 3.15 and 3.16.

The monitor results compared to the expected TE_{011} and TM_{111} fields in Figs. 3.5 and 3.6 respectively show that the dip at 3.865 GHz corresponds to the TE_{011} mode, and the dip at 3.843 GHz corresponds to the TM_{111} mode. Although the calculated modes in an empty cylinder have the TE_{011} and TM_{111} modes colocated in frequency, here the presence of the antenna has caused the modes to shift to two distinct frequencies. This separation is a benefit to us as we wish to isolate and use the TE_{011} mode, and means that exploring mode suppression techniques such as the crosswire is no longer necessary. As mentioned previously the TE_{011} mode is desirable because it does not rely on surface currents between the end plate and the cavity walls. This behaviour is confirmed in the simulations as the TE_{011} surface current can be seen going to zero at the edge of the cavity walls in Fig. 3.15, a contrast to the TM_{111} surface current in Fig. 3.16 where it is at a maximum at the edge.

3.3.2 Frequency change with offset

Offsets of the metal test plate are simulated to compare the resonant mode frequency shifts relative to the theoretical predictions made by Eq. 3.3. The reflectometer simulation

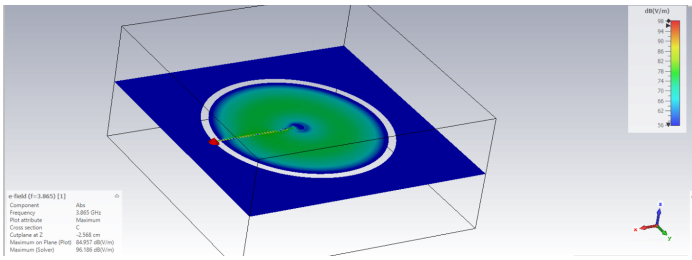

(a) E field cut (xy plane).

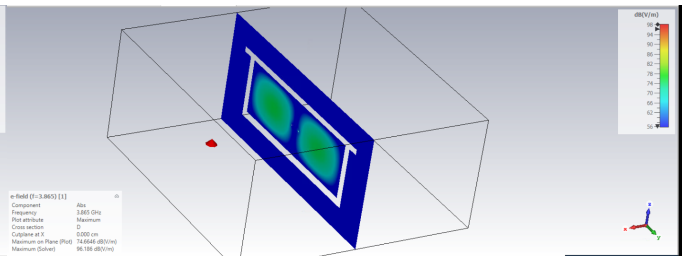

(b) E field cut (yz plane).

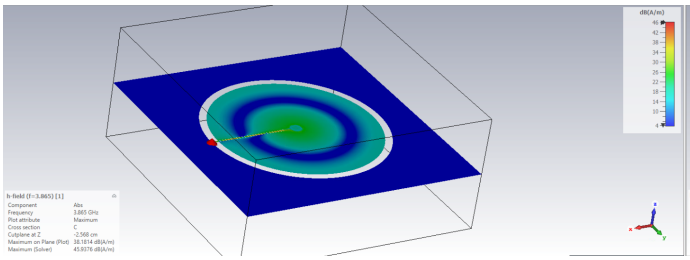

(c) H field cut (xy plane).

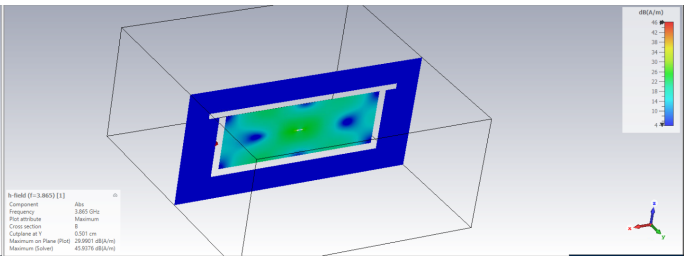

(d) H field cut (xz plane).

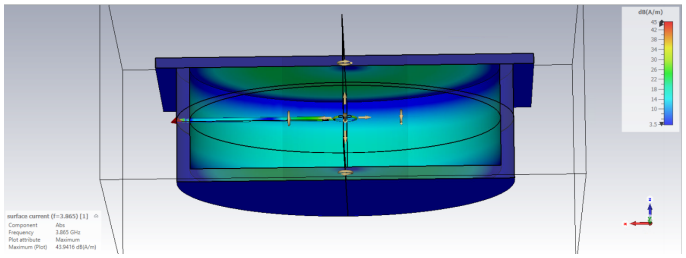

(e) Surface current.

Figure 3.15: Simulated electric and magnetic field magnitude and surface current at 3.865 GHz. a) E field cut (xy plane). b) E field cut (yz plane). c) H field cut (xy plane). d) H field cut (xz plane). e) Surface current. The fields of this resonant mode at 3.865 GHz match the fields of the TE_{011} mode in Fig. 3.5.

is rerun with the plate offset from the cavity walls to determine the effects of relatively small and large changes in depth. Detecting small changes on the order of 0.1 mm allows verification that the variance in the mesh depth is within the 0.5 mm requirement for CHORD. Understanding the effect of larger offsets ($\lesssim$1.5 mm) is important as the reflectometer is offset from the mesh because of a surface composite layer and the curvature of the dish. The physical reflectometer offsets are tested using sheets of roughly 0.12$\pm$0.01 mm thick paper with ten sheets measured to be 1.25 mm, so the simulation offsets are chosen to be 0.125 and 1.25 mm to gather information on large and small offsets.

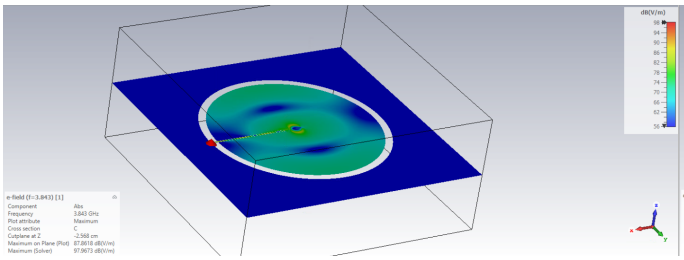

(a) E field (xy plane).

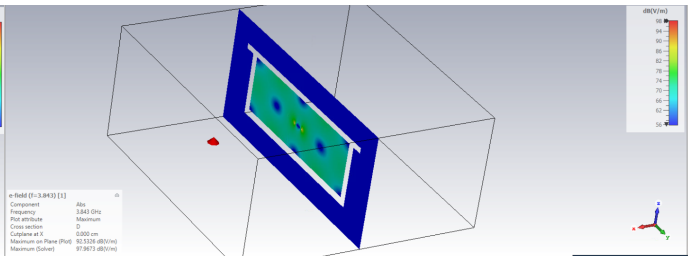

(b) E field (yz plane).

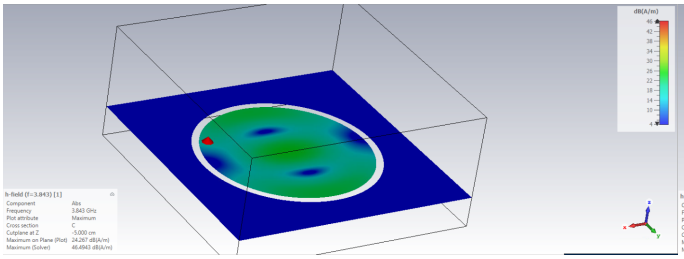

(c) H field (xy plane).

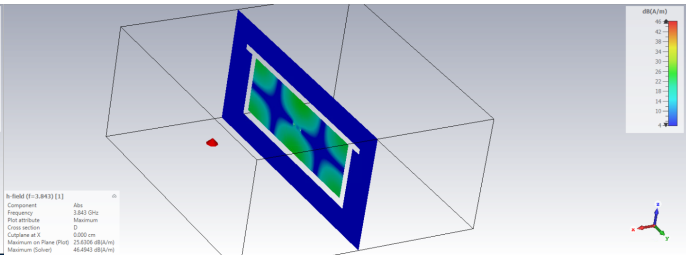

(d) H field (xz plane).

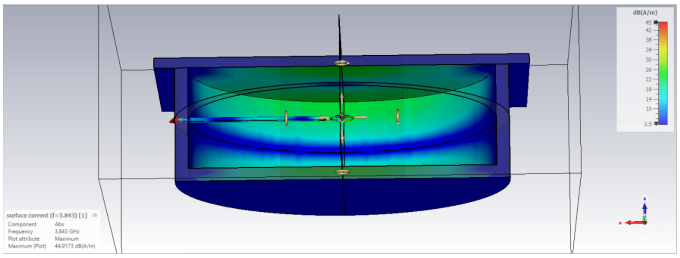

(e) Surface current.

Figure 3.16: Simulated electric and magnetic field magnitude and surface current at 3.843 GHz. a) E field cut (xy plane). b) E field cut (yz plane). c) H field cut (xy plane). d) H field cut (xz plane). e) Surface current. The fields of this resonant mode at 3.843 GHz match the fields of the TM_{111} mode in Fig. 3.6.

These simulations are compared to the zero offset simulation in Fig. 3.17. The 0.125 mm simulation produced a 5.0 MHz shift in frequency, and the 1.25 mm simulation gave a 48.0 MHz shift, or an average shift of 4.8 MHz per sheet of paper (0.125 mm). The theoretical change in frequency from the same endplate offset calculated using Eq. 3.1 are 5.8 MHz per sheet of paper, meaning that the CST simulation gives an underestimate of depth. In Section 3.4.2 we see that the CST simulations do give an underestimate compared to the physical reflectometer.

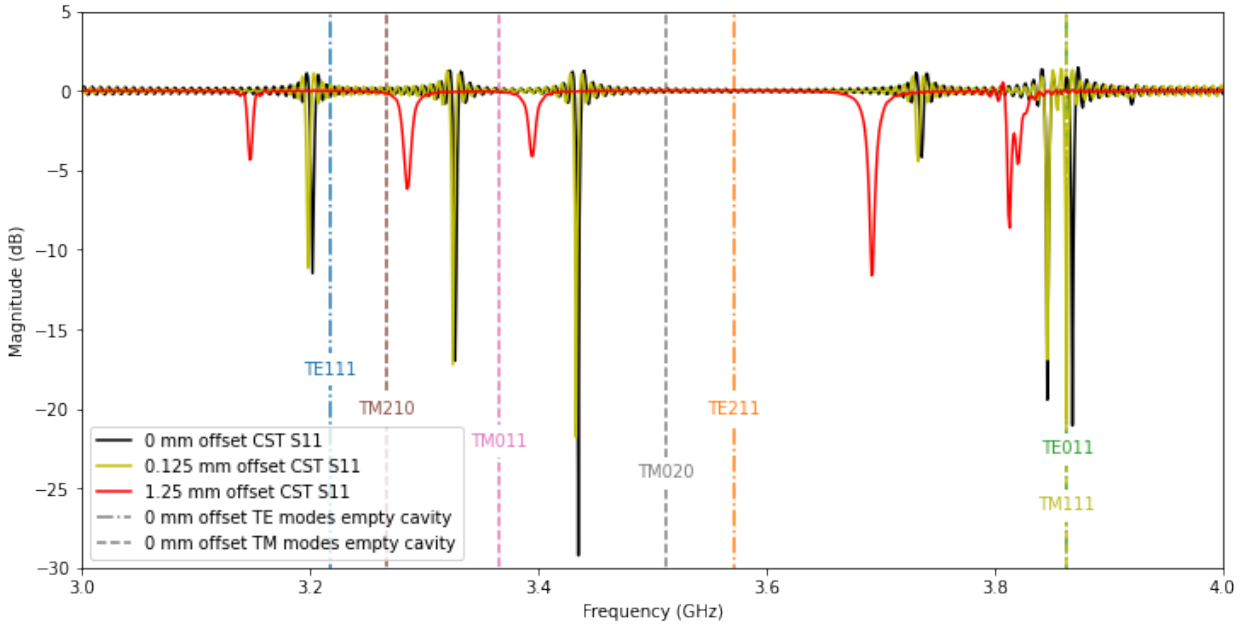

Figure 3.17: CST reflectometer simulated S_{11} parameters with the endplate offset by 0 mm (solid black), 0.125 mm (solid yellow), and 1.25 mm (solid red). The nominal TE and TM modes for an empty cylindrical cavity with no offset are shown (dash-dotted and dashed lines). With increasing endplate offset and therefore increasing cavity length, the resonant modes represented by dips in the S_{11} shift down in frequency.

The CST simulations have demonstrated that we can pick out the TE_{011} resonant mode, and that the mode decreases in frequency with a at a rate of 4.8-5 MHz per 1.25 mm offset over the first 1.25 mm of offset, which is similar to the theoretical increase of 5.8 MHz per 1.25 mm. We have shown that the VNA used to read the S_{11} parameters of the reflectometer must be able to resolve a 5 MHz shift in peak frequency to provide information about the offset of a reflective endplate on the order of 0.1 mm.

3.4 Reflectometer data analysis

Data from the reflectometer are acquired by attaching a coax cable to the an SMA bulkhead connector accessible on the exterior of the cavity, as shown in Fig. 3.9. This coax cable runs to a network analyzer capable of sweeping the S_{11} parameter against frequency with

a sub-MHz resolution. Frequency sweeps of S_{11} are best exported as single parameter Touchstone files (s1p) [44]; when exporting with csv or txt it is important that both the magnitude and phase of the complex S_{11} parameter are saved, as both can be used to detect resonances and can be compared for quality control. Python code has been created to handle the reflectometer data and includes multiple methods of detecting resonances in the S_{11} data using the magnitude and phase. Class reflectometerDepth uses the detected resonant frequencies to generate the depth and provides convenient plotting functionality.

3.4.1 Resonance detection

Class reflectometerDepth currently employs three main methods of peak detection which complement each other and provide fairly effective error catching. The strengths and weaknesses of each method are discussed below. Plotting all three provides the quickest way to catch anomalous detections and measurements which can then be examined more closely using the many debug plots provided by reflectometerDepth.

Magnitude peak finder

The magnitude peak finder applies Scipy Signal's `findpeaks` function [45] to both a positive and negative copy of the S_{11} magnitude in decibels (dB). While the resonances are an absorption of energy within the cavity and hence a drop in the S_{11} the resonances can show up as peaks because of the accompanying phase shifts. In Fig. 3.18a) we see an example where the TE_{011} mode (the resonance to the right of the empty cavity TE_{011} and TM_{111} mode, which was identified as the TE_{011} mode in the simulations), is left undetected as it manifests half as a peak and half as a dip. Scipy's findpeaks function has a number of arguments to fine tune peak selection, but the variations in peak height, width, and the background S_{11} level make it difficult to find parameters that will work for all measurement sets. To provide comparisons for quality control we introduce two more peak selection methods that rely on the phase.

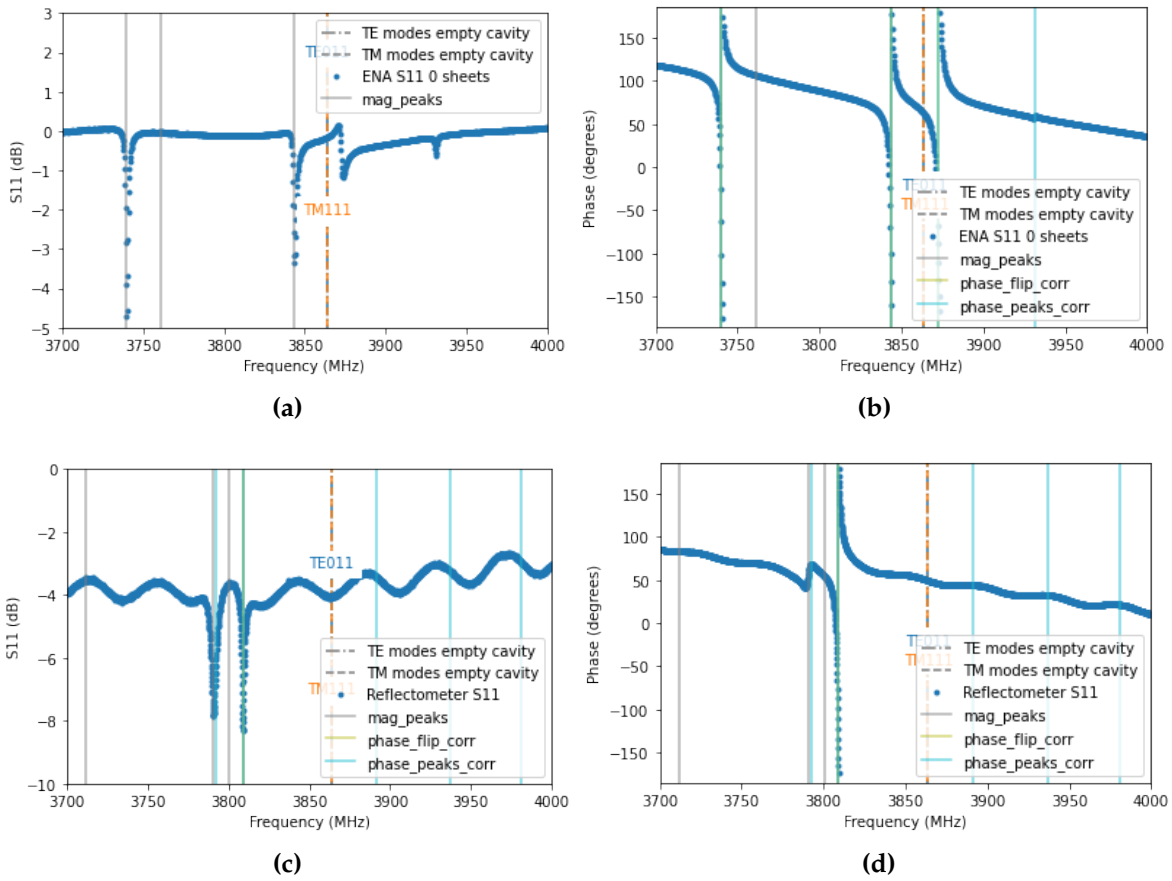

Figure 3.18: Reflectometer resonance finding examples. Shown are a) magnitude and b) phase of S_{11} data taken on bare metal surface using the ENA. The c) magnitude and d) phase of S_{11} data taken in the six meter D3A dish with the Fieldfox show visible ripples caused by the long (∼15 ft) coax used that day. The pair of resonances in c) and d) are shifted in frequency indicating the offset of the mesh from the reflectometer. The locations of resonances found using different methods, namely the magnitude peak finder (mag_peaks), the deramped phase flip finder (phase_flip_corr), and the deramped phase peak finder (phase_peaks_corr), are displayed. Each method has its strengths and weaknesses in peak detection.

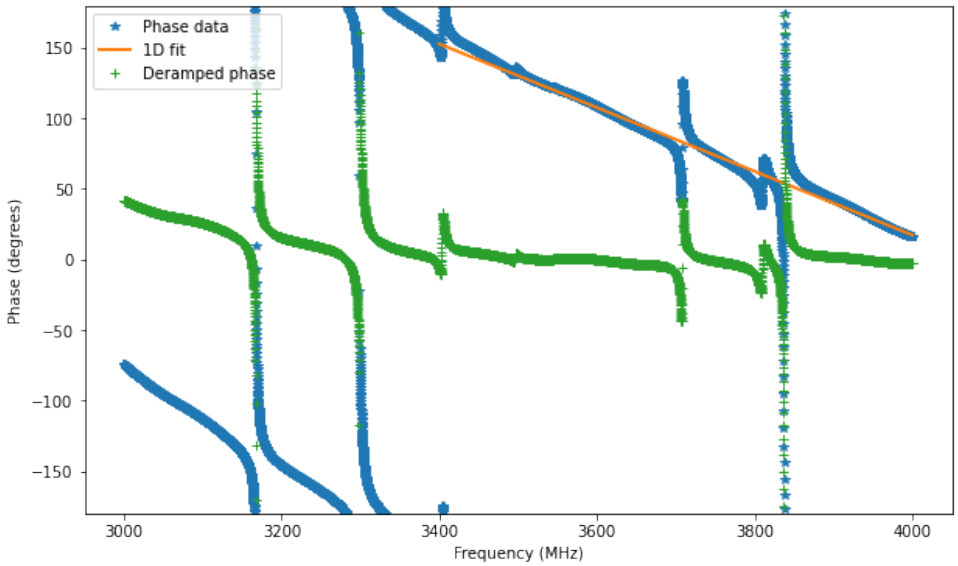

Figure 3.19: Reflectometer phase data correction showing the original phase (blue *), the 1D fit to the phase ramp (orange line), and the the deramped phase (green +).

Deramped phase peak finder

As with the magnitude peak finder, the deramped phase peak finder uses Scipy Signal's `findpeaks` but applies it to a version of the phase that has been corrected to remove the phase ramp. The motivation for subtracting the ramp is that the phase peak finder will primarily detect the phase flip from -180 to +180 degrees, which is the center of the phase change (and therefore the resonance) only when the background phase is close to zero. The deramping is performed by subtracting a 1D fit line from the phase data and rewrapping the data to lie within $\pm$ 180 degrees. Figure 3.19 demonstrates the deramping process, showing the original phase data, the 1D fit to the phase ramp, and the final deramped phase. Note that the Fieldfox and ENA have different ramps, so when using a new instrument it is good to confirm that the 1D fit line is fitting properly; warning statements are generated in reflectometerDepth if the automatic fit line is positive.

In Fig. 3.18b) the deramped phase peak finder locates the TE_{011} resonance that the magnitude peak finder missed in Fig. 3.18a). If the phase does not flip cleanly from -180 to +180 degrees on the phase plot the peak finder will not locate the dead center of the

resonance, but rather the peak to one side. The peak finder may pick up incorrect peaks in the phase that are not caused by resonances. Erroneous phase peak detection occurred consistently when a 15 foot cable is used in concert with the Fieldfox and oscillations are present in the data, as shown in Fig. 3.18c) and d). The magnitude peak finder and deramped phase flip finder discussed next are able to correctly locate the resonances in the aforementioned dataset.

Deramped phase flip finder

The deramped phase flip finder uses the same deramped phase as the deramped phase peak finder. Instead of searching for peaks, it searches for large discontinuities that mark the moment when the phase wraps from -180 to +180 degrees. The advantage of this method is that it will not detect false peaks; the disadvantage is that it will not detect resonances whose phase change lacks a discontinuity. These characteristics are illustrated in Fig. 3.18c) and d) where the phase flip finder misses a resonance detected by the phase peak and magnitude peak finders, but correctly discounts the ripples in S_{11} .

Phase gradient method

One method explored but not completed involved using the gradient of the phase. The phase, when unwrapped, should have its steepest slope at the center of the resonance, and therefore the peaks of the phase gradient provide the centers of the resonances. This method implicitly handles the phase ramp, which appears as a constant offset in the slope and does not affect peak finding. However, the gradient of the unwrapped phase using Numpy's gradient function [46] does not have smooth maximums but is jagged, as seen in Fig. 3.20. Consequently the method has not been fully developed, but could be an avenue for future improvements on the resonance finding methods.

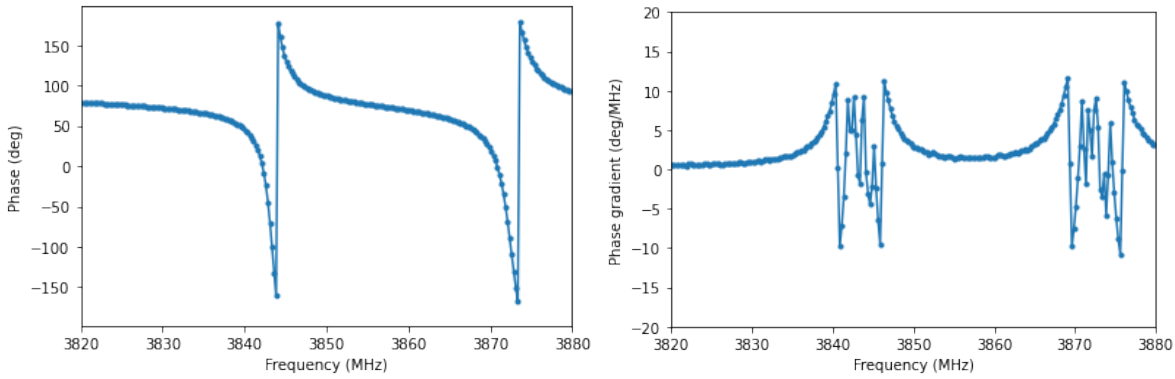

(a) **(b)**

Figure 3.20: Reflectometer data showing the a) phase and b) the phase gradient around the TE_{011} and TM_{111} resonances.

3.4.2 Depth calculations and comparison to simulation

Datasets are taken to compare the reflectometer performance to the CST simulations and determine the reflectometer's sensitivity to changes in depth. These datasets are taken by placing the reflectometer against a flat metal plate with sheets of paper in between to act as a depth offset. Each sheet of paper has a thickness of approximately 0.12 ± 0.01 mm, with 10 sheets measured to be 1.25 mm, which motivated the CST simulation offsets of 0.125 and 1.25 mm.

The first comparison between measurement and simulation is shown in Fig. 3.21, showing two extra resonances appearing in the measured data but otherwise a striking agreement between the location of resonances. In Section 3.3 it was shown that the higher frequency of the double peaks near the theoretical TE_{011} and TM_{111} frequency is the TE_{011} mode. In Fig. 3.21c) we see this higher frequency resonance is closest to the theoretical TE_{011} frequency, and so to identify the TE_{011} resonance we simply select the resonance closest to the theoretical TE_{011} frequency. Although the resonances shift to lower frequencies with increasing depth, no higher resonances come close enough to the theoretical TE_{011} mode at the offsets that we are investigating ($\sim$1 mm) to cause a false identification of the TE_{011} mode. The frequencies of the detected TE_{011} resonances and the resulting

depths are shown in Fig. 3.22. The depth is calculated using Eq. 3.3 for resonant modes in an empty cavity. Despite being against bare metal, the resulting depth in Fig. 3.22 is slightly negative (-0.07$\pm$0.02 mm for the Fieldfox), which can be taken into account as an offset when calculating absolute depths with Eq. 3.3. Possible future steps include fabricating a solid metal surface that the reflectometer can be calibrated against before measurements to accurately remove this offset for absolute depth measurements.

The second set of measurements involved adding sheets of paper between the reflectometer and the flat metal test plate as shown in Fig. 3.23 in order to add a small ($\sim$0.1 mm) but measurable offset. Datasets are taken on both the ENA and the Fieldfox, though on different days with different sheets of paper from the same notebook. The depth results are shown in Fig. 3.24, and the average depth per sheet of paper in Fig. 3.25. The average depth per sheet of paper measured with the ENA data holds fairly constant around 0.13 mm, giving confidence that using Eq. 3.3 to calculate depth is valid. The Fieldfox data in 3.25 shows a trend indicating that small offsets ($\lesssim$0.45 mm) tend to be underestimated and larger offsets ($\gtrsim$1.3 mm) tend to be overestimated. A comparison with the ENA data suggests that the Fieldfox data is accurate around 3-10 sheets of paper or 0.45-1.3 mm. Future work could aim to calibrate the Fieldfox bias out of the data, or alternatively an experimental relationship between frequency shift and depth offset could be derived. For now it is satisfactory that the data in Fig. 3.24 has shown that it is sensitive to shifts on the order of $\sim$0.1 mm, and the Fieldfox will continue to be used because it is portable.

The measurements presented in this section are performed on flat surfaces, but the dishes are parabolic and the reflectometer is presented with a curved surface. The expectation is that the reflectometer will provide the average depth of the surface that it covers [37]. To confirm this, data are taken with sheets of paper under only one edge of the reflectometer to determine the effect of a tilt. As expected, the tilt results in roughly half the depth of the paper under one edge.

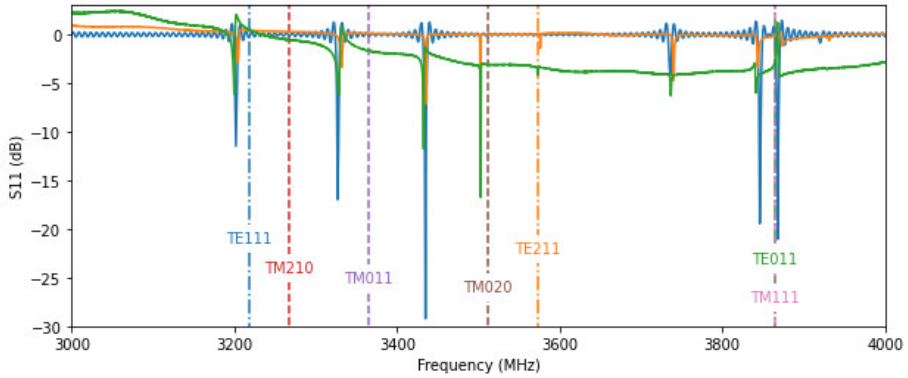

(a)

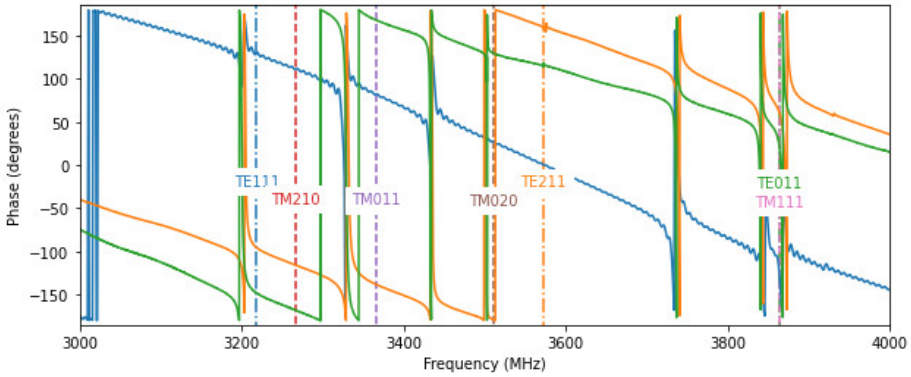

(b)

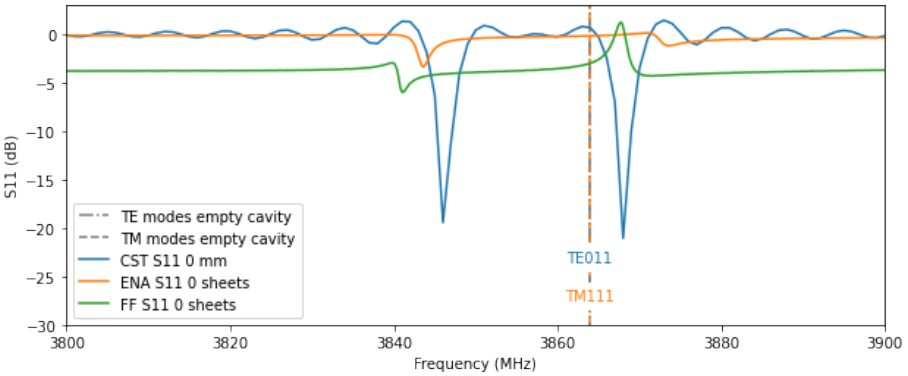

(c)

Figure 3.21: Reflectometer S_{11} a) magnitude and b) phase pressed against a metal plate comparing CST simulation (blue) with measurements done on the ENA (orange) and Fieldfox (green), with theoretical resonant modes of an empty cavity (dotted and dash-dot vertical lines). In c) we see the zoomed in S_{11} magnitude showing the peak locations around the TE_{011} mode.

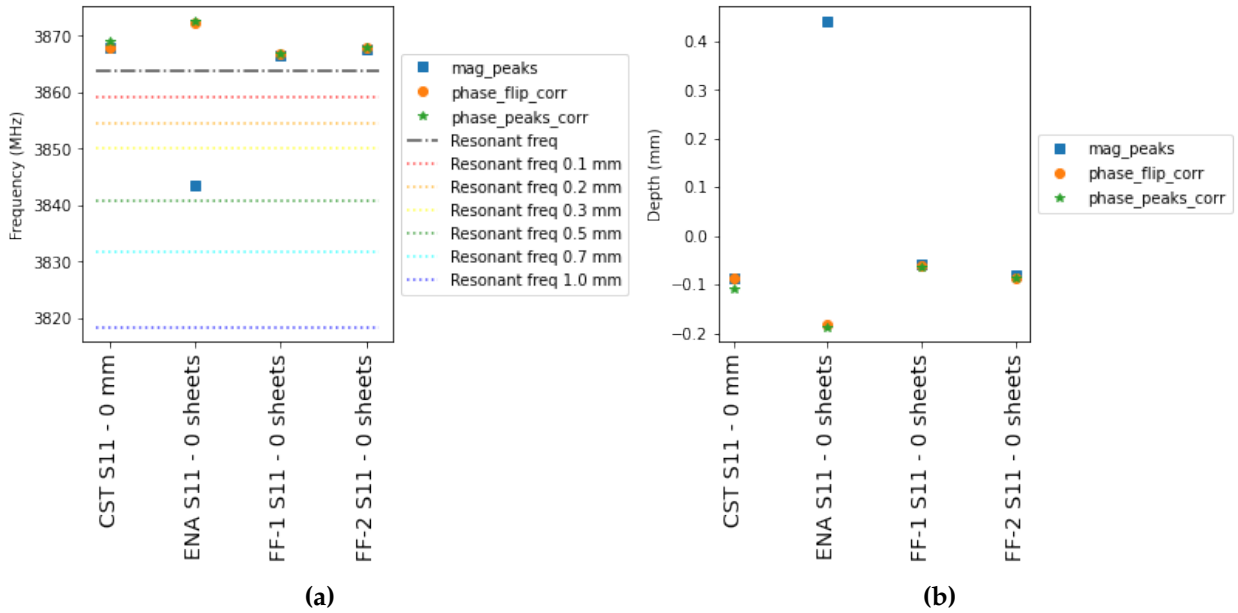

Figure 3.22: Reflectometer S_{11} TE_{011} a) frequency of TE_{011} mode and b) subsequent offset depth comparing CST simulation with measurements done on the ENA and Fieldfox (two runs, FF-1 and FF-2). Note that the magnitude peak finder (mag_peaks) in the ENA data has erroneously selected the TM_{111} mode, but because all three peak detection methods are plotted it is easy to detect. All other depth estimates are within $\sim$0.1 mm. The reflectometer shows an offset of -0.07$\pm$0.02 against bare metal.

3.5 D3A six meter dish measurements

Reflectometer measurements are taken on the first six meter dish created at DRAO to help determine whether the dish meets the required surface variance of $\lesssim$0.5 mm, necessitating the 0.1 mm precision achieved by the reflectometer. There are no requirements on the absolute depth of the mesh within the surface. These measurements are performed before the dish is painted while the metal mesh can be seen through the translucent composite material and examined for defects. Datasets were taken on three different days, Sept. 22, 24, and 28th, 2021. On Sept. 22 the dish was fully supported on the mount, whereas on Sept. 24 and 28 the dish was held aloft by a crane attached to the feed leg feet positions, as shown in Fig. 3.26. The mesh is fixed inside the composite surface, but changes in the support could cause flexion in the dish, resulting in a difference in the measured depth.

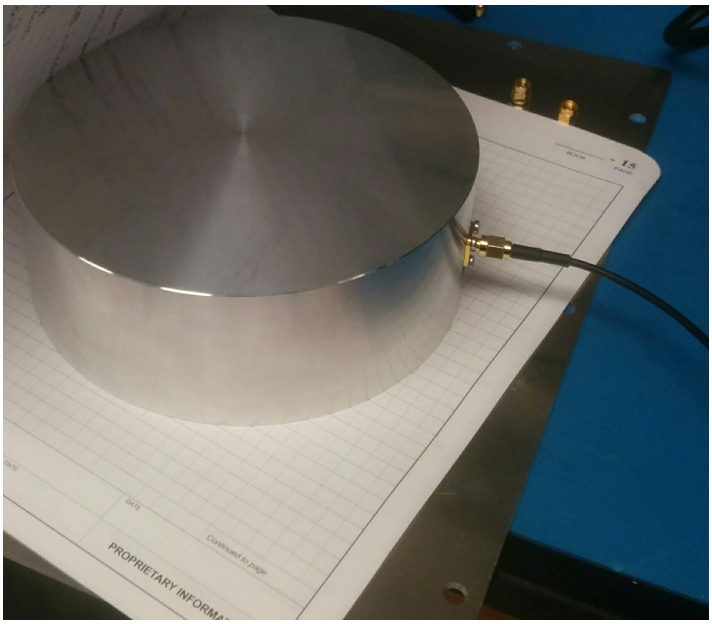

Figure 3.23: Reflectometer offset from metal test plate using pieces of paper each about 0.12±0.01 mm thick.

The attachment points for the crane are close to the support points for the dish backing ring, and likely cause similar deformations. As well, measurement differences between repeat data points taken on the same day are comparable to differences between days, as will be seen in the data sets presented later in this chapter. These differences are therefore unlikely to be day-to-day variations but rather measurement uncertainties from various factors including exact positioning, uneven pressure on the reflectometer forcing one edge up or down against the curved surface, and fibreglass dust and debris affecting contact with the surface of the dish.

A number of practical considerations must be dealt with when transitioning to reflectometer measurements within a dish. The first is pressing the reflectometer firmly against the dish while operating the Fieldfox and standing on a slippery curved surface. The difficulty of standing on the higher and steeper portions of the dish make higher locations inaccessible to measurements unless a second person is involved, or unless the dish is accessed externally using a ladder, in which case only areas close to the edge are accessible.

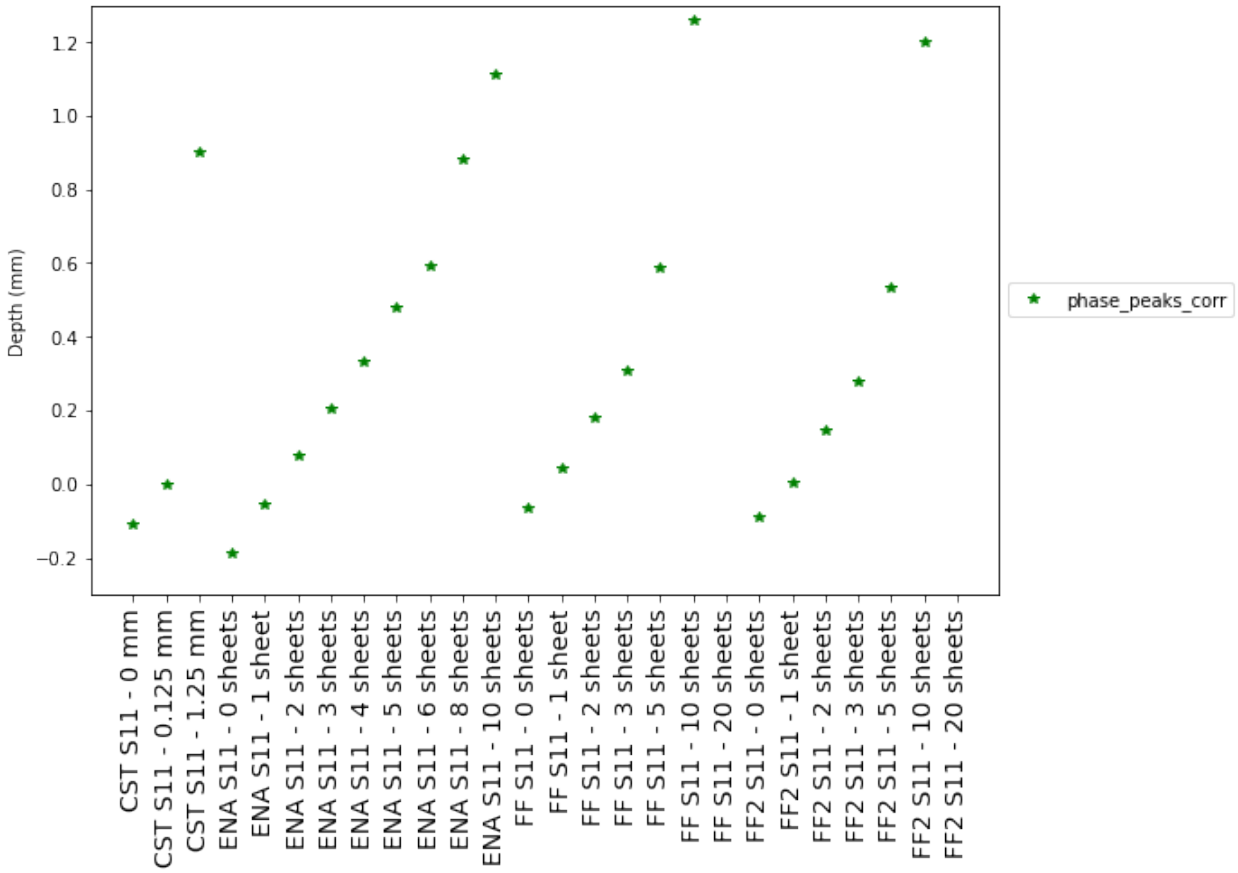

Figure 3.24: Depth measured with varying numbers of 0.12±0.01 mm thick sheets of paper comparing CST simulations and the reflectometer in combination with the ENA and the Fieldfox. Resonances are detected using the deramped phase peak finder method. The Fieldfox and ENA data taken on different days has a maximum discrepancy of $\lesssim$0.2 mm, most of which is accounted for by an overall offset that does not affect relative shifts. The Fieldfox data show $\lesssim$0.05 mm precision from day to day. All data show sensitivity to changes in depth on the order of 0.1 mm, which is our target precision.

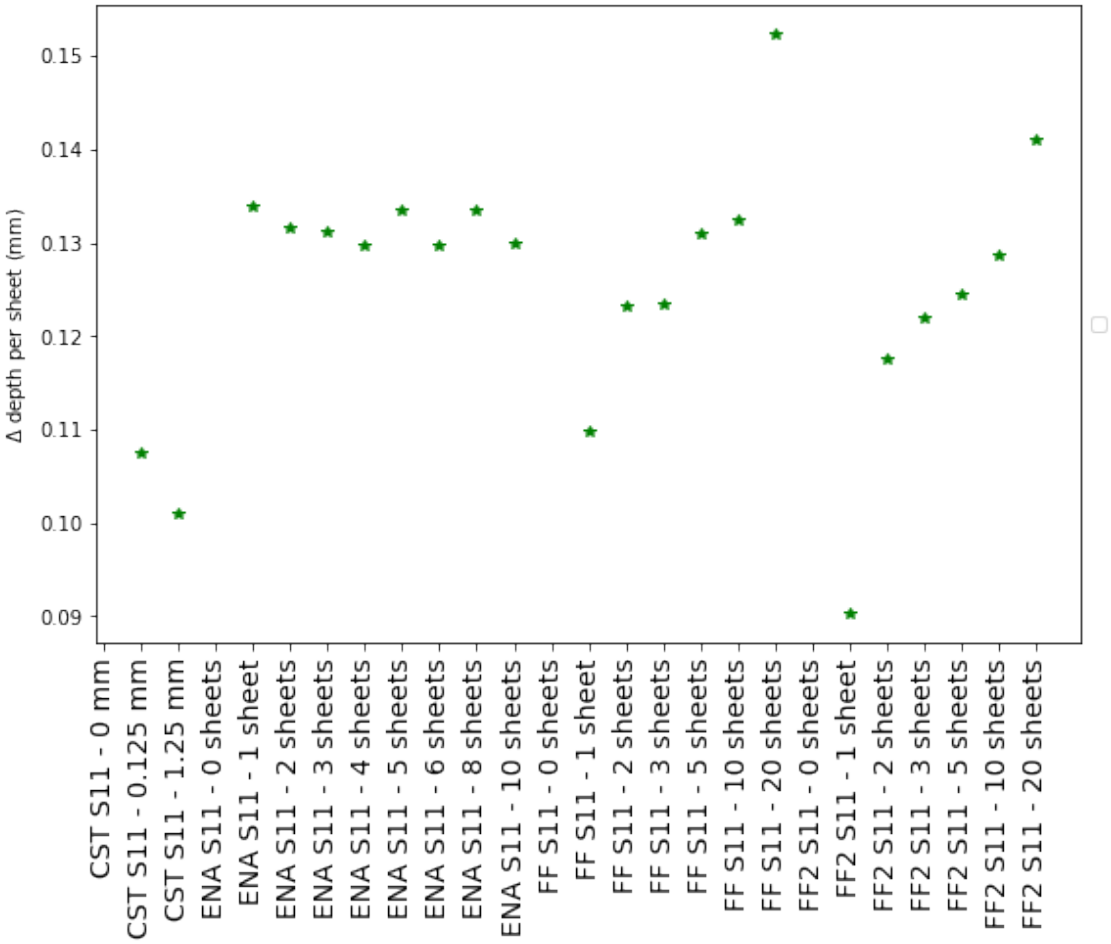

Figure 3.25: Average depth per sheet measured with CST simulations, and the reflectometer in combination with the ENA and the Fieldfox, using only the deramped phase peak finder (phase_peak_corr) method for locating resonances. The upward trend in the Fieldfox data suggests it will tend to overestimate large offsets and underestimate small offsets but seems accurate around 3 to 10 sheets of paper (or 0.45-1.3 mm).

Figure 3.26: First D3A six meter dish partially supported by a crane attaching to the future feet locations of the feed legs.

The second challenge is finding a method of locating the reflectometer within the dish. Because of the parabolic shape of the dish, the circular reflectometer covers areas with a different curvature and therefore a different average offset, referred to as the dish curvature offset, depending on the position within the dish. This offset is calculated in Section 3.5.1. An additional 0.025 mm offset comes from the surface composite layer overtop of the metal mesh and is considered negligible. The method of locating the reflectometer within the dish is measuring the arclength of the dish from the outer edge down to the reflectometer with a measuring tape as shown in Fig. 3.27; this level of accuracy is sufficient as arclength measured to 10 cm gives about 0.01 mm accuracy for the dish curvature offset. Only arclength is necessary to determine dish curvature offset because the dish has rotational symmetry. The difficulty of taking data with a single person means that the majority of the datasets in this section are taken with the invaluable assistance of K. Gerodias.

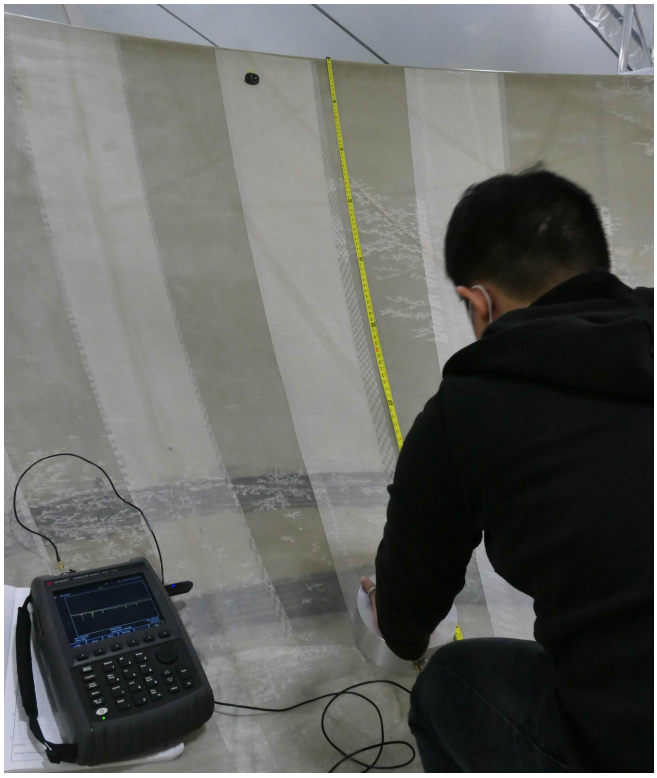

Figure 3.27: K. Gerodias measuring the arclength from the edge of the dish to the reflectometer (s_{edge}) with a tape measure. Measuring the arclength to within 10 cm provides the dish curvature offset within 0.01 mm.

3.5.1 Dish curvature

The curvature of the dish generates an additional offset to the reflectometer data depending on how far down into the dish the measurements are taken. The distance into the dish can be expressed as a radial distance from the center of the dish or as an arclength along the curve of the dish. The expression for a parabolic spheroid relating radial distance r to height z is

$$z = \frac{r^2}{4f} \tag{3.4}$$

and the arclength from the center of the dish s_{center} is

$$s_{\text{center}} = \frac{\frac{r}{2}\sqrt{f^2 + \frac{r^2}{4}}}{f} + f \ln\left(\frac{\frac{r}{2} + \sqrt{f^2 + \frac{r^2}{4}}}{f}\right) \tag{3.5}$$

where f is the focal distance [47]. While the radius r is used to calculate the dish curvature offset, it is more practical to measure the arclength from the edge of the dish to the reflectometer s_{edge} as shown in Fig. 3.27 because the center of the dish has no defining feature. This s_{edge} can be first translated s_{center} using $s_{\text{center}} = \max(s_{\text{center}}) - s_{\text{edge}}$, and then converted into the radius. The maximum value of s_{center} is calculated by plugging in the maximum radius into Eq. 3.5.

The equation for calculating the dish curvature offset was provided by [37]. The calculation takes into account the curvature of the dish, the radius a of the reflectometer, and the weighting of the TE_{011} mode, resulting in an offset Δd where

$$\Delta d = \frac{a^2}{\sqrt{32F^2 + 8r^2}}. \tag{3.6}$$

In this instance we use the 8.1 cm outer reflectometer radius as a rather than the 7.5 cm inner radius because the reflectometer outer edge makes contact with the dish (the edge of the reflectometer is not bevelled). Figure 3.28 shows the dish curvature offset the reflectometer will experience at a given arclength from the rim of a dish with a six meter diameter and 1.5 m focal length. The offset is 0.55 to 0.8 mm and varies by 0.25 mm which is quite large compared to the 0.1 mm precision measured with the reflectometer. The depth curvature offset must be taken into account and cannot be treated as constant unless the data are taken at the same arclength.

3.5.2 Measurement results

The measurements in this section are chosen to investigate aspects of the dish construction that might degrade the uniformity of the dishes, namely the seams shown in Fig. 3.29 where strips of metal mesh overlap, and defects such as wrinkles in the mesh shown in Fig. 3.30. Datasets used to spot check problem areas, for example wrinkles, are taken

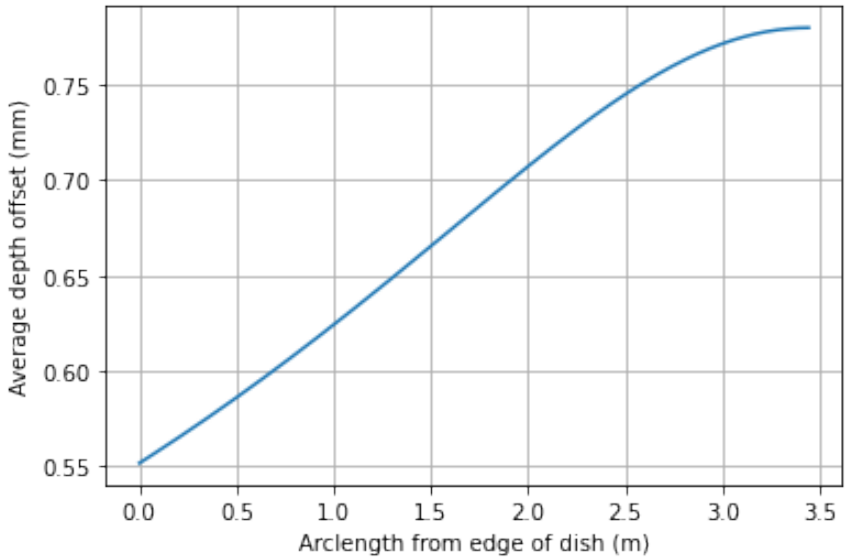

Figure 3.28: Average depth offset the 8.1 cm outer radius reflectometer will experience at a given arclength from the edge of the dish. Data generated for a six meter diameter dish with a focal length f of 1.5 m. Both the average offset and variation are large compared to the 0.1 mm precision of the reflectometer and must be taken into account when looking at data.

with other measurements at the same arclength into the dish to avoid differences in dish curvature offsets. All variances in depth are found to be within the 0.5 mm variance specifications.

In absolute depth the reflectometer measurements show a mesh depth roughly 0.5 mm greater than could be explained by the curvature offset and the negligible 0.025 mm estimated thickness of the composite layer in front of the mesh. Contributing factors could take the form of a) a constant offset, such as the mesh being deeper within the dish than estimated or extra distance caused by the unbevelled reflectometer edge contacting the curved dish, b) an overestimate in the depth, caused by the dielectric properties of the composite material, or c) unknown effects from other factors, such as the reflective surface being mesh rather than solid metal. Because the concern is the variance in the mesh depth rather than the absolute depth, a) a constant offset is not a concern for measurements of the first dish. Comparing offsets from dish to dish when more dishes have been

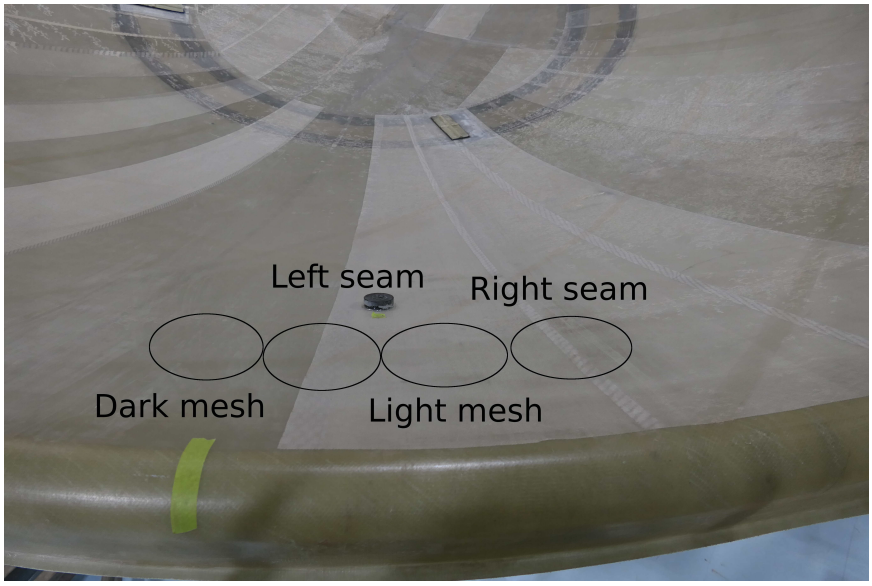

Figure 3.29: Locations of first D3A six meter dish seam measurements taken at the edge of the dish are labelled and shown in black circles. The light and dark mesh do not indicate depth; when viewed from different angles the mesh strips will appear alternately light and dark.

constructed is an area of future work and is discussed in Section 3.6.1. Having b) an overestimate of the depth would cause the variances in depth to likewise be overestimates, and our variance still meets the specifications. As for c) unknown factors, the effect the mesh has on the reflectometer has not been well characterized; measurements made on bare mesh are inconclusive because of difficulties keeping the mesh flat. In theory the 7.8 cm wavelength from the reflectometer's TE_{011} mode should see the mesh as a solid surface, since the largest gaps in the mesh are on the order of millimetres and well below the wavelength. For this analysis it is assumed that the additional depth comes either as a constant offset or overestimate in depth, and that the variance measured is generally indicative of the actual variance in depth or an upper bound. Further identifying the cause of the depth overestimate is a topic for future work.

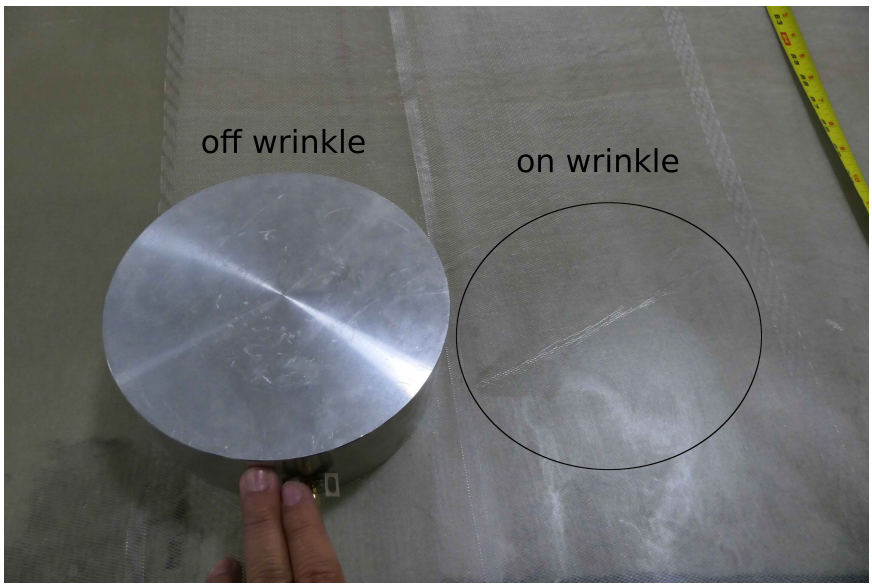

(a)

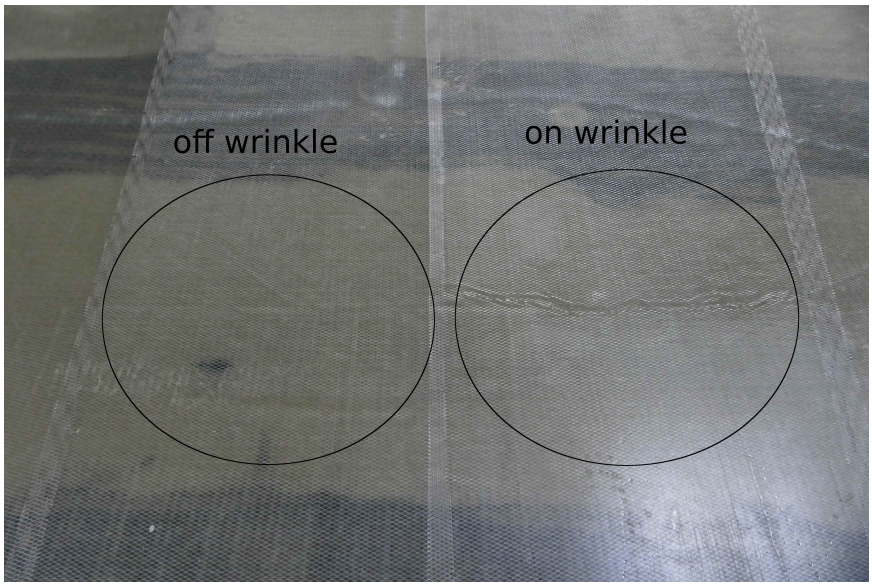

(b)

Figure 3.30: Wrinkles in D3A six meter dish mesh located at a) 75 inches and b) 86.5 inches arclength from the edge of the dish into the dish. The approximate positions of the reflectometer for the on and off wrinkle measurements are shown with black circles or in the case of a) with the reflectometer itself.

Seams

Datasets are taken on two different days examining seams at an arclength of 25 cm from the edge of the dish as illustrated in Fig. 3.29. The results in Fig. 3.31 show that that the greatest change in depth is not caused by the seams but is found when comparing one mesh strip to another; these two neighboring strips are visible in Fig. 3.29 as the light and dark regions. The visual difference arises from the interaction between the observation angle and the geometry of the mesh perforations, and is *unrelated* to the mesh depth. In this specific test case, the lighter mesh is embedded deeper in the dish than the darker mesh. This change, at less than 0.2 mm, is still well within the 0.5 mm requirements. Datasets between days show agreement better than 0.1 mm, reinforcing the 0.1 mm precision of the reflectometer. All of the measured depths exceed the dish curvature offset of 0.57 mm by about 0.4 to 0.6 mm.

Wrinkles

Datasets are taken examining the two wrinkles from Fig. 3.30 on Sept. 24 and 28 2021; data both directly on the wrinkle and off the wrinkle at the same arclength are taken for comparison and are shown in Fig. 3.32. The two wrinkles are centered at an arclength of 75 and 86.5 inches deep into the dish with an estimated dish curvature offset of 0.70 and 0.72 mm respectively; the reflectometer depth estimates are about 0.4 mm deeper. The wrinkle in Fig. 3.32a) does not show a difference in depth when compared to the measurement taken off the wrinkle, but the wrinkle in Fig. 3.32b) appears to be about 0.1 mm closer to the surface. The measurements are fairly consistent between the two datasets on Sept. 24 and 28th; all but one data point lie within 0.1 mm of their cohorts. The precision is notable as the coax cable running from the Fieldfox to the reflectometer is significantly different for the two datasets (approximately 2 versus 15 feet long), with the longer cable causing ripples in the Sept. 24 dataset (those seen in Fig. 3.18c) and d)) despite calibration with the Fieldfox.

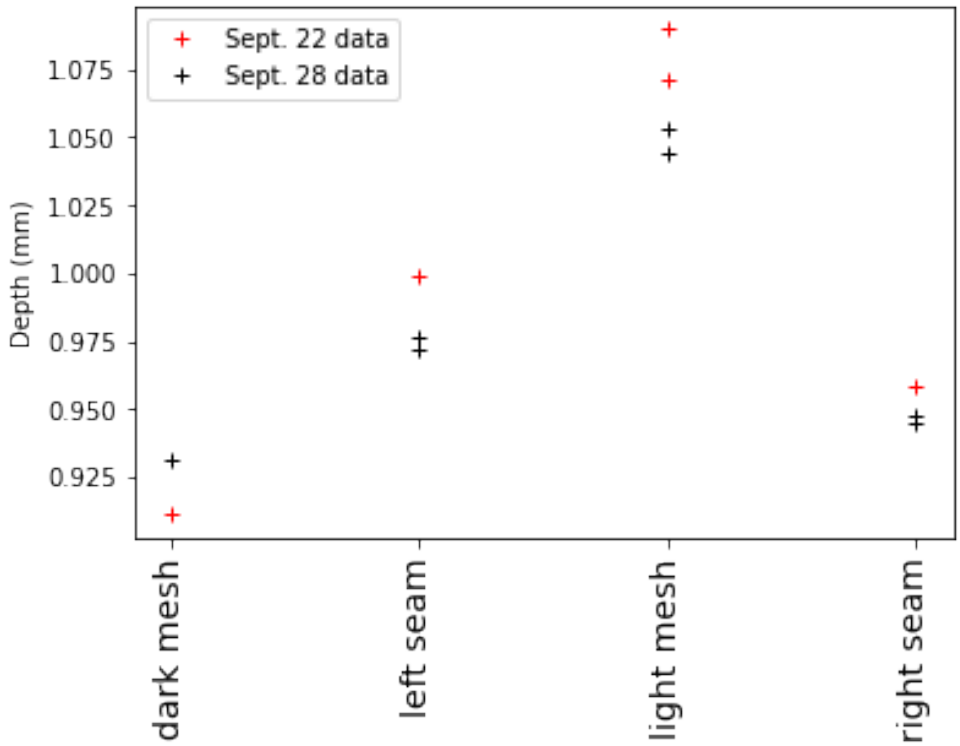

Figure 3.31: Measurement data taken over the mesh and seams pictured in Fig. 3.29. Resonances detected using the deramped phase flip method. Depths are significantly deeper than the 0.57 mm contributed from the dish curvature offset. While the different meshes and seams appear to be at different depths, all estimates lie within 0.2 mm of eachother, well within the maximum 0.5 mm variance requirement.

This measurement has shown a visible effect on the order of 0.1 mm over a wrinkle but still within the dish variance specifications of $<$0.5 mm. However this change is within the $\sim$0.2 mm variance noted between mesh strips during the previous discussion about seams, and it is not completely certain that the wrinkle is causing the change. Future spot checks on dishes should to take comparison points above and below the defect on the same strip of mesh in addition to the side to side points at the same arclength from the edge of the dish.

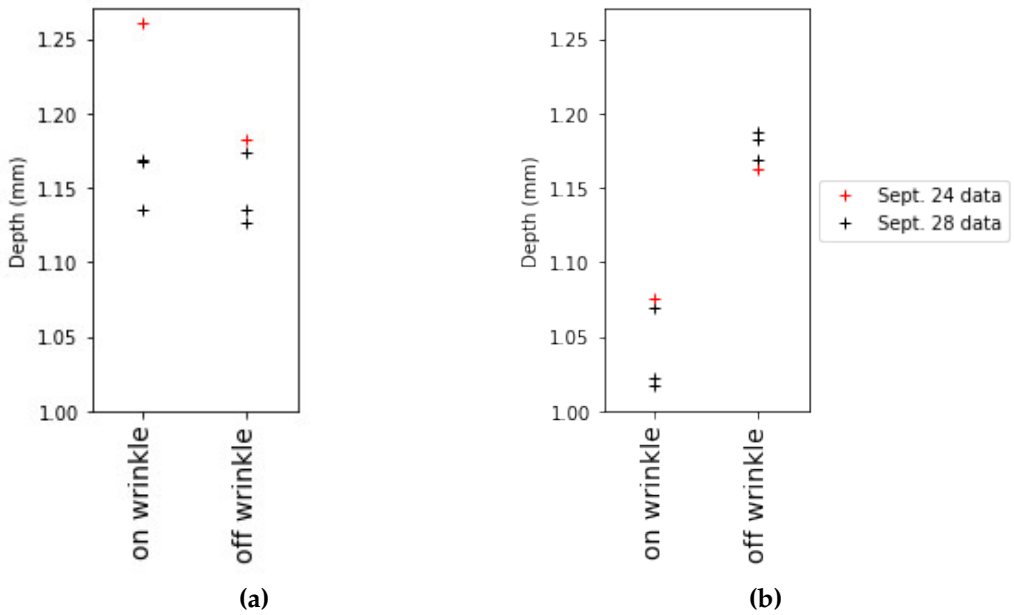

Figure 3.32: D3A six meter dish measurements with reflectometer taken on wrinkles compared to measurements off the wrinkles at the same arclength. The wrinkles are located at an arclength of a) 75 in and b) 86.5 in deep into the dish. All measurements are significantly deeper than the dish curvature offsets of 0.70 and 0.72 mm for a) and b) respectively. Resonances shown detected using the deramped phase flip method. The wrinkle in a) appears to have no effect on depth, while the wrinkle in b) appears to be about 0.1 mm closer to the surface than the measurement taken off the wrinkle at the same arclength.

3.6 Summary

The reflectometer is a tool that allows us to probe the reflective surface of the D3A dishes through the outer composite layer. This measurement provides information about the uniformity of the dish that is critical to the redundancy of the array. The reflectometer has been tested in the lab and shown to provide measurements with a precision of 0.1 mm when used in conjunction with the Fieldfox. Preliminary tests on the first six meter D3A dish indicate that the reflective mesh layer meets the required specifications on variance; the absolute depth was measured to be greater than expected and is a subject of future work, along with optimizing calibration of the reflectometer to improve precision and accuracy.

3.6.1 Future work

The reflectometer in conjunction with the Fieldfox can provide measurements with a precision of 0.1 mm. To improve accuracy and better understand the absolute depth measured by the reflectometer, further calibration is needed, requiring a more accurate test bed is than the sheets of paper and uncharacterized metal plates previously used. The ideal test bed would use an unbending metal surface flat to 0.01 mm and test offsets of 0.05 mm that are accurate to 0.01 mm. Such a setup could allow for corrections to the theoretical relationship between depth and frequency (Eq. 3.3), or for the derivation of a separate experimentally determined relationship. Note that these measurements are device specific, for the Fieldfox or ENA. The reflectometer could be calibrated against the flat metal surface at the beginning and end of any measurements to ensure consistency of the dataset. For further direct comparison to the dish, an piece of metal mesh could be obtained for calibration. Measurements on bare mesh were attempted at DRAO but difficulties ensuring the mesh was flat made the data inconclusive. Other unresolved questions include the extra roughly 0.5 mm depth that appears when measuring the depth of the six meter dish, which should involve an investigation into the effects of dielectrics on the reflectometer.

Further characterization of the dishes could involve comparing reflectometer measurements to optical measurements such as photogrammetry and laser tracking data which map out the surface layer of the dish. To enable precise comparison between reflectometer and laser tracker measurements, the reflectometer could be modified to allow a laser tracker nest to sit on the exterior which would allow precision placement of the reflectometer within the dish. If many measurements are to be made, a long handle attachment would allow the reflectometer to be pressed into the dish at a distance. Adding bevelled edges to the reflectometer could improve contact between the reflectometer and the dish.

Another consideration is that the reflectometer takes the average of the area underneath it. Defects in the mesh that have a small area relative to the opening of the re-

flectometer (47 cm^2) are averaged with the surrounding mesh. Constructing a smaller reflectometer might be a solution to determine the effects of smaller defects, though it is advisable to maintain a wavelength greater than the mesh spacing to avoid detecting surfaces through the mesh.

Dish to dish comparisons are an important avenue for future investigation when multiple dishes become available for reflectometer measurements. This comparison should determine whether the mesh is located at the same overall depth in each dish. Differences in mesh depth from dish to dish would mean that perfectly placed dishes still have a difference in the location of their reflective surfaces. This difference could affect the beam pattern by changing the distance between the feed and reflective surface and compromise the redundancy of the array if not compensated for in feed position.

3.6.2 Recommended best practices

Below is a list of recommendations for best practices when using the reflectometer to take data. The list includes suggestions to improve repeatability and confidence in the measurements.

- Ensure the loop antenna in the reflectometer is parallel to the flat back of the reflectometer and securely connected.
- Calibrate the Fieldfox with the coax cable at the beginning of each measurement session and save the calibration.
- Ensure the number of data points and frequency range provides a fine enough frequency resolution to resolve resonances (minimum sub-MHz).
- Save both the magnitude and phase of the S_{11} parameter; Touchstone (s1p) files are a convenient format.
- Keep a standard flat metal plate with the reflectometer and take a bare metal zero offset measurement before and after the dataset for calibration purposes.

- Wipe the edges of the reflectometer and the test surface clear of any dust before taking measurements.
- Press firmly on the center of the reflectometer when taking measurements.
- Take measurements three times, removing and replacing the reflectometer each time, to distinguish outlier measurements and estimate placement error.
- Frequently check the connections to the Fieldfox because they can work loose while the reflectometer is moved around.
- Take pictures and make note of what you are measuring for later reference, including any measurement setup used to locate the reflectometer within the dish.
- Orient the reflectometer the same way when taking measurements (ie SMA cable connection pointed downwards into the dish).

Bibliography

[1] J. R. Pritchard and A. Loeb, "21 cm cosmology in the 21st century," *Reports on Progress in Physics*, vol. 75, p. 086901, August 2012.

[2] B. Ryden, *Introduction to Cosmology*. Cambridge UK: Cambridge University Press, 2 ed., November 2016.

[3] L. B. Newburgh, K. Bandura, M. A. Bucher, T.-C. Chang, H. C. Chiang, J. Cliche, R. Davé, M. Dobbs, C. Clarkson, K. M. Ganga, and et al., "HIRAX: a probe of dark energy and radio transients," *Ground-based and Airborne Telescopes VI*, Aug 2016.

[4] L. Anderson et. al., "The clustering of galaxies in the SDSS-III baryon oscillation spectroscopic survey: baryon acoustic oscillations in the data releases 10 and 11 galaxy samples," *Monthly Notices of the Royal Astronomical Society*, vol. 441, pp. 24–62, apr 2014.

[5] T.-C. Chang, U.-L. Pen, K. Bandura, and J. B. Peterson, "An intensity map of hydrogen 21-cm emission at redshift z $\approx$ 0.8," *Nature*, vol. 466, pp. 463–465, Jul 2010.

[6] L. J. et. al., "The tianlai cylinder pathfinder array: System functions and basic performance analysis," *Science China Physics, Mechanics & Astronomy*, vol. 63, sep 2020.

[7] W. Fengquan et. al, "The tianlai dish pathfinder array: design, operation, and performance of a prototype transit radio interferometer," *Monthly Notices of the Royal Astronomical Society*, vol. 506, pp. 3455–3482, jul 2021.

[8] Santos, M. et. al., "A Large Sky Survey with MeerKAT," in *MeerKAT Science: On the Pathway to the SKA*, p. 32, Jan. 2016.

[9] NASA, "Introduction to Pulsars." [Online]. Available: `https://heasarc.gsfc.nasa.gov/docs/objects/pulsars/pulsarstext.html`, June 2007. Accessed: 2021- 10- 15.

[10] D. Castelvecchi, "Mysterious fast radio bursts come in two distinct flavours," *Nature*, June 2021. [Online]. Available: `https://www.nature.com/articles/d41586-021-01560-4`. Accessed: 2022- 03- 02.

[11] FRB Collaboration et al., "The First CHIME/FRB Fast Radio Burst Catalog," 2021.

[12] CHIME Collaboration, "CHIME." [Online]. Available: `https://chime-experiment.ca/en`, 2020. Accessed: 2021- 10- 10.

[13] D. Crichton et al., "Hydrogen intensity and real-time analysis experiment: 256-element array status and overview," *Journal of Astronomical Telescopes, Instruments, and Systems*, vol. 8, Jan 2022.

[14] K. Vanderlinde, A. Liu, B. Gaensler, D. Bond, G. Hinshaw, C. Ng, C. Chiang, I. Stairs, J.-A. Brown, J. Sievers, J. Mena, K. Smith, K. Bandura, K. Masui, K. Spekkens, L. Belostotski, M. Dobbs, N. Turok, P. Boyle, M. Rupen, T. Landecker, U.-L. Pen, and V. Kaspi, "The Canadian Hydrogen Observatory and Radio-transient Detector (CHORD)," in *Canadian Long Range Plan for Astronomy and Astrophysics White Papers*, vol. 2020, p. 28, Oct. 2019.

[15] M. Tegmark and M. Zaldarriaga, "Fast fourier transform telescope," *Physical Review D*, vol. 79, Apr 2009.

[16] A. Thompson, J. Moran, and G. Swenson, *Interferometry and Synthesis in Radio Astronomy*. Astronomy and Astrophysics Library, Springer International Publishing, 2017.

[17] J. J. Condon and S. M. Ransom, *Essential Radio Astronomy*. Princeton, New Jersey: Princeton University Press, 2016.

[18] Warren L. Stutzman and Gary A. Thiele, *Antenna Theory and Design*. Wiley, 3rd ed., 2013.

[19] J. W. McCorkle, "Noise Figure One and Two, Friis and IEEE." [Online]. Available: https://www.microwaves101.com/encyclopedias/noise-figure-one-and-two-friis-and-ieee#_Toc535079837, January 2019. Accessed: 2021- 10- 12.

[20] K. Blattenberger, "Conversion between noise figure and noise temperature." [Online]. Available: http://www.rfcafe.com/references/calculators/noise-figure-temperature-calculator.htm. Accessed: 2021- 10- 21.

[21] D. Pozar, *Microwave Engineering*. Wiley, 4th ed., 2011.

[22] W. D. Reeve, "Noise Tutorial Part III Attenuator and Amplifier Noise." [Online]. Available: https://www.reeve.com/Documents/Noise/Reeve_Noise_3_AttenAmpNoise.pdf, 2017. Accessed: 2021- 10- 21.

[23] D. E. Gary, "Lecture 5 Front End Receiving System." NJIT Physics 728 Radio Astronomy. Available: https://web.njit.edu/~gary/728/Lecture5.html, 2019. Accessed: 2021- 10- 24.

[24] Dassault Systemes, "CST Studio Suite Electromagnetic field simulation software." [Online]. Available: https://www.3ds.com/products-services/simulia/products/cst-studio-suite/, 2021. Accessed: 2021- 06- 17.

[25] McGill Cosmology, "ICE System." [Online]. Available: https://sites.google.com/a/mcgillcosmology.ca/mcgillcosmology/ice-system. Accessed: 2021- 10- 24.

[26] N. Denman, A. Renard, K. Vanderlinde, P. Berger, K. Masui, and I. Tretyakov, "A GPU Spatial Processing System for CHIME," *Journal of Astronomical Instrumentation*, vol. 09, p. 2050014, Sep 2020.

[27] M. Amiri, K. Bandura, P. Berger, M. Bhardwaj, M. M. Boyce, P. J. Boyle, C. Brar, M. Burhanpurkar, P. Chawla, and et al., "The CHIME Fast Radio Burst Project: System Overview," *The Astrophysical Journal*, vol. 863, p. 48, Aug 2018.

[28] J. Mena-Parra, C. Leung, S. Cary, K. W. Masui, J. F. Kaczmarek, M. Amiri, K. Bandura, P. J. Boyle, T. Cassanelli, J. F. Cliche, M. Dobbs, V. M. Kaspi, T. L. Landecker, A. Lanman, and J. L. Sievers, "A clock stabilization system for CHIME/FRB Outriggers," 2021.

[29] Mathworks, "Powergain." [Online]. Available: `https://www.mathworks.com/help/rf/ref/powergain.html`, 2021. Accessed: 2021- 08- 07.

[30] SciPy, "scipy.interpolate.interp1d." [Online]. Available: `https://docs.scipy.org/doc/scipy/reference/generated/scipy.interpolate.interp1d.html`, 2021. Accessed: 2021- 10- 11.

[31] NumPy, "numpy.polyfit." [Online]. Available: `https://numpy.org/doc/stable/reference/generated/numpy.polyfit.html`, 2021. Accessed: 2021- 10- 11.

[32] Noise Tech Microwaves, "Noise Parameter Equations." [Online]. Available: `https://www.microwaves101.com/encyclopedias/noise-parameter-equations`, 2021. Accessed: 2021- 06- 07.

[33] Times Microwave Systems, "LMR-400 Flexible Low Loss Communications Coax." [Online]. Available: `https://www.timesmicrowave.com/DataSheets/CableProducts/LMR-400.pdf`. Accessed: 2021- 06- 15.

[34] Times Microwave Systems, "LMR-195 Flexible Low Loss Communications Coax." [Online]. Available: https://www.pasternack.com/images/ProductPDF/LMR-195.pdf. Accessed: 2021- 06- 15.

[35] J. Mena-Parra, *Correlator and calibration for the Canadian Hydrogen Intensity Mapping Experiment*. PhD thesis, McGill University, Montreal, QC, July 2018.

[36] Times Microwave Systems, "LMR-195 Flexible Low Loss Communications Coax." [Online]. Available: https://www.timesmicrowave.com/DataSheets/CableProducts/LMR-195.pdf. Accessed: 2021- 06- 15.

[37] I. Theron. private communication, February 2021.

[38] R. Clauss and P. D. Potter, "Improved RF Calibration Techniques–A Practical Technique for Accurate Determination of Microwave Surface Resistivity," *Deep Space Network Progress Report*, vol. 12, pp. 59–67, Sept. 1972.

[39] D. Henke, G. Lacy, I. Wevers, P. Niranjanan, and F. Miranda, "Fabry-Perot resonator design for the measurement of surface reflectivity," in *2016 Global Symposium on Millimeter Waves (GSMM) ESA Workshop on Millimetre-Wave Technology and Applications*, pp. 1–4, 2016.

[40] J. P. Donohoe, "Waveguides." [Online]. Available: https://my.ece.msstate.edu/faculty/donohoe/ece3323waveguides.pdf. Accessed: 2021- 10- 10.

[41] F. Marhauser, "Lecture: Transmission Lines and Waveguides." Microwave Measurement and Beam Instrumentation Course at Jefferson Laboratory. Available: https://uspas.fnal.gov/materials/18ODU/11L%20Waveguides.pdf, January 2018. Accessed: 2021- 08- 12.

[42] Keysight Technologies, "FieldFox Handheld RF and Microwave Analyzers." [Online]. Available: https://www.keysight.com/ca/en/products/

network-analyzers/fieldfox-handheld-rf-microwave-analyzers.html, 2021. Accessed: 2021- 10- 12.

[43] Keysight Technologies, "ENA Vector Network Analyzers." [Online]. Available: https://www.keysight.com/ca/en/products/network-analyzers/ena-vector-network-analyzers.html, 2021. Accessed: 2021- 10- 13.

[44] Keysight Technologies, "SnP (Touchstone) File Format." [Online]. Available: https://na.support.keysight.com/plts/help/WebHelp2015/FilePrint/SnP_File_Format.htm. Accessed: 2021- 10- 14.

[45] SciPy, "scipy.signal.find_peaks." [Online]. Available: https://docs.scipy.org/doc/scipy/reference/generated/scipy.signal.find_peaks.html, 2021. Accessed: 2021- 08- 07.

[46] NumPy, "numpy.gradient." [Online]. Available: https://numpy.org/doc/stable/reference/generated/numpy.gradient.html, 2021. Accessed: 2021- 08- 07.

[47] Wikipedia, "Parabola." [Online]. Available: https://en.wikipedia.org/wiki/Parabola, 2021. Accessed: 2021- 10- 07.

[48] Hewlett Packard, "S-Parameter Design." Application Note 154, 1990.

Appendix A

S-parameters

Scattering parameters, which are commonly referred to as s-parameters, describe the scattering and reflections of the traveling power waves incident on a network of ports (see [48]). A given port has a superposition of a traveling wave heading towards the network and a second wave heading away. The S-parameters describe the strength of the outgoing wave from a port caused by an incoming wave from a port in terms of a ratio. Therefore, a given s-parameter S_{nm} denotes the power ratio of the traveling wave exiting port m to the traveling wave incident on port n given that all other incident waves on all ports are zero.

In the simplest case, a single port network such as a terminator or an antenna has only a single S-parameter. This is the S_{11} parameter and it characterizes the amount of incident power onto the input that is reflected away. Applications such as antennas will try to minimize the S_{11} as it represents a loss of signal power.

In a two-port network such as the one in Fig. A.1 from [48, Fig. 18], there are four S-parameters that correspond to the ratios of the incident waves on ports 1 and 2 (a_1 and a_2 respectively) and the outgoing waves (b_1 and b_2). The calculations for the S-parameters (from [48, Figs. 15-17]) are

$$S_{11} = \left.\frac{b_1}{a_1}\right|_{a_2=0}, \tag{A.1}$$

$$S_{21} = \left.\frac{b_2}{a_1}\right|_{a_2=0}, \tag{A.2}$$

$$S_{12} = \left.\frac{b_1}{a_2}\right|_{a_1=0}, \tag{A.3}$$

and

$$S_{22} = \left.\frac{b_2}{a_2}.\right|_{a_1=0} \tag{A.4}$$

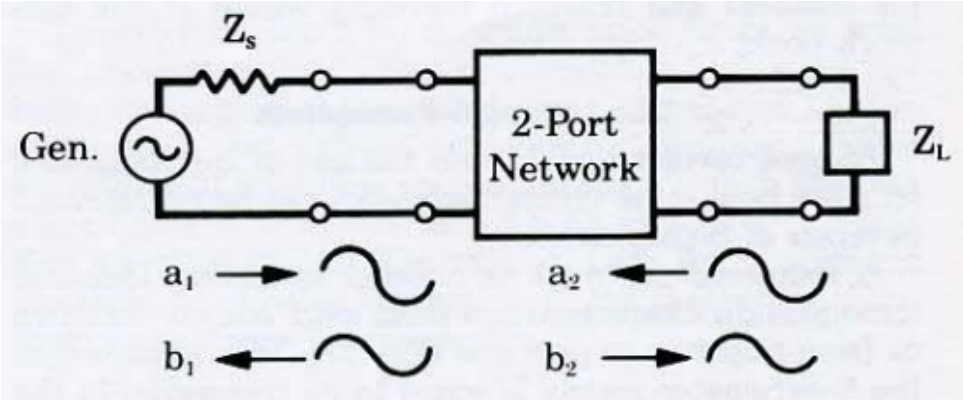

Figure A.1: Two port device illustrating S-parameters with a_1 and b_1 as incident and outgoing waves from port 1 respectively, and a_2 and b_2 as incident and outgoing waves from port 2 respectively. $\mathrm{Z_s}$ is the source impedance and $\mathrm{Z_L}$ is the load impedance. Figure from [48, Fig. 18].

.

$\mathrm{S_{11}}$ again describes the incident power reflected back from port 1, and $\mathrm{S_{21}}$ represents the gain from port 1 to port 2. In the case of a device such as an amplifier, the $\mathrm{S_{11}}$ would determine how much of the incoming signal was accepted into the amplifier, and the $\mathrm{S_{21}}$ would provide information on the amplification of that accepted signal.

S-parameters have both a real and imaginary component and their magnitude is often expressed in dB. The value of S-parameters can change over a given frequency range; for example with filters whose purpose is to block out certain frequency ranges will have a decreased gain or $\mathrm{S_{21}}$ in that region.

Appendix B

Reflectometer schematic

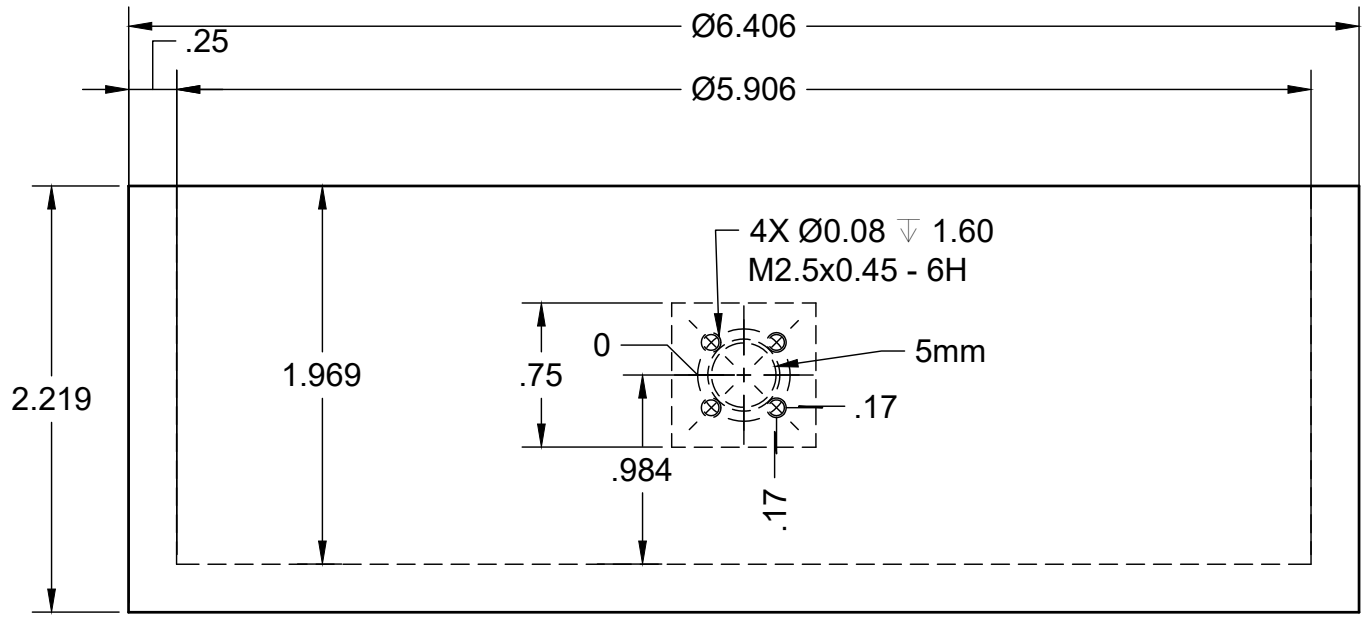

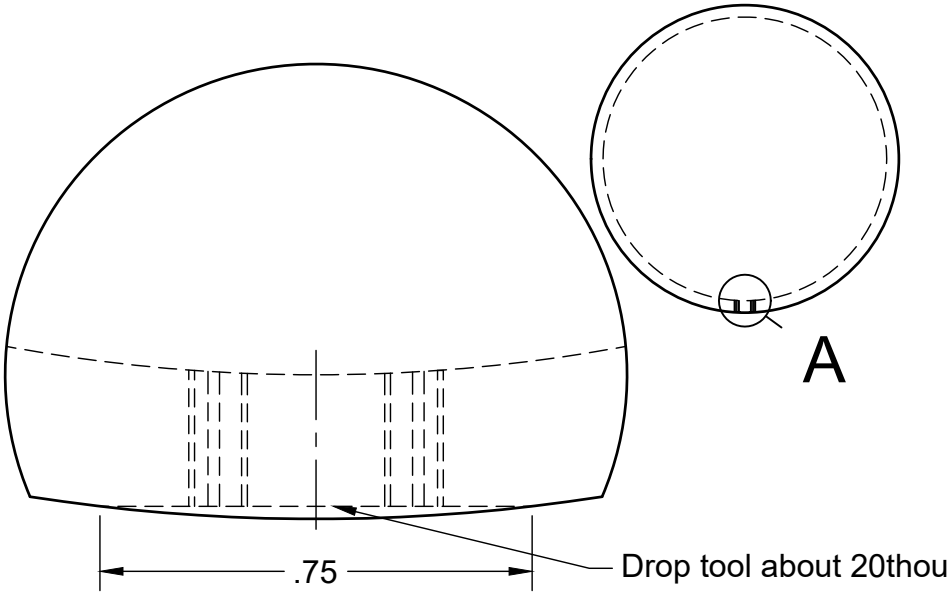

A

	PROJECT: Hirax			
	TITLE: resonator			
APPROVED	SIZE: A	CODE	DWG NO	REV
CHECKED				
DRAWN Simon Tartakovsky 2020-11-27	SCALE 1:1	WEIGHT	SHEET 1/1	